

Design, Characterization, and Implementation of Optical Systems
for Remote Sensing of the Atmosphere and Astrophysical Objects

By

Sarmad Albanna

Copyright ©Sarmad Albanna 2015
A Dissertation Submitted to the Faculty of the

COLLEGE OF OPTICAL SCIENCES

In Partial Fulfillment of the Requirements

For the Degree of

DOCTOR OF PHILOSOPHY

In the Graduate College

THE UNIVERSITY OF ARIZONA

2015

THE UNIVERSITY OF ARIZONA
GRADUATE COLLEGE

As members of the Dissertation Committee, we certify that we have read the dissertation prepared by Sarmad Albanna entitled “Design, Characterization, and Implementation of Optical Systems for Remote Sensing of the Atmosphere and Astrophysical Objects” and recommend that it be accepted as fulfilling the dissertation requirement for the Degree of Doctor of Philosophy

_____ Date: November 23, 2015
Milorad Cvijetic, PhD
Professor

_____ Date: November 23, 2015
Christopher Walker PhD
Professor

_____ Date: November 23, 2015
Yuzuru Takashima PhD
Associate Professor

Final approval and acceptance of this dissertation is contingent upon the candidate’s submission of the final copies of the dissertation to the Graduate College.

I hereby certify that I have read this dissertation prepared under my direction and recommend that it be accepted as fulfilling the dissertation requirement.

_____ Date: November 23, 2015
Dissertation Director: Milorad Cvijetic, PhD
Professor

STATEMENT BY AUTHOR

This dissertation has been submitted in partial fulfillment of requirements for an advanced degree at The University of Arizona and is deposited in the University Library to be made available to borrowers under rules of the Library.

Brief quotations from this dissertation are allowable without special permission, provided that accurate acknowledgment of source is made. Requests for permission for extended quotation from or reproduction of this manuscript in whole or in part may be granted by the copyright holder

SIGNED: __ Sarmad Albanna

A handwritten signature in black ink, appearing to read 'Sarmad Albanna', written over a horizontal line.

DEDICATION

I dedicate my dissertation work to my loving parents Hazim and Amel Albanna and to my incredibly supportive aunt and uncle Syham and Jim Manns whose words of encouragement and push for tenacity ring in my ears. I also dedicate this dissertation to my many friends and church family who have supported me throughout the process in many possible ways.

ACKNOWLEDGMENT

Though only my name appears on the cover of this dissertation, a great many people have contributed to its production and because of whom my graduate experience has been one that I will cherish forever. Given the one page space, I would like to acknowledge the ones who have played a key role in my success to complete this dissertation.

First I would like to express my deep appreciation and gratitude to my advisor, Dr. Milorad Cvijetic for the patient guidance and resilient mentorship he provided to me. His amazing support, encouragement through pushing me beyond my limits and helped me overcome many difficult situations throughout the PhD program leading to the completion of this dissertation.

In a similar vein would like to express my deepest appreciation and gratitude to my co-advisor, Dr. Christopher Walker. I have been amazingly fortunate to have him as an advisor especially at difficult times when he helped me recover when my steps faltered. Dr. Walker intellectual heft is matched only by his genuinely good and down-to earth nature. I hope that one day I would become as good an advisor to my students as Dr. Walker has been to me.

Special thanks go to my other committee member, Dr. Yuzuru Takashim for the friendly guidance, and thought provoking suggestions on the work in this dissertation that helped me improve my knowledge in the area.

I also would like to extend my thanks to the PIs on both projects Dr. Rob Kursninski on the ATOMMS instrument and Bill Shillue on the ALMA-Photonics LO system for providing the research funding needed, and for all the technical guidance and long discussions that helped me sort out the technical details of my work. I also would like to extend my gratitude to other scientists and engineers on both projects: Drs. Darrel Emerson and Larry D'Addario on the ALMA-Photonics LO system, and Drs. Angel Otarola, Abram Young, Christian Drouet d'Aubigny, Chris Groppi, and Mike Stovern on the ATOMMS instrument.

I would like to extend my deep appreciation to Drs Lars Furenlid, Ewan Wright, Harry Barret and Khanh Kieu for numerous enriching advises and stimulating discussions throughout the whole PhD program.

I would like to extend my appreciation to many of the amazing staff at the College of Optical Sciences at the University of Arizona to name few: Holly Brown, Mark Rodriguez, Luz Palomarez, Suzan Nares, Gail Varin, and Amanda Ferraris.

The support of my friends in and outside the college is not possible to forget who helped me overcome setbacks and help me stay focused on my graduate study. I greatly value their friendship and I deeply appreciate their belief in me.

Finally, yet most importantly, none of this would have been possible without the love and patience of my family.

Table of Content

Design, Characterization, and Implementation of Optical Systems for Remote Sensing of the Atmosphere and Astrophysical Objects.....	1
Abstract.....	13
Chapter I: Introduction and description of research topics	14
PART A: The ALMA instrument.....	15
I.1 Motivation for building ALMA	15
PART B: The ATOMMS instrument.....	29
I.3.1 SCIENTIFIC MOTIVATION.....	30
I.4. ATOMMS’s Measurement configuration.....	35
I.4.1 Radio occultation RO:.....	35
I.4.2 ATOMMS operational Concept.....	36
I.4.3 The ATOMMS Instrument.....	39
I.5. The Microwave Instrument.....	41
I.5.1 22 GHz.	41
I.5.2. 13 GHz.	44
I.5.3. 183 GHz	46
Chapter II: Optical phase correction/stabilization for ALMA Photonics LO [Early Development].....	52
II.1 Optical phase correction Background on existing approaches.....	53
II.2 Characterization of the physical factors affecting the LO phase error and the ALMA instrument coherence.....	55
II.3 First technique used of optical phase stabilization for the ALMA Photonic LO	57
II.3.1 Illustration of the proof of concept	58
II.3.2 Experimental setup.....	59
II.3.3 Test Results and Analysis	63
II.4. Optical phase correction for the Photonics LO with a moving structure.	68
II.4.1. Optical phase correction measurement at the ATF.....	68
CHAPTER III. OPSiF Performance.....	79
III.1 Faraday Mirror Implementation Baseline test.....	80
III.2 Phase correction with different length spools of fiber.....	82
III.3 Phase correction with the Fiber Movement:	85
III.4. Phase drift due to the Optical Amplifier.....	88

III.5. phase correction 2 ALMA antenna System implementation.....	89
III.5.1 PHOTONIC SYSTEM DESIGN DESCRIPTION.....	92
III.5.2. The Laser Synthesizer.....	94
III.5.4 The Optical Phase Stabilizer.....	96
III.5.6 EXPERIMENTAL SETUP	98
III.5.7 Fiber Wrap Configuration	101
III.5.8 MEASUREMENT RESULTS AND ANALYSIS	104
III.5.8.1 Phase stability without antenna fiber wrap motion.	104
III.5.8.2 Phase stability with simulated antenna motion.....	107
CHAPTER IV: ATOMMS QUASIOPTICS LENS DESIGN.....	113
IV.1 ATOMMS QUASIOPTICS SUBSYSTEM.....	115
IV.1.1 200 GHz Quasi-optics system	116
IV.1.2 22 GHz Quasi-optics system.....	119
IV.1.3 Lens selection and Zemax simulation	120
IV.2 LOSS CALCULATION & MEASUREMENTS	123
CHAPTER V: ATOMMS QUASIOPTICS CHARACTERIZATION.....	130
V.1 Introduction.....	131
V.2 The 22 GHz FH Far-field Measurements	132
V.3 Diffraction analysis of the ATOMMS quasioptics system.....	140
V.4 New Quasi Optics Design Concepts.....	147
V.5 Design III 2Lenses approach	148
V.5.1 Deriving the new optics design requirements from the ATOMMS System performance requirements.	150
V.6. 22 GHz 20 cm lens design.....	155
V.6.2 22 GHz RX.....	165
V.6.2.1 Design Criteria for the 22 GHz RX	165
V.6.3 Lens design	167
CHAPTER VI: CONCLUSION.....	173
APPENDIX A: Link Budget for 22 GHz Ground experiment	178
APPENDIX B	179
REFERENCES.....	183

LIST OF FIGURES

FIGURE (I.1).....	16
TOP ROW: HIGH REDSHIFT ($z > 1.5$) GALAXIES EXPECTED FROM A SIMULATED DEEP ALMA OBSERVATION.	16
BOTTOM ROW: LOW REDSHIFT ($z < 1.5$) GALAXIES EXPECTED FROM A SIMULATED DEEP HUBBLE OBSERVATION.	17
FIGURE I.2.1: ALMA LO SYSTEM LEVEL GENERATION AND DISTRIBUTION.....	22
FIGURE I.2.2: LO EQUIPMENT IN EACH ANTENNA, THE ABOVE ASSEMBLY IS PROVIDED FOR EACH BAND. AND THE PHOTONIC REFERENCE IS OPTICAL SWITCHED TO THE BAND IN USE.....	23
FIGURE I.2.2 SCHEMATIC IF THE LASER SYNTHESIZER	26
FIGURE I.2.3 – LASER SYNTHESIZER OUTPUT AT 108 GHz (AFTER PHOTOMIXER). THE MEASUREMENT NOISE FLOOR -97 dBc/Hz LIMITS THE MEASUREMENT ABOVE 200 kHz OFFSET. CF=108 GHz, SPAN=5 MHz, RBW=30 kHz	27
FIGURE I.2.4 –LASER SYNTHESIZER LOOP IF. SCALE IS 10 dB/DIV, RBW=30 kHz, NOISE MARKER AT 542 kHz OFFSET IS -103.1 dBc/Hz	28
FIGURE I.4.1 THE TWO SATELLITES OCCULTATION GEOMETRY	38
FIGURE I.4.2: ATOMMS EXPERIMENT CONFIGURATION. THE TWO PAYLOADS ARE REFERRED TO AS ATOMMS-A AND ATOMMS-B.	40
FIGURE I.4.3: BLOCK DIAGRAM OF THE ATOMMS A AIRCRAFT. WITH THE EXCEPTION OF THE SCIENCE TONE COMPLEMENT, ATOMMS B IS IDENTICAL.....	41
FIGURE (I.5.1) MICROWAVE ABSORPTION SPECTUM FOR WATER VAPOR AT DIFFERENT	42
FIGURE (I.5.2) THE ATOMMS 22 GHz TRANSMITTER (TOP) AND RECEIVER (BOTTOM).....	43
SUBSYSTEMS. ONLY 2 OF THE 8 CHANNELS ARE SHOWN IN EACH BLOCK DIAGRAM.	43
FIGURE (I.5.4) THE ATOMMS 13 GHz TRANSMITTER (BOTTOM) AND RECEIVER (TOP).....	45
SUBSYSTEMS. TWO OF THE EIGHT CHANNELS ARE SHOWN IN EACH BLOCK DIAGRAM.	45
FIGURE I.5.5.: STANDARD DEVIATION OF THE PHASE RATE ERROR FOR A 13 GHz SIGNAL GENERATED AND TRANSMITTED FROM ONE ATOMMS DEVICE, THEN RECEIVED AND DIGITIZED BY THE SECOND ATOMMS DEVICE BEFORE PROCESSING	45
FIGURE I.5.6: THE ATOMMS 183 GHz TRANSMITTER (TOP) AND RECEIVER (BOTTOM) SYSTEM BLOCK DIAGRAMS.	46
FIGURE I.5.7: THE FULLY ASSEMBLED ATOMMS A INSTRUMENT. VISIBLE COMPONENTS ARE LABELED. THE 183 GHz Tx AND 22 GHz Rx MODULES ARE NOT VISIBLE.....	48
FIGURE (I.6.1) AN THE AIRCRAFT TO AIRCRAFT OCCULTATIONS	48
TABLE II.1 EXPECTED FIBER PATH LENGTH CHANGE PER DAY	56
TABLE II.2 EXPECTED FIBER PATH LENGTH CHANGE PER HOUR	56
FIGURE II.3.1 BASIC PRINCIPLE OF THE TEST.....	59
FIGURE II.3.2.1 THE ACTUAL TEST ARRANGEMENT.....	59
FIGURE II.3.2.2: BLOCK DIAGRAM OF OPSIF TEST BOX.....	62
FIGURE II.3.2.3 SCHEMATIC OF CONTROLLER BOARD FOR CORRECTION LOOP, INCLUDING FILTER/AMPLIFIERS FOR MONITORING PHASE DETECTOR SIGNALS.....	63
FIGURE II.3.3.1 MEASUREMENTS USING STABILIZED MASTER LASER WITH 180M OF EXTERNAL FIBER	64
FIGURE II.3 3.2: SIMILAR TO FIG. II.3.3.1 BUT WITH 1 KM OF FIBER AND WITH THE MASTER LASER LOCKED TO ITS OPTICAL CAVITY BUT NOT TO THE ACETYLENE CELL.....	65
FIGURE II.3.3.3 SPECTRUM OF RESIDUAL ROUND-TRIP PHASE ERROR OBTAINED FROM DYNAMIC SIGNAL ANALYZER	66

FIGURE II.3.3.4: ALLAN STANDARD DEVIATION OF THE SIGNAL PHASE DATA FROM FIG. II.3.4.4 AT A FREQUENCY OF 26.625 GHZ.	67
FIG.II.4.1.THE TEST SETUP THAT WAS USED AT THE ANTENNA.....	69
FIGURE II.4.2 - PHASE FLUCTUATION OF THE 20 GHZ BEATNOTE VERSUS AZIMUTH POSITION (RED TRACE– TOP). THE SOLID LINE IS WITH THE LINE LENGTH CORRECTION ON AND THE DASHED LINE IS WITH THE CORRECTION OFF. THE PHASE ARTIFACT IS NOT AFFECTED BY THE CORRECTION, AND HAS SOME CORRELATION WITH THE VARIATION OF THE BEATNOTE AMPLITUDE (BOTTOM TRACE).	70
FIGURE II.4.4 TEST RESULT OF STATE-OF-POLARIZATION-DISPERSION OF OPTICAL CIRCULATOR. THE VERTICAL AXIS IS S_T (SEE EQ(1) ABOVE). EACH TRACE CORRESPONDS TO A SPECIFIC INPUT POLARIZATION ANGLE AS SHOWN IN THE KEY. PEAKS AND JUMPS OCCURRING OUTSIDE THE 1549.1-1550.4 RANGE ARE ARTIFACTS OF THE DATA ACQUISITION AND SHOULD BE IGNORED..	72
FIGURE II.4.5 - US PATENT #4,650,289 “OPTICAL CIRCULATOR – POLARIZATION INDEPENDENT INPUT TYPE” MAR 17, 1987.....	73
FIGURE II.4.6 - TEST SETUP FOR MEASUREMENT OF PHASE FLUCTUATION DUE TO FIBER MOVEMENT, USING TWO LIGHTWAVES WITH POLARIZATION ALIGNMENT ENFORCED BY USE OF A FREE-SPACE POLARIZER. THERE ARE NO CIRCULATORS IN THE RECEIVING SYSTEM.	74
FIGURE II.4.7: RESULTS OF TEST SETUP FIGURE II.4.6 THE PHASE FLUCTUATION RESULTED BY MOVING THE FIBER BY +360 AZIMUTH ROTATION AND BACK BY -360 DEG WHILE RECORDING THE CHANGE IN THE POLARIZATION DUE TO THE FIBER MOVE. THE MASTER AND SLAVE LASERS ARE FULLY ALIGNED IN THIS TEST RESULTS.....	75
FIGURE II.4.8: TEST SETUP FOR MEASURING THE VARIATION OF THE POLARIZATION OF THE LASER LIGHT TRAVELING THROUGH THE BURIED FIBER CABLE OF THE EVLA SITE WHILE SCANNING THE WAVELENGTH OF A TUNABLE LASER SOURCE.....	76
FIGURE II.4.9: RELATIVE POLARIZATION CHANGE (FROM INITIAL VALUE) FOR VARIOUS FIBERS- UNDER-TEST AS WAVELENGTH IS SCANNED FROM 1480 TO 1580 NM. THE VERTICAL AXIS IS S_T - SEE EQ (1).....	77
FIGURE II.4.10 THE 1.2NM-VARIATION IN S_T (AS DESCRIBED BY EQ3). THE S_T PARAMETER IS NORMALIZED TO THE OUTPUT SOP OF THE WAVELENGTH THAT IS 1.2 NM PRECEDING IT.....	78
FIGURE III.1 - FARADAY MIRROR TEST SETUP FOR THE LINE LENGTH CORRECTION SYSTEM WITHOUT THE USE OF AN OPTICAL CIRCULATOR. INSTEAD WE USED THE COMBINATION OF PBS AND FARADAY MIRROR TO ROUT THE LIGHT SIGNAL BACK TO THE NEAR END AS SHOWN IN THE BLUE LINE.	80
FIGURE III.2.2 (A): 10 KM OF FIBER AT 20 GHZ WITH THE CORRECTION ON AND OFF	84
(B): ZOOMED VERSION OF 10 KM OF FIBER AT 20 GHZ WITH THE CORRECTION ON.....	84
(C) THE MEASUREMENT OF THE ALLAN VARIANCE OF THE PHASE.....	84
FIGURE III.3.1: (A) 5 KM CORRECTION IS OFF WHILE BENDING THE FIBER (B) 5 KM CORRECTION IS ON WHILE BENDING THE FIBER	85
FIGURE III.3.2 10 KM LENGTH OF FIBER WITH CONTROLLED BENDING CORRECTION IS ON AND UNDERGOES CYCLICAL BENDING FROM 0 TO 275 SEC., THEN THE CORRECTION IS TURNED OFF FROM 275 SEC TO 525SEC. THE BEND RADIUS WAS CHANGING FROM 2.5 INCH TO 26 INCHES. ..	87
FIGURE III.3.4: 5 KM WITH TWISTING ½ INCH OF FIBER FROM 0 TO + 360 DEG AND THEN BACK FROM	87
+360 TO 0 DEG . THE CORRECTION IS OFF FROM 0 TO 130 SEC, THEN THE CORRECTION IS ON	88
FROM 125 SEC TO 327SEC, AND FINALLY CORRECTION IS OFF FROM 327SEC TO 490 SEC.....	88
FIGURE III.4.1: (A) TEST OF THE PHASE INCURRED ON 5 KM OF FIBER AT 20 GHZ WITH THE CORRECTION SYSTEM ON (FROM 0 SEC TO 800 SEC) AND OFF FROM (800 SEC TO 1700 SEC)	

WITH AN OA LOCATED JUST BEFORE THE FAR-END PHOTOMIXER (REFER TO FIGURE III.1). NO MOVEMENT OF THE FIBER HAS BEEN APPLIED. (B) ZOOMED VERSION OF THE CORRECTION ON PART OF (A)..... 88

TABLE III.5.1: A SUBSET OF ALMA PHOTONIC LO REFERENCE SPECIFICATION .. **ERROR! BOOKMARK NOT DEFINED.**

FIGURE III.5.1 SIMPLIFIED ALMA PHOTONIC LO SYSTEM DIAGRAM 94

FIGURE III.5.2.1 THE SCHEMATIC OF THE ALMA PROTOTYPE LASER SYNTHESIZER (LS)..... 95

FIGURE III.5.2.2 THE PHASE NOISE RESULTS COMPARING THE LS FIRST PHOTONIC LO OUTPUT AT 81 GHZ (BLACK) AND THE SCALED MICROWAVE REFERENCE TO 81 GHZ (RED), PHASE NOISE (1KHZ TO 10 MHZ) = 0.017 RAD= 35 FS. 96

FIGURE III.5.4.1 A SCHEMATIC OF THE ALMA PROTOTYPE OPTICAL PHASE STABILIZATION IN FIBER(OPSIF) AND THE PHOTONIC COMPONENTS IN THE LOPR..... 98

FIGURE III.5.6.1 A 81 GHZ PHOTONIC LO DIFFERENTIAL PHASE DRIFT EXPERIMENT SIMULATING 2 ALMA ANTENNAS. THE FIRST IS A REFERENCE LENGTH OF 10 M (ARM1) AND THE SECOND WITH 14 KM SPOOL OF FIBER AND A FIBER WRAP ASSEMBLY (ARM2)..... 102

FIGURE III.5.7.1 A PHOTO SHOWING TWO UNITS OF THE PROTOTYPE FIBER WRAPS THAT ARE USED IN THE AZIMUTH AND ELEVATION ROTATIONS IN THE ALMA ANTENNAS. THE TWO WRAPS ARE CONNECTED BACK TO BACK TO SIMULATE ANTENNA MOTION IN BOTH AZIMUTH AND ELEVATION ANGELS AT THE SAME TIME. 103

FIGURE III.5.8.2 THE DIFFERENTIAL PHASE MEASUREMENT OF 81 GHZ PHOTONIC LO REFERENCE BETWEEN 2 ANTENNA RACKS WITH 14 KM OF FIBER AND FIBER WRAP ASSEMBLY BETWEEN CENTRAL LO RACK & ANTENNA2 & 10 M BETWEEN CENTRAL LO RACK AND ANTENNA#1. BOTH OPSIFs WERE ACTIVE WHEN THE FIBER WRAP ASSEMBLY WAS UNDER 8 SEPARATE CONTROLLED ROTATIONS FROM 0°-360° AND 360°-0°..... 110

FIGURE III.5.8.3. THE DIFFERENTIAL PHASE MEASUREMENT OF 81 GHZ PHOTONIC LO REFERENCE BETWEEN 2 ANTENNA RACKS WITH 14 KM OF FIBER AND FIBER WRAP ASSEMBLY BETWEEN CENTRAL LO RACK & ANTENNA2 & 10 M BETWEEN CENTRAL LO RACK AND ANTENNA#1. BOTH OPSIFs WERE INACTIVE WHEN THE FIBER WRAP ASSEMBLY WAS UNDER 4 SEPARATE CONTROLLED ROTATIONS FROM 0° -360° AND 360°-0°..... 110

FIGURE III.5.8.4 THE ALLAN STANDARD DEVIATION Φ CALCULATION FOR THE RESIDUAL 81 GHZ PHASE IN CASE OF THE BASELINE WITH 20 FT OF CABLE LENGTH (BLACK CURVE), 14 KM OF FIBER WITHOUT APPLIED ROTATION TO THE FIBER ASSEMBLY WITH OPSIFs ACTIVE (BLUE CURVE) COMPARED TO THE ALMA PHASE DRIFT SPEC OF 0.51DEG AT 81 GHZ (RED LINE). ADDED TO THAT IS THE CALCULATED $\Delta\Phi_{AVE-RMS-81\text{ GH}}$ IN THE CASE OF 14 KM OF FIBER WITH APPLIED ROTATION TO THE FIBER ASSEMBLY WHILE OPSIFs ACTIVE (PINK LINE) AND INACTIVE (ORANGE LINE)..... 111

FIGURE IV.1: THE SIMPLIFIED QUASI-OPTICS SYSTEM DIAGRAM SHOWING BOTH THE 22GHZ & 200 GHZ FHS, 30 CM LENS ANTENNA, A DIELECTRIC SPIDER AND ABSORBER CONE. 115

FIGURE IV.2 E & H-FIELD BEAM PATTERN (SOLID AND DOTTED LINE RESPECTIVELY), WITH RESPECT TO THE ANGLE..... 122

θ , WITH $\theta=0$ (TOP) (PARALLEL TO THE DIELECTRIC SPIDER), AND 45° TILT AWAY FROM IT (BOTTOM). 122

FIGURE IV.3. THE SPOT SIZE IN IN $\square\text{M}$ AT THE 200 GHZ FH APERTURE (TOP), $40 \square\text{M}/\text{DIV}$ AND THE OPTICAL PATH DIFFERENCE (BOTTOM) WITH RESPECT TO CHIEF RAY IN WAVES AT THE WAVELENGTH OF 0.155 CM. 122

FIGURE IV:4 REFLECTION AND ABSORPTION LOSSES VERSUS FREQUENCY FOR A GROOVED HDPE LENS WITH $n=1.52$. THE STRAIGHT LINE IS JUST THE MATERIAL LOSSES, AND THE FABRY-PEROT

REFLECTION LINE IS MATERIAL LOSSES PLUS REFLECTION LOSSES, SIMULATED USING PROGRAM “SCATTER” WRITTEN BY R. PADMAN [67].	126
FIGURE IV.5 THZ PULSE TDS REFLECTION MEASUREMENTS SETUP DIAGRAM OF THE GROOVED AND UN-GROOVED SURFACES OF THE HDPE LENS.	127
FIGURE IV.6: THZ TDS REFLECTED E-FIELD MEASUREMENTS FOR THE GROOVED (RED) LENS FLAT SURFACE AND UN-GROOVED (BLUE) FLAT SURFACE WITH RESPECT TO FREQUENCY (THz). REFLECTED LOSSES FOR THE UN-GROOVED SURFACE AT BOTH 183 GHz AND 203 GHz IS \cong -18 dB, WHILE AT THE GROOVED SURFACE THE TOTAL LOSSES ARE -26 dB AT 183 GHz AND -27.2 dB AT 203 GHz.	128
TABLE V.1: FAR FIELD DISTANCES FOR THE 22 GHz TX RX PAIR FEEDHORNS.	133
FIGURE V.2.1: THE 22GHz FAR-FIELD BEAM PATTERN MEASUREMENT WITH AND WITHOUT THE 200GHz FH OBSCURATION.	133
FIGURE V.2.2 MEASURED AND SIMULATED WITH AND WITHOUT OBSCURATION RESULTS FOR 18.5 GHz.	135
FIGURE V.2.3 MEASURED AND SIMULATED WITH AND WITHOUT OBSCURATION RESULTS FOR 25.5 GHz.	136
FIGURE V.2.4 MEASURED AND SIMULATED WITH AND WITHOUT OBSCURATION RESULTS FOR 22.2 GHz.	137
FIGURE V.2.5 GAUSSIAN BEAMLET WITH CORRESPONDING RAYS	139
TABLE V.3.1 : 22.6 GHz GAUSSIAN BEAM PARAMETERS	141
FIGURE V.3.1 MODEL AND TEST CONFIGURATION	142
FIGURE V.3.2 THE NORMALIZED FIELDS AND PHASE AT THE 200GHz FEED AND AT THE 22 GHz RX (2130 CM AWAY)	143
FIGURE V.3.3 BABINET PRINCIPLE	144
FIGURE V.3.4 U(R,Z) AFTER THE DISK (A) AMPLITUDE (B) PHASE	144
FIGURE V.3.5: THE FRAUNHOFER DIFFRACTION PATTERN SEEN AT THE 22GHz FEEDHORN 2130 CM AWAY FROM THE TX WITH THE OBSCURATION IN PLACE FOR F=22.6 GHz	146
FIGURE V.5.1 DESIGN III DUAL LENSES BASIC CONFIGURATION SHOWING EACH FEEDHORN ILLUMINATING THEIR PERSPECTIVE LENS	149
FIGURE V.5.1: NORMALIZED GAIN AT 18.5, 22.6 & 25.5 GHz AND RESIDUAL AMPLITUDE ERROR IN % WHEN THE RATIO OF THE RECEIVED AMPLITUDES IS FORMED FOR LENS DIAMETER OF $D_{LENS}=30$ CM. MAXIMUM AMPLITUDE ERROR \sim 0.3% AT 0.25 DEG POINTING ERROR	151
FIGURE V.5.2: NORMALIZED GAIN AT 183 & 186 GHz AND RESIDUAL AMPLITUDE ERROR IN % WHEN THE RATIO OF THE RECEIVED AMPLITUDES IS FORMED FOR LENS DIAMETER OF $D_{LENS}=30$ CM (ONLY 15 CM OF THE DIAMETER IS ILLUMINATED) MAXIMUM AMPLITUDE ERROR \sim 0.8% AT 0.25 DEG POINTING ERROR.	152
FIGURE V.5.3: D=20 CM: AT 0.25 DEGREE POINTING ERROR CAUSES <0.2% DIFFERENTIAL AMPLITUDE ERROR BETWEEN 18.5 AND 22.6 GHz	152
FIGURE V.5.4: .NORMALIZED GAIN AT 183 & 186 GHz AND RESIDUAL AMPLITUDE ERROR OF 0.3% AT 0.25DEG WHEN THE RATIO OF THE RECEIVED AMPLITUDES IS FORMED FOR LENS DIAMETERS OF 10 CM	153
FIGURE V.5.5 WATER VAPOR & POINTING ERRORS FOR DIFFERENT ANTENNA SIZES FOR 22 GHz ..	153
FIGURE V.5.6; WATER VAPOR & POINTING ERRORS FOR DIFFERENT ANTENNA SIZES FOR 183 GHz	154
TABLE V.6.1: GAUSSIAN BEAM PARAMETERS AND FEEDHORN MECHANICAL QUANTITIES	158
FIGURE V.6.1 THE RELATIONSHIP BETWEEN THE ANTENNA EFFICIENCY EA AND THE QUANTITY A (RA/WA) ²	160

FIGURE V.6.2 SCHEMATIC OF THE FEEDHORN ILLUSTRATING THE SPHERICAL EQUIPHASE SURFACES AT THE APERTURE	161
FIGURE V.6.3: GAUSSIAN BEAM, TRANSFORMATION BY A QUASIOPTICAL SYSTEM CHARACTERIZED BY ITS ABCD MATRIX.....	164
FIGURE V.6.4 (A) SHOWS THE D_{OUT}/F VERSUS D_{IN}/F (B) SHOWS W_{OUT} VERSUS D_{IN}/F FOR 18.5,22.6 AND 25.5 GHZ	164
TABLE V.6.2 22 GHZ GAUSSIAN BEAM PARAMETERS	165
TABLE V.4. 22 GHZ HDPE ZEMAX LENS SURFACES PARAMETERS.....	168
FIGURE V.23 ZEMAX LENS CONFIGURATION	168
FIGURE V.25 SPOT DIAGRAM FOR 0, +1,-1 DEG FIELDS	170
FIGURE V.26 OPD FOR 0, +1 DEG AND -1 DEG FIELDS.....	170
FIGURE V.25 THE GAUSSIAN BEAM SPOT PRODUCED BY ZEMAX WITH $w_0=1.64$ CM.....	171

Abstract

This dissertation investigates the optical design and characterization for two distinct remote sensing applications. The first application is focused on the high precision optical phase correction for the photonic Local Oscillator (LO) designed for the Atacama Large Millimeter Array (ALMA). The phase instability in the original fiber optics design scheme is characterized and a novel, single mode fiber-based interferometric approach to measure and actively zero out the unwanted Photonic LO phase drift is introduced. The proposed technique is implemented and characterized by using a 16 km baseline with a two element array.

In the second application, the first iteration of the quasioptics design used in the ATOMMS instrument is characterized. (ATOMMS-Active Temperature, Ozone and Moisture Microwave Spectrometer-is the pathfinding implementation of an Earth and Space Atmosphere Global Remote Sensing Instrument).The diffraction problems in this design which were limiting the instrument performance were analyzed. Then different design concepts to mitigate these limitations and optimize system performance are presented.

Chapter I: Introduction and description of research topics

PART A: The ALMA instrument

ALMA is the most powerful telescope for observing the cool Universe — molecular gas and dust as well as the relic radiation of the Big Bang. ALMA will study the building blocks of stars, planetary systems, galaxies and life itself. By providing scientists with detailed images of stars and planets being born in gas clouds near our Solar System, and detecting distant galaxies forming at the edge of the observable Universe, which we see as they were roughly ten billion years ago, it lets astronomers address some of the deepest questions of our cosmic origins.

ALMA was inaugurated in 2013, but early scientific observations with a partial array began in 2011. The ALMA project is a partnership of Europe, North America and East Asia in cooperation with the Republic of Chile. ALMA is funded in Europe by ESO, in North America by the U.S. National [Science Foundation](#) (NSF) in cooperation with the National Research Council of Canada (NRC) and the National Science Council of Taiwan (NSC) and in East Asia by the National Institutes of Natural Sciences (NINS) of Japan in cooperation with the Academia Sinica (AS) in Taiwan. ALMA construction and operations are led on behalf of Europe by ESO, on behalf of North America by the National Radio Astronomy Observatory (NRAO), which is managed by Associated Universities, Inc. (AUI) and on behalf of East Asia by the National Astronomical Observatory of Japan (NAOJ). The Joint ALMA Observatory (JAO) provides the unified leadership and management of the construction.

I.1 Motivation for building ALMA

The ALMA instrument is located close enough to the Equator, in the southern hemisphere side such that it able to observe 73% of the Northern Sky and 87% of sky overall. ALMA is designed to explore the following 5 categories:

Category 1. Cosmology and the high redshift universe:

Telescopes are able to measure the rate of increase in distance of sufficiently distant light sources distance from Earth indirectly by measuring **cosmological** redshift. The sensitivity of ALMA is able to detect the distance of the first stars and galaxies that emerged from the cosmic "dark ages" billions of years ago that are Large Red shifted ($z > 1.5$) where Z is relative difference between the observed and emitted wavelengths, i.e.

$$z = \frac{\lambda_{observed} - \lambda_{emitted}}{\lambda_{emitted}} \quad (1)$$

ALMA sensitivity is illustrated in Figure (I.1) where the top row images shows the number of low redshift ($z < 1.5$) and high redshift ($z > 1.5$) galaxies expected from a simulated deep ALMA observation [1]. The bottom row shows that with an optical image, such as the Hubble Deep Field, most of the detections are of galaxies with $z < 1.5$. In stark contrast to the optical image, 80 percent of the ALMA detected galaxies will lie at high redshifts.

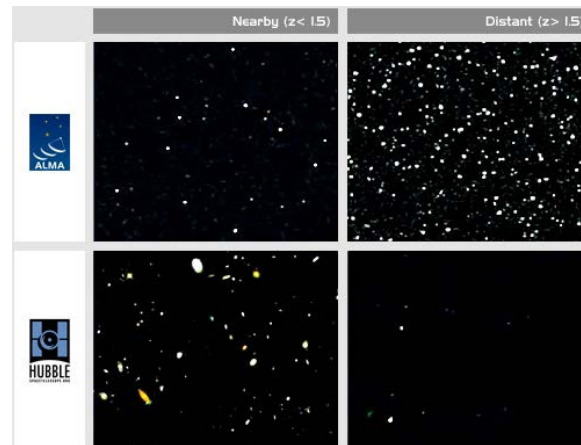


Figure (I.1)

Top row: high redshift ($z > 1.5$) galaxies expected from a simulated deep ALMA observation.

Bottom row: low redshift ($z < 1.5$) galaxies expected from a simulated deep HUBBLE observation.

ALMA will help us in the understanding of the true cosmic star formation history which is a crucial component in constraining galaxy formation models. There is a strong interest in searching for the first galaxies that emerged from the cosmic "dark ages" (at $z > 7$) which is a big observational challenge for galaxy formation studies. Earlier studies revealed that the rate of formation of cosmic stars has risen by one order of magnitude from the present-day to redshift $z=2$ ($\sim 10^9$ years ago). However, at $z > 2$, the contribution from the dusty star-forming galaxy population is still uncertain due to the lack of sensitivity of millimeter (mm) /submillimeter (submm) instruments before the ALMA-era. ALMA is designed to fill that gap by tracing the redshifted emission from near and beyond the peak of the dust emission.

Category 2 – Galaxies and galactic nuclei

ALMA will be able to explore the relationship between gas density, star formation, and gas kinematics. It will be able to resolve the small-scale structure of the molecular component that will clarify the mechanisms of starbursts/AGNs in galaxies, and the associated feedback processes, such as outflows of molecular gas, bubbles and winds. It will be also able to map out all types of galaxy types such as spiral, elliptical, dwarf and satellite galaxies at different mass ranges by producing maps with parsec and kpc resolutions.

ALMA will also allow us to constrain the H_2/CO conversion factor, which still contains large uncertainties as it appears to vary depending on the environment and metal content, etc. This is done by studying individual molecular clouds in nearby galaxies, including the Magellanic clouds

which are known to have lower metallicity, lower dust content, and star formation rate per unit area which is about 10 times larger than the solar region.

Category 3 – ISM, star formation and Astrochemistry

Life in the universe has become possible due to the creation of the planetary environments which is indirectly the result of the star formation in the universe which are the building blocks of the galaxy's structure. Star formation starts with an early phase called Protostellar collapse. ALMA have a very special ability to detect protostellar collapse on solar-system size scales. Gravitational forces within giant molecular clouds and the decrease of their velocities is the reason why protostellar are created. To detect the Gravitational collapse we would need to map the velocity field of smaller structures which would need high spatial and velocity resolution. ALMA will operate at wavelengths at which the collapsing object emits, and at which the surrounding material is transparent.

Further, ALMA will be ideal for studying the diversity of objects and physical processes involved in star formation. Its excellent mapping precision will allow astronomers to study the characteristics of parent molecular clouds from which stars form. Its sensitivity, angular and velocity resolution, and high frequency performance will allow the study of smaller structures, including protostellar fragments, outflows, and disks.

Category 4 – Circumstellar disks, exoplanets and the solar system

The most important stages of planet formation process are: The growth of submicron-sized, primordial interstellar grains out of **cosmic dust** grains into larger particles; the growth of these particles into planetesimals; and the growth and orbital evolution of these planetary embryos into

the mature systems observed around our own star and dozens of others. Circumstellar disks form as a result of the orbital evolution of these planetary embryos and they provide the elementary raw material and the early physical and environmental conditions for the formation of planetary systems.

Circumstellar disks pass through several discernible stages on their way to becoming planetary systems. Some stages of evolution of circumstellar disks:

- Protoplanetary disks largely primordial reservoir of gas and dust, massive enough to imply planet-forming potential
- Transition disks with properties intermediate between protoplanetary and debris disks, exhibiting substantial clearing of gas and/or dust from the systems
- Debris disks have little or no gas, tenuous dust disks, and dust lifetimes shorter than the age of the system, indicating that the disk is second generation rather than primordial.

ALMA will have a transformative role with its both sensitivity and spatial resolution for studies of circumstellar disks structure and evolution, particularly in the following area:

- Inside Transition Disk Cavities —providing the first look at the amount and location of planet-forming material on the spatial scale of the inner Solar system, which will have profound implications in particular for the study of the disk clearing processes operating in transition disks. The forest of molecular lines observable with the sensitive ALMA receivers, including low optical depth tracers, will allow for chemical modeling of the gas within the cavity. [2]
- Planet-Disk Interactions — High-resolution continuum observations with ALMA should provide direct evidence for planet formation through dynamical interactions, as well as constraints on the masses of young planets. It was suggested that giant planets are responsible

for clearing the inner cavities in transition disks, if so their dynamical signatures may be imprinted in particular on the wall at the inner edge of the outer disk.

Molecular lines: Combining sensitive spectral line surveys with high spatial resolution will provide detailed studies of the chemistry and kinematics of disks using molecular line observations, including rare tracers that will be less sensitive to cloud contamination and will permit the study of the gas properties of embedded disks. Generally speaking more sophisticated understanding of disk chemistry that will permit improved characterization of the gas content of circumstellar disks. The latter will also yield detailed information about the temperature, density, and kinematics as a function of height above the disk midplane (extending the work of Dartois et al. 2003; Panić [3]).

Category 5 Stellar evolution and the Sun

The Sun can be split into two regions: The **interior** is a sphere with radius $R = 7 \times 10^8 \text{m}$. The **atmosphere** lies on top and has consist of the following layers (from innermost to outermost):

1. The **photosphere** is about 300 km thick. Most of the Sun's visible light that we see originates from this region.
2. The **chromosphere** is about 2000 km thick. We only see this layer and the other outer layers during an eclipse. The **corona** extends outwards for more than a solar radius.

ALMA can resolve the photospheres and chromospheres of giant and supergiant stars within a few hundred parsecs. Moreover, in addition to free-free emission, ALMA will allow (sub) millimeter imaging of thermal emission from dust in stellar envelopes. ALMA will detect the photospheres of stars across the HR diagram, including those in the Bright Star Catalog, as it did recently for α Centauri [4]

ALMA's ability to detect the photospheres of so many stars allows it to measure positions relatively often to astrometric accuracy. The orbit of any planet around its central star causes that star to undergo a reflexive circular motion around the star-planet barycenter. By taking advantage of the incredibly high resolution of ALMA in its widest configuration, we may be able to detect this motion. This will enable ALMA to indirectly detect planets which may orbit these stars.

I.2 The instrument description and some important technical specification

ALMA will consist of an array of up to 64 12-meter parabolic antennas operated interferometrically and spanning a range of 31-950 GHz. The antennas will be located on a plateau at 5000m elevation and will be separated by distances of up to 15 km. The millimeter wave front-end receivers are cryogenically-cooled and use SIS mixers (above 90 GHz) or low-noise-amplifiers (below 90 GHz) as the initial active element. All receiving bands will be operated as heterodyne receivers that require a phase-stabilized local oscillator (LO) coherent among all antennas.

The phase stability specifications of the instrument are driven primarily by the requirement for high coherence and high dynamic range synthesis mapping at the highest operating frequency of 950 GHz. The design philosophy of the ALMA electronics systems, photonics systems, and antenna structure itself is that the phase stability of these elements should not appreciably degrade the instrument capability which is otherwise limited by the atmosphere. Extensive site measurements on the Chajnantor plateau (in the Chilean Andes) have documented the very stable atmospheric conditions [5]. The remarkable atmospheric stability can be further improved by calibration devices. The allowable phase stability over the integration time of the instrument (10 sec or less) must not cause loss of coherence exceeding that which is expected to occur due to the atmosphere after calibration. Coherence of an interferometer is given approximately by:

$$C=1- \phi^2/2$$

Where ϕ is the rms phase deviation for all frequencies greater than the inverse of the integration time [6]. At the highest ALMA frequency of 950 GHz, the rms atmospheric fluctuations after correction is expected to be better than 75 fsec or 25.6 deg (C4.9) at least 5% of the time. We have chosen to use this level as a specification for the rest of the system. The First LO is allotted 50% of the overall system phase stability, for an RSS level of 53 fsec. For slower fluctuation scales greater than the integration period (10 sec) but less than the maximum calibration period (1000 sec), phase drift causes degradation in image quality. The slow phase drift specification was set to 25 fsec, again using the criterion that the atmosphere would be the dominant contributor 95% of the time. The first LO was allocated 50% of the RSS total, or 17.7 fsec.

Figure I.2.1 is a high-level block diagram of the LO reference generation and distribution system. The blocks shown will be located in a building near the center of the array. Figure I.2.2 shows the LO equipment at an antenna. The 31-950 GHz range of the receivers is actually partitioned into 10 bands, with separate RF and LO hardware for each; typical LO equipment for one band is shown.

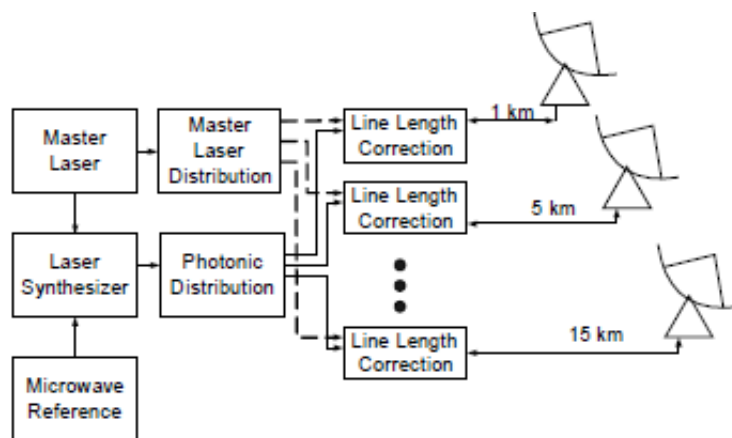


Figure I.2.1: ALMA LO system level generation and distribution

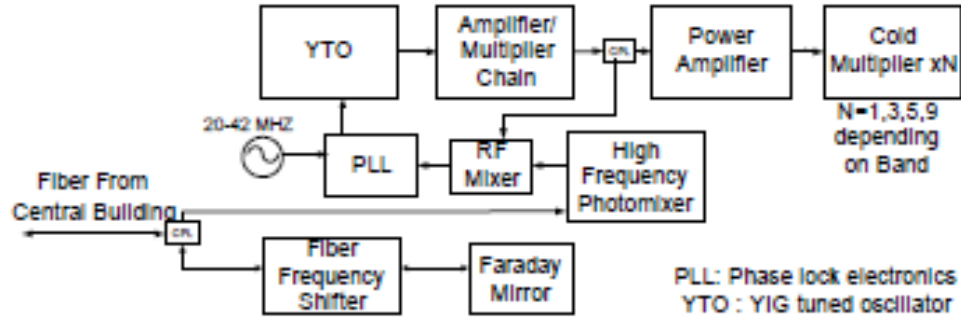


Figure I.2.2: LO Equipment in each antenna, the above assembly is provided for each band. And the Photonic reference is optical switched to the band in use.

The receivers in each of the ALMA antenna require a phase-stabilized local oscillator (LO) coherent among all antennas. These LO signals will be supplied by assemblies of YIG oscillators with relatively low (12-25 GHz) fundamental frequencies that get multiplied up to the higher frequencies by multiplier/amplifier stages. Each antenna and receiver has dedicated LO assemblies mounted directly to the receiver front ends. These local oscillators must have very low phase noise, and the phase drift between any two such LOs must also be very low. All this will be imposed as design constraints in technique that we propose for the high precision optical phase correction for the photonic LO. Namely, the phase instability in the original fiber optics design scheme is characterized, and based on that a novel single mode fiber-based interferometric approach to measure and actively zero out the unwanted Photonic LO phase drift is introduced. The LOs must actually be coherent across the wavefront of the astronomical signal; this requires that their phases be continuously adjusted in real time to account for the differential Doppler shift induced by the rotation of the earth. We choose to accomplish this by distribution of a centrally-generated reference signal to all antennas. The reference will be transmitted over buried optical fiber whose routing requires fiber lengths of up to 15 km. The reference signal is used to phase-

lock electronic oscillators at the antennas. The total phase noise of the resulting LO is the sum of the intrinsic phase noise of the electronic oscillator outside the loop bandwidth and the reference noise within the loop bandwidth.

An important design decision was that the reference should be transmitted at the frequency higher than the actual LO frequency, or at the highest frequency permitted by available technology, to minimize the need for frequency multiplication at the antennas and the corresponding multiplication of phase errors on the reference signal. Photodetector technology at 1.55 microns currently limits the maximum practical frequency to ~150 GHz [7,8].

I.3 Description of the photonic LO reference

In this design, the reference signal is a single sinusoid of variable frequency, depending on the desired astronomical observing frequency, and it is encoded as the difference in frequency between two optical carriers generated by two lasers. The first of these, called the master laser (ML), operates at a fixed wavelength and the second, called the slave laser (SL), is tunable and is phase locked to the master. Copies of the same two-wavelength signal are then distributed to all antennas. By careful design, including the use of narrow linewidth lasers and a fast phase-locked loop (PLL), phase-stable references are produced at the array center. To maintain this stability at each antenna, the electrical length of the fiber is actively stabilized by returning a portion of the master laser signal along the same fiber and measuring the round-trip phase change.

The laser synthesizer shown in Fig. I.2.2 contains the slave laser and the phase locking circuitry, and its output is the two-wavelength optical signal. Optical phase correction block contains a fiber stretcher in the signal path along with circuitry to measure the two-way optical phase of the ML carrier. The fiber stretcher is driven by a servo so as to keep the phase constant. The development of the last block will be described in more detail Chapter II and III.

At each antenna, the optical signal is delivered to a photodetector which acts as a mixer

(photomixer) to recover the difference-frequency reference in millimeter-wavelength waveguide. The reference covers a portion of the range 27-142 GHz, depending on the receiving band. An electronic oscillator near the same frequency (consisting of a YIG-tuned oscillator in the range 12 to 25 GHz and a chain of frequency multipliers and amplifiers) is phase locked to the reference. For those bands that require an LO frequency above 142 GHz, the locked oscillator is followed by a frequency multiplier (cryogenically cooled) at a factor $N = 3$ to 9. The main purpose of these electronic components is to provide sufficient LO power for the receiver; if enough power were available from the photomixer, its output could in principle be used directly as the LO signal. In the chosen design, the only uncorrected phase drift comes from the power amplifier and cold multipliers, which are outside the PLL. Meanwhile, a portion of the optical signal is coupled off before the photomixer and passed through an optical frequency shifter (acousto-optic cell) driven at 25 MHz and then reflected at a Faraday mirror. The reflected signal returns by the same path to the OPSIF assembly at the center.

Details of the laser synthesizer design are shown in Figure I.2.2. It takes as input the master laser signal (frequency f_M) and a variable low-noise microwave reference ($f_R = 8$ -12 GHz), and generates a second lightwave at optical frequency $f_S = f_M + n f_R + 125\text{MHz}$. This might have been accomplished by various techniques such as comb generation in combination with phase locking [9], or injection-locking [10]. It was decided to use electronic phase locking of a tunable DFB fiber laser. Space limitations prevent giving a full description of the reasons for our selection of this method here. However, the key elements of the technique are: we are using a narrow linewidth tunable slave laser; the main PLL uses a fiber frequency shifter rather than adjusting the frequency of the laser; and the loop error signal is developed by using a high frequency photomixer and electronic harmonic mixing rather than low frequency photomixing and optical

comb generation. In addition, the tunable slave laser has very precise open loop tuning and high resolution to support rapid frequency changes and phase lock acquisition.

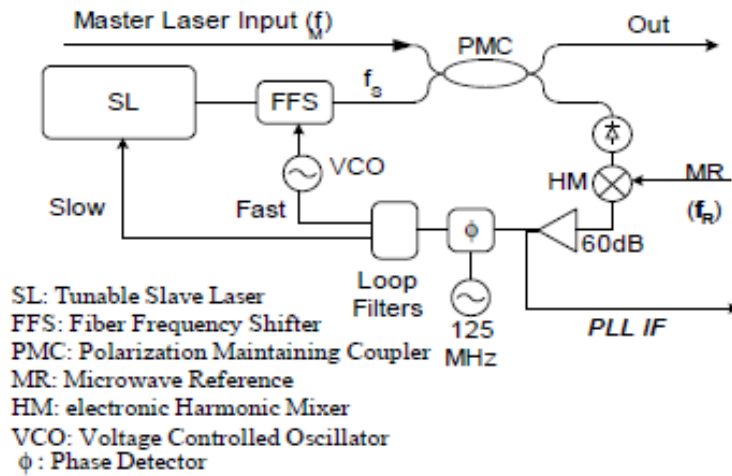


Figure I.2.2 Schematic of the laser synthesizer

As shown in Fig. I.2.2, the master and slave laser are combined in a polarization-maintaining coupler (PMF), so their polarizations are aligned. One branch of the coupler provides the output, while the other feeds a photomixer that recovers the difference frequency. (Not shown is the fact that 4 separate photomixers are needed to cover the whole 27-142 GHz frequency range. These are connected as required, along with matching harmonic mixers, by optical and electrical switches.) The microwave reference and harmonic mixer are used to down-convert the signal to 125 MHz. A conventional phase detector and Type II loop integrator then drive a voltage controlled oscillator near 100 MHz, which in turn drives a fiber-frequency shifter (FFS). The FFS is a commercial device modified to provide low acoustic delay of 100 nsec. To avoid having the slave laser drift beyond the range of the FSS (about 30 MHz), an additional slow loop drives a piezo-element that adjusts the frequency of the laser. A similar technique has been demonstrated earlier at a lower difference frequency [11]. Figure I.2.3 shows a test result for an assembly using this technique to phase lock the slave laser at 108 GHz difference frequency. The output is shown

in Fig. I.2.4 was measured at the laser synthesizer output by a W-band (75-110 GHz) waveguide photomixer and a spectrum analyzer outfitted with harmonic mixers for W-band operation. The RMS phase noise from 3 kHz to 3 MHz is 34 fsec for this measurement. This is thought to be mainly from the microwave reference, which was a laboratory instrument. Later measurements will include a custom designed low phase-noise microwave reference. The loop IF was also measured directly by the spectrum analyzer and that is shown in Fig. I.2.4. The IF noise was 0.013 radians from 10 Hz to 1 MHz. This indicates that there is some small amount of residual phase noise from the lasers. Extending the loop bandwidth is expected to further suppress this noise.

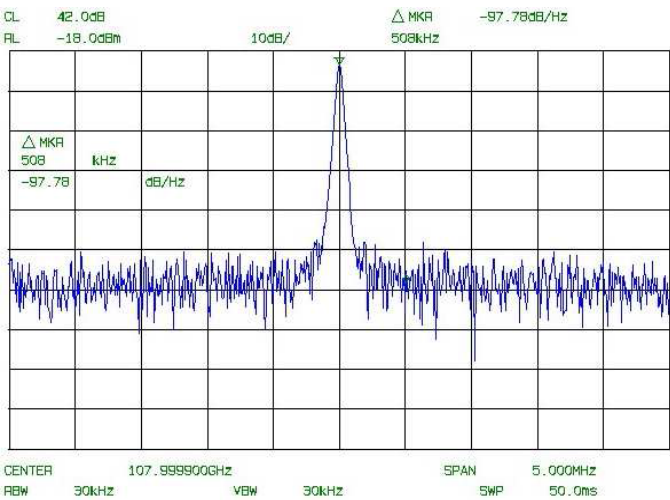


Figure I.2.3 – Laser Synthesizer Output at 108 GHz (after photomixer). The measurement noise floor -97 dBc/Hz limits the measurement above 200 kHz offset. CF=108 GHz, Span=5 MHz, RBW=30 kHz

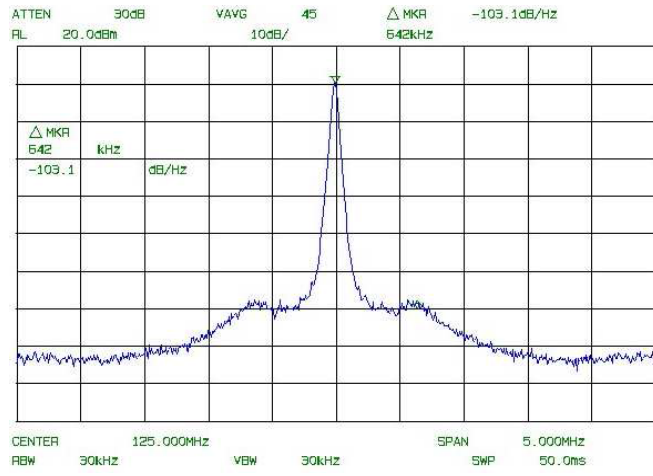


Figure I.2.4 –Laser Synthesizer Loop IF. Scale is 10 dB/div, RBW=30 kHz, noise marker at 542 kHz offset is -103.1 dBc/Hz

The above description of the photonic local oscillator will be needed to fully understand the proposed concept and prototype development of the optical phase correction covered in Chapter II and III.

PART B: The ATOMMS instrument

The Active Temperature Ozone and Moisture Microwave Spectrometer (ATOMMS) is an active aircraft to aircraft remote sensing occultation instrument that is designed to accurately measure and resolve the vertical profiles of temperature, pressure, density, water and ozone content of the atmosphere. The need for an instrument like ATOMMS is very essential to better understand and characterize our rapidly changing climate, and its evolving climate processes. Since the current water vapor and temperature remote sensing Earth systems do not provide accurate, complete. Each present global observation system has its own measurements limitations. At the same time they all share their biased estimates of water vapor, oxygen, and O₃ distributions and densities.

According to the National Academy Reports [12], it is crucial to ensure the existence of a long-term more definite observing system of variables such as temperature, precipitation, humidity, pressure, clouds and turbulence. Such systems should be able to provide a 10-100 years scale of variability and change. These set of systems should also be able to break the ambiguity of wet and dry components, as is the case for the existing GPS Radio Occultation systems, via measuring of the absorption of water-vapor, reduce ionospheric sensitivity with the use of much higher frequencies, eliminate the need of using boundary conditions and weighting factors of middle atmosphere climatology, and profile other constituents such as O₃ via absorption. Reference [13] covers in details the global measuring systems that are operating today and their limitations. The ATOMMS instrument remote sensor will bring unique new capabilities in vertical resolution, accuracy, to the global observation measurement techniques [14].

I.3.1 Scientific motivation

Global warming is already having significant and costly effects on our communities, our health, and our climate. The impact is easily and directly seen through all aspects: The increased coastal flooding and accelerating sea level rise, longer and more intensified wild fires, more frequent and intense heat waves, wide spread forest death in the rocky mountains, growing health impact since rising temperatures will proportionally **increase air pollution**, and **more intense allergy season**, the wider **spread of insect-borne diseases**, the list goes on. Global warming is the result of an intensified Green House Effect (GHE) which is directly due to the increase of the concentration of Green House Gasses in our atmosphere notably CO₂ and water vapor. Earth's natural greenhouse effect makes life as we know it possible. However, human activities, primarily the burning of fossil fuels and clearing of forests, have greatly intensified the natural greenhouse effect, causing global warming.

There are other indicators for global warming that should have been identified, studied and understood both through accurate climate observation system in one hand and correct climate models on the other hand neither that exist up to date. The latter is the main reason why the atmospheric scientific committee has failed to predict the current state of Earth climate and the projected one. .

In order to deepen our understanding of the current state of our climate and predict it's future behavior depends critically on our very detailed knowledge of the present distribution of atmospheric water vapor both in the troposphere and stratosphere layer of the atmosphere.

1. Large dynamic range and High Vertical Resolution of Temperature and Water Vapor Profiles

The Troposphere layer extends from ground to about 11 Km of altitude. The planetary boundary layer (PBL) was first defined by [15] is usually define as the lowest few Km that are directly modified by the underlying surface and directly influence by earth surface around 1 km deep, temperatures vary diurnally, unlike the free atmosphere above. PBL is characterized by a greater rate of change in its thermodynamic state than higher tropospheric altitudes on a time scale of 1 hr or less, where is the upper troposphere is characterized by much longer time constants. Large horizontal gradients in vertical wind speed and steep vertical gradients in water vapor and temperature in the PBL result in high-impact weather, including severe thunderstorms. High vertical resolution observation of these gradients in the PBL is important for improvement of weather prediction. Additionally high vertical resolution and accuracy of measured thermodynamic profiles, especially water vapor and temperature, are important for initialization of numerical weather prediction models.

Higher vertical resolution is essential since the average scale height of the troposphere is $\sim 1.5\text{Km}$ therefore a factor of 10~ 150 m would be the desired resolution in any measurement. The best claimed levels of vertical resolution using a passive, nadir-viewing system (e.g., AIRS, IASI, AMSU).claimed for these systems is on the order of 2 km. With the radio occultations technique for probing the atmosphere constituents the recent GPS occultation experiments [16], [17], [18], and [19] have demonstrated the ability of vertical resolution of ~ 200 m which is within the same vertical resolution of ATOMMS, however those GPS systems are limited to operate only in the upper troposphere) through the mid-stratosphere (limited by the ionosphere). In contrast,

ATOMMS temperature and stability will extend throughout the free troposphere through the mesosphere under any conditions.

ATOMMS will precisely profile water from the 1-4% levels in the LT to the ppm levels in the mesosphere with 1-10% individual profiles and absolute accuracies with averaging perhaps an order of magnitude better (depending on spectroscopy), while simultaneously profiling temperature to sub Kelvin accuracy over the same range. These dynamic ranges are orders of magnitude larger than the GPS RO which measures temperature OR water vapor, not both.

2. Upper Troposphere / Lower Stratosphere Retrievals

As mentioned earlier Water vapour as the most important natural greenhouse gas plays a key role in the global radiation budget. The strong temperature dependence of the saturation vapor pressure according the Clausius-Clapeyron equation (up to +7 % per Kelvin) leads to a strong positive feedback effect of the tropospheric water vapor on global warming e.g.[20] Schneider et al., 2010, and references therein). Therefore it is essential to understand the effects of increasing water vapor on circulations on all scales, which requires first of all to extend the knowledge about actual humidity distribution and circulation processes [21]. All the more important is the observation of the distribution of water vapor in the atmosphere. Microwave radiometry offers the opportunity of continuous observations throughout a large altitude range from surface to mesosphere (with a gap in the UT/LS-range) and under almost all conditions, except during precipitation [22].

Additionally; E. K. Oikonomou, A. O'Neill in [23] compared (ECMWF) 40-year Re-analysis named ERA-40 that is ozone and water vapor reanalysis fields during the 1990s with independent satellite data from the Halogen Occultation Experiment (HALOE) and Microwave Limb Sounder (MLS) instruments on board the Upper Atmosphere Research Satellite (UARS). He also compared ERA-40 has been with aircraft data from the Measurements of Ozone and Water Vapour by Airbus

In-Service Aircraft (MOZAIC) program. The finding of his comparison saw the upper stratosphere in ERA-40 has about 5–10% more ozone and 15–20% less water vapor. Most of the discrepancies and seasonal variations between ERA-40 and the independent observations occur within the upper troposphere over the tropics and the lower stratosphere over the high latitudes. He also points out the deficiencies in the way ERA-40 reproduces the water vapor signal in the tropical stratosphere.

Additional uncertainties in the current measurement systems uncertainties also exist between the models predicting the behavior of our climate. They seem to lean towards producing more water vapor in the upper troposphere in response to increased greenhouse gas concentrations and warming at the surface than may be occurring in the real world. Unfortunately we don't really know whether or not this is true because the water vapor and temperature observations in the upper troposphere are simply not good enough. ATOMMS profiles of temperature, geopotential height and moisture will extend from the lower troposphere to the mesopause with typical precisions over much of this altitude range of ~0.4 K, 10 m and 1-3%. With additional signal frequencies, other trace constituents such as water isotopes can be measured in the upper troposphere and above with similar performance.

3. Retrievals can be made in the presence of most clouds

Water vapor content is affected by increasing temperature, which affects the lapse rate, which affects the temperature again. Feedback loops such as this are important in determining the real world consequences of CO₂. Clouds, some positive (amplifying) and some negative (stabilizing).

Clouds: can be positive or negative feedback depending on what type of clouds form, because different clouds block incoming light and outgoing IR to different degrees: High clouds are warming (positive feedback) because they block little incoming light but have a big IR effect

(because they are cold, so re-radiate at low intensity) Low clouds are cooling: they have little IR effect (because they are low, thus closer to surface temperature) but are usually dense. Studying and understanding the mechanism of those feedback loops is also essential in determining the current status of our climate and the future prediction. Differences in the modeled effects of these details underlie the uncertainties in the forecast. That uncertainty extends within all current IR probing systems (e.g., AIRS, IASI) and MLS are limited in measuring under cloudy conditions since clouds create fundamental sampling problem due to high microwave absorption. ATOMMS will probe the 22 and 183 GHz water lines. Because absorption by *liquid* water in clouds is very large at frequencies near 200 GHz, observations near 200 GHz will be limited to altitudes above the freezing level (~ 5 km and above in the tropics and lower altitudes at higher latitudes). ATOMMS occultation signals near 22 GHz will be used to probe through liquid water clouds. The spectral shape and magnitude of cloud liquid water absorption near 22 GHz can be satisfactorily reproduced using two fitting parameters: cloud liquid water path and cloud temperature, this method has been developed for isolating and removing the liquid water clouds and ice is detailed in [24].

I.4. ATOMMS's Measurement configuration.

I.4.1 Radio occultation RO:

Radio occultation (RO) techniques have been developed for many years to study planetary atmospheres. The application to the Earth's atmosphere of these limb-sounding techniques provides an approach for global scale monitoring of tropospheric/ stratospheric temperature, pressure, and humidity profiles with high accuracy and vertical resolution, as well as ionospheric electron density profiles and scintillation properties. The concept is that when a radio signal passes through the atmosphere its phase is perturbed in a manner related to the refractivity along the ray path. Measurements of the phase perturbations can reveal the refractivity, from which one can then derive such quantities as atmospheric density, pressure, temperature, moisture, geopotential heights, and winds. The concept can successfully work for earth's atmosphere and frequencies less < 300 GHz where refractivity is defined by Clausius-Clapeyron equation (up to +7 % per Kelvin) as:

$$N = \frac{77.6P}{T} + 3.73 * 10^5 * \frac{P_w}{T^2} \quad (2)$$

The first term is the Hydrostatic balance where P is the total pressure (mb) and T is the temperature (K), the second term is the Moisture where P_w is the water vapor pressure (mb) and N = (n-1) X10⁶.

The above technique can produce very accurate density and temperature profile in the upper troposphere through the stratosphere altitudes because the contribution of moisture in these heights is negligible. On the contrary, in the lower half of earth's troposphere, water vapor contributes significantly to the index of refraction where additional information such as temperature from a weather analysis is required to determine the wet and dry contributions to the

index of refraction. Given present knowledge of atmospheric temperature to roughly 1.5 K, one can derive moisture from GPS occultations to an accuracy of roughly 0.1–0.2 g/kg, which is useful in the lower to middle troposphere [25].

I.4.2 ATOMMS operational Concept

The technique in I.4.1 is powerful, but not perfect since it assumes that the temperature and pressure profile produced are perfect, which is not the case. Accordingly, if we add additional remote sensing capability that directly measures the absorption of the constituents of moisture and temperature independent of models with the accuracy and vertical resolution of the GPS refractivity profiles will reduce the uncertainties of the determining the profiles of all constituents.

The ATOMMS System does exactly that, it measure both the phase and amplitude of monochromatic signals within a 22Ghz band - and 183-GHz band where water and other atmospheric constituents have absorption spectral lines. From the measured phase and amplitude, we can derive profiles of both the speed of propagation and the attenuation due to water absorption respectively and in turn solve for the wet and dry density profiles directly from the occultation observations. Below is a summarized description of how the measurement is done, however the detailed derivation and error analysis is well covered in [26]. Using Beer’s law for absorption a long an optical path

$$I=I_0 e^{-\alpha d} \tag{3}$$

Where

I = is the intensity of the received signal passing through the atmosphere

I_0 = is the intensity of the received without the atmosphere

$\alpha d=\tau$ is the optical depth integrated along the signal path through the atmosphere.

The optical depth relates to the extinction ratio k as below:

$$\tau = \int k dl$$

The desired quantity is the radial profile of the extinction coefficient, $k(r)$. Given k and N as functions of r , the distance from the center of curvature (approximately the center of the Earth), we can derive a radial profile of atmospheric water >> change formulas (should be (4) and (5) π and π

$$\tau = \int k dl = 2 \int_{r_0}^{\infty} k \frac{nr dr}{(n^2 r^2 - n_0^2 r_0^2)^{1/2}} \quad (4)$$

$$k = - \frac{1}{\pi} \frac{da}{dr} \bigg|_{a=a_0} \int_{a_0}^{\infty} \frac{d\tau}{da} \frac{da}{(a^2 - a_0^2)^{1/2}} \quad (5)$$

Equation (4) (represents the forward problem of the extinction coefficient integrated along the occultation path. Equation (5) is the inverse relation allowing us to derive the extinction coefficient profile from the measured, path-integrated optical depth. Equation (5) can be derived from (3) via standard abel integral transform pair relations [27]. Parameter a is the asymptotic miss distance as shown in Figure I.3.1 defined as $a = nr \sin(\theta)$, where θ is the angle between the ray path and radial direction. Note that a is a constant for each ray path under the assumption of spherical symmetry and is derived from the atmospheric Doppler profile as described in [28]. Then k is derived as a function of r in (4) using the fact that $a_0 = r_0 n(r_0)$, where r_0 is the tangent radius of the ray path such that θ is $\pi/2$ and $n(r_0)$ is derived from the bending angle profile via the standard Abel equation.

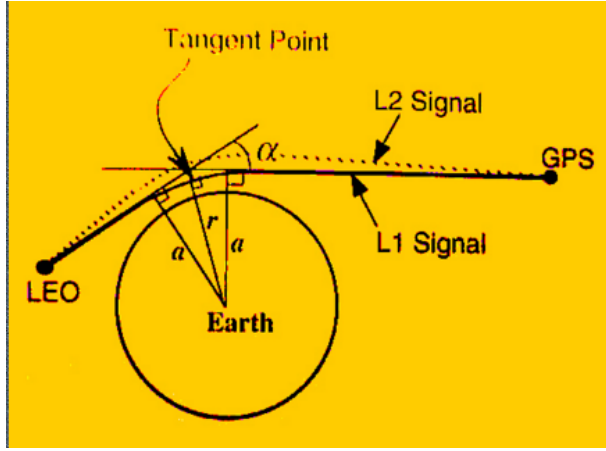


Figure I.4.1 The two satellites occultation geometry

As indicated earlier ATOMMS will measure the atmosphere absorption at different frequencies, one freq will be set at the center of the absorption profile and the other is off the absorption profile, therefore the optical depths difference between those frequencies is described in (6)

$$\tau_{21} = \tau_2 - \tau_1 = \frac{I_{10}}{I_1} - \frac{I_2}{I_{20}} \quad (6)$$

Subscripts 1 and 2 refer to two frequencies f_1 and f_2 . The resulting extinction coefficient profile derived from (5) will be $k_1 - k_2$. k will be measured at different frequencies and ratio them to remove any common mode noise effects. Deriving $k(r)$ will give us the imaginary part of the index of refraction $N''(r)$ since $k(r) = 4\pi N''(r) / \lambda_0 \times 10^{-6}$ and complex index of refraction is $N_c(r) = N'(r) + jN''(r)$.

The next step is to deriving the real part of the index of refraction $N'(r)$. As stated earlier ATOMMS will measure the Doppler frequency. The 13 GHz system will measure the Doppler frequency $\Delta f_{\text{aircrafts}}$ due to the relative velocities ΔV of the aircrafts while descending through the atmosphere. However, in order to isolate $\Delta f_{\text{aircrafts}}$ from the overall Δf ($\Delta f_{\text{atmosphere}} + \Delta f_{\text{aircrafts}}$), the aircraft velocities must be measured very accurately. We do that with very low noise accelerometers GPS position error is = 1 cm, maximum decedent time through 100 m of height

estimated to be 100 sec (which is chosen as an integration time). Therefore the velocity error need to be ~ 0.1 mm/sec. which is a requirement for the accelerometers, model EndeVCO 86 should meet that.

From the above velocity error, the bending angle $\alpha (r)$ error is determined via the reverse process and $N'(r)$ is then calculated. Therefore, from the two profiles of two observables, $k_1(r) - k_2(r)$ and $N'(r)$, we can derive temperature (T), total pressure (P_t), and partial pressure of water vapor (e) by simultaneously solving three equations: the refractivity equation (2), the hydrostatic equation, and the following absorption equation

$$k_1(r) - k_2(r) = F(f_1, f_2, P_t, e, T) \quad (7)$$

where f_1 is positioned on the line to measure absorption and f_2 is positioned offline to calibrate out unwanted effects.

I.4.3 The ATOMMS Instrument

A high- level ATOMMS instrumental configuration is shown in Figure (I.4.2), it shows only the 13 GHz, 22 GHz and 183 GHz Transmitters and receivers systems in each aircraft. Each aircraft consist of the following systems as shown in Figure (I.4.3),

1. ATOMMS microwave instrument 13 GHz, 22 GHz and 183 GHz transmitters and receivers:
2. ATOMMS precise positioning system hardware consisting of a GPS receiver a 3 axis precision accelerometer system on each aircraft.
3. The WB57F aircraft
4. WAVE gimbal built by SRI for NASA that points the ATOMMS microwave instrument.

Not shown are the ATOMMS retrieval system and the precise positioning system software

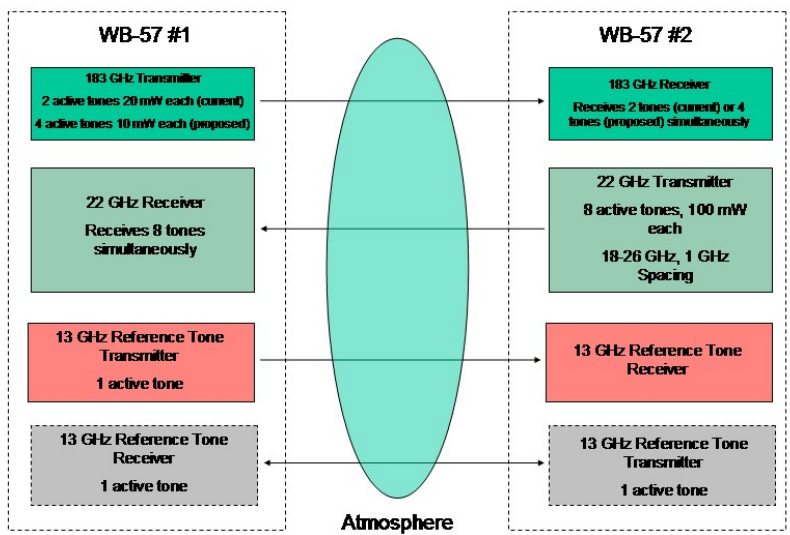


Figure I.4.2: ATOMMS experiment configuration. The two payloads are referred to as ATOMMS-A and ATOMMS-B.

The operation of the ATOMMS instruments is described as follows: Each microwave transmitter located in ATOMMS transmitter located in ATOMMS A or B radiates several monochromatic signal tones through quasi-optics lens system in which the design of is described in more details in Chapter IV and V. Those radiating signals pass through the atmosphere and then are received by the receiving antennas in the receiver that is on the opposite side of the atmosphere as shown in Figure I.4.2 The RF signals are down-converted into IF signals, then digitized and records the signals. The data is retrieved after the occultation is complete. With ATOMMS microwave system the absorption of water or other desired atmosphere constituents are simultaneously measured with the 22 and 183 GHz systems which is adds a key advantage in the dynamic range allowing the profile of the gasses from the ground surface into the mesosphere as well as measure ozone at 195 GHz in the upper troposphere and middle atmosphere. The absorption lines are retrieved from the 22 GHz and 183 GHz TX/RX pairs while the phase information is retrieved from the 13 GHz dual; TX/RX. From the latter the

bending angle is found. Combining the amplitude and phase with the accurate measurement of the ATOMMS A and B The ATOMMS retrieval system later derives the phase and amplitude of the signals and combines them with the precise knowledge of the transmitter and receiver positions found using the GPS on board of each aircraft, then we can derive profiles of atmospheric moisture, ozone, temperature and pressure.

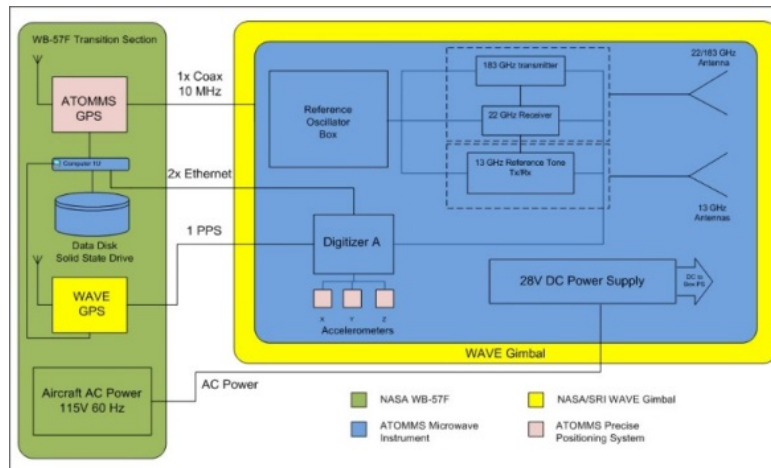


Figure I.4.3: Block diagram of the ATOMMS A aircraft. With the exception of the science tone complement, ATOMMS B is identical.

I.5. The Microwave Instrument

I.5.1 22 GHz frequency

The 22 GHz TX/ RX consist of 8 fixed microwave tones. The frequencies are selected such that the absorption spectra of water around the 22.25 GHz is profiled during the occultation. Figure (I.5.1) shows the Zenith opacity of water vapor at different microwave frequencies.

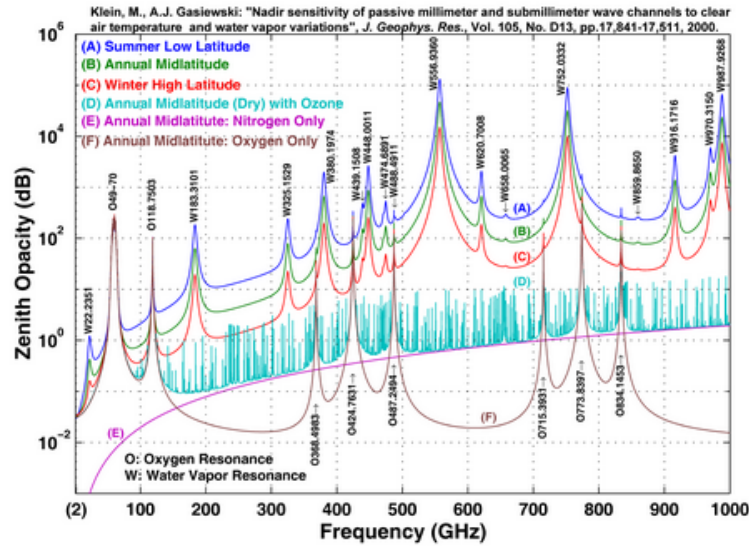


Figure (I.5.1) Microwave Absorption spectrum for water vapor at different

Figure I.5.2 shows the block diagram of the 22 GHz transmitter and receiver with the detailed of parts used and most important specs. The transmitter employs eight separate phase locked YIG oscillators to generate the frequencies 18.5, 19.5, 20.2, 21.5, 22.5, 23.5, 24.5 and 25.5 GHz that are driven by 100 MHz reference. The center frequencies of all oscillators are shifted by 40 KHz from the center frequencies of the corresponding oscillators in the receiver. All signals are monitored before they are power combined by an 8:1 combiner. The TX amplifier then amplifies the combined signals to a level of ~100 mW per tone. The amplifier is operating at 1dB below the gain compression point as shown in the diagram. This scheme is chosen where 1 common amplifier is used in order to eliminate any differential noise occurs between the 8 microwave paths. The amplified signal is the fed to rectangular waveguide, then into a rectangular to circular waveguide, linear polarizer then fed to the corrugated feed horn. As we will discuss in the rest of the quasi-optics design, the output beam from the feed horn will illuminate the lens antenna. After the signals travel to ATOMMS B, the beam is focused into the receiver feed horn of ATOMMS B. As Figure 4 shows, the beam passes through the waveguide system into the RX

amplifier that amplifies all eight received tones. The amplified signal is then power divided into eight channels. Then we use a bandpass filters in each channel to isolate a single received tone. These tones are then mixed with LO signals generated by YIG phase locked oscillators fed with a reference from a DDS synthesizer. This synthesizer is used to offset the frequency of the LO, generating a ~ 40 kHz IF frequency. The low frequency IF is then low pass filtered, and amplified with a low noise audio frequency amplifier. The IF is then fed into a National Instruments Compact RIO real-time data acquisition system, where the time domain waveform is digitized and recorded. This data acquisition system has been shown to operate at ambient pressure in the WB-57F in previous experiments.

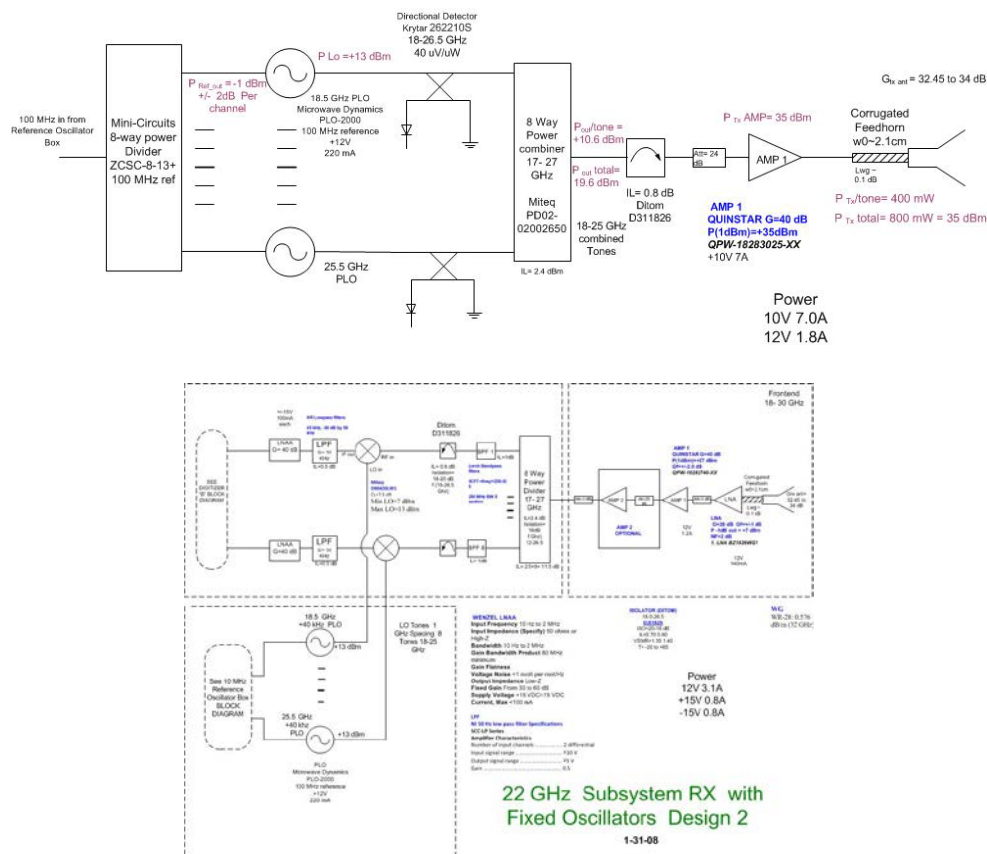


Figure (I.5.2) The ATOMMS 22 GHz transmitter (top) and receiver (bottom)

subsystems. Only 2of the 8 channels are shown in each block diagram.

I.5.2. 13 GHz frequency

The 13 GHz reference tone transmitter and receiver are similar to the 22 GHz system, but in each ATOMMS A and B there is a pair of TX and RX since this system is primarily used to measure the bending angle that is used to retrieve the index of refraction as shown in Figure (I.5.4). The bending angle is calculated by first measuring the phase difference between the Transmitted signals which from we can derive the Doppler shift versus time. To meet our accuracy goals, the 13 GHz signals need to be extremely phase stable. The expected the limiting error in determination of the atmospheric Doppler shift to be due to uncertainty in the estimation of the line of sight velocities of the aircraft, which is specified to be 0.1 mm/s or less. Digitized laboratory measurements from one of the 13 GHz transmit-receive chains has been analyzed for phase stability as a function of the signal integration time as shown in Figure I.5.5

The phase error has been now translated into units of mm/s. The figure shows that for integration times greater than 0.5 s, the instrument performance is an order of magnitude better than the expected error in the line of sight velocity determination. The plan is to use integration times of 1-10s for signal extraction; the phase error of the 13 GHz signals is well within specification.

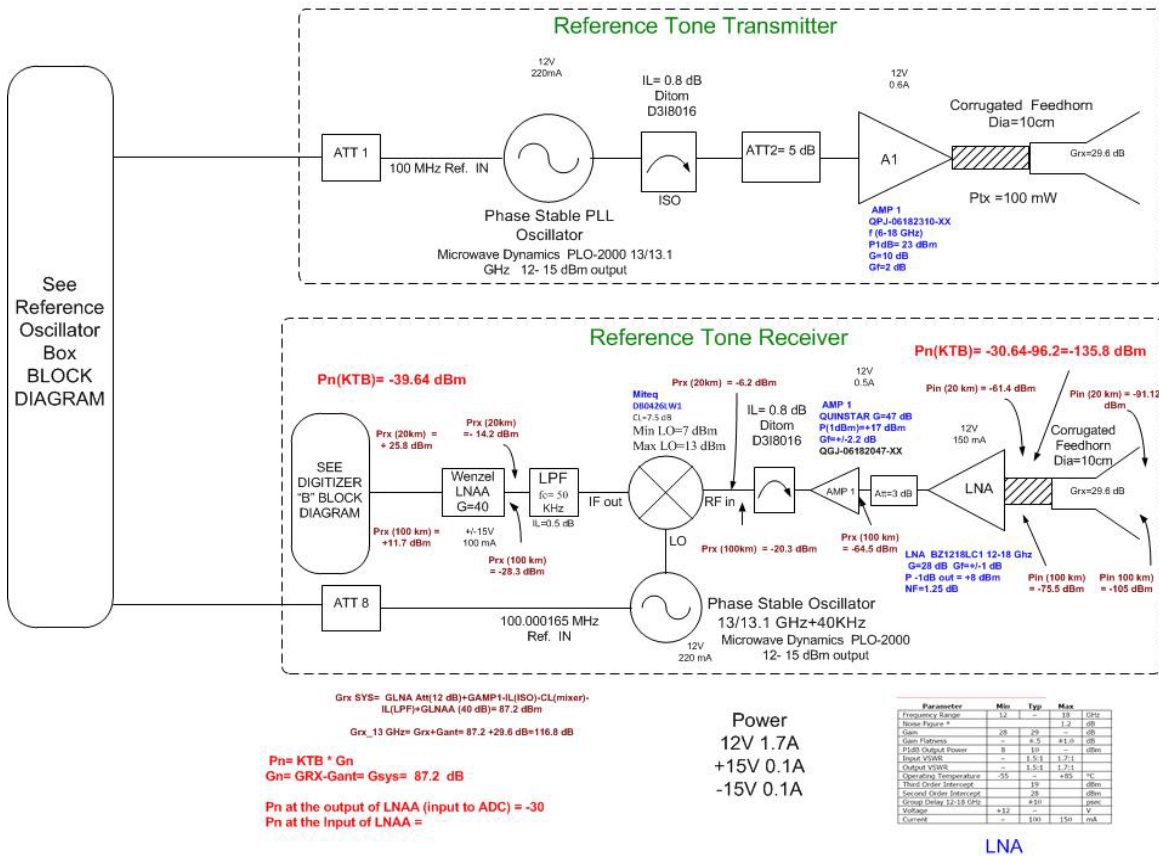


Figure (I.5.4) The ATOMMS 13 GHz transmitter (bottom) and receiver (top)

subsystems. Two of the eight channels are shown in each block diagram.

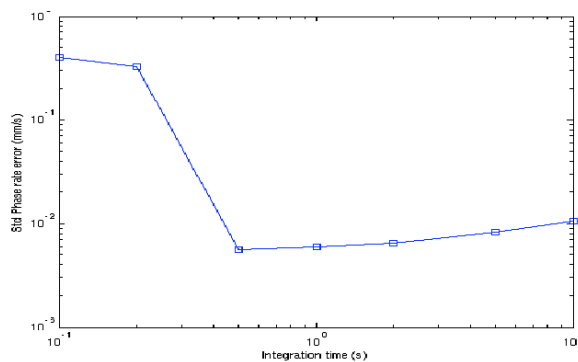


Figure I.5.5.: Standard deviation of the phase rate error for a 13 GHz signal generated and transmitted from one ATOMMS device, then received and digitized by the second ATOMMS device before processing

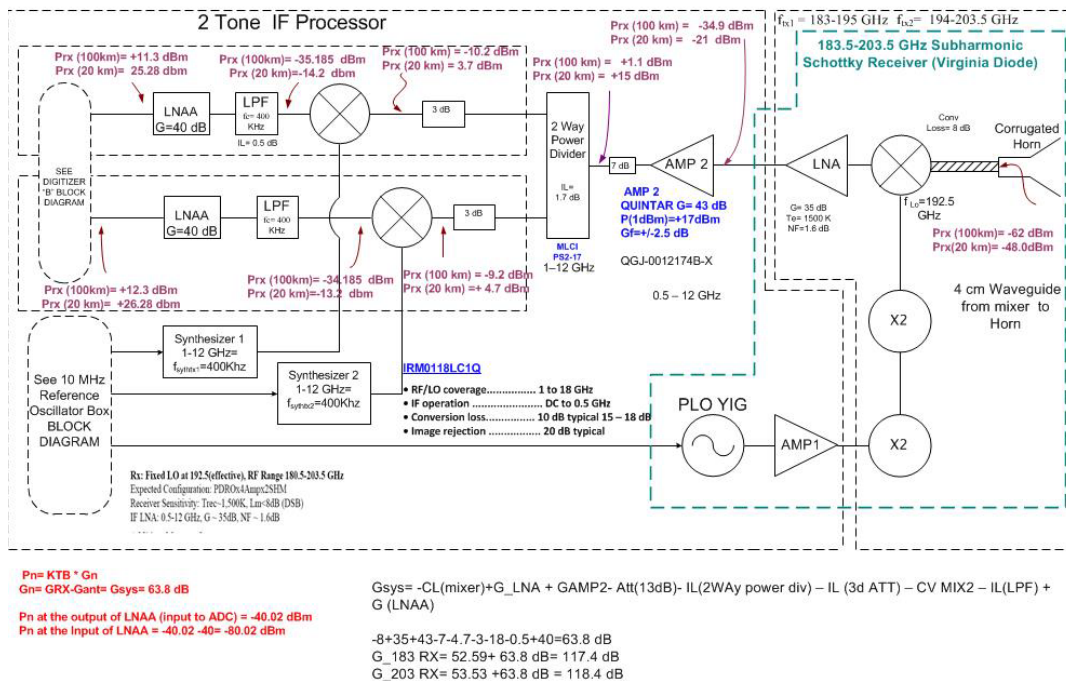
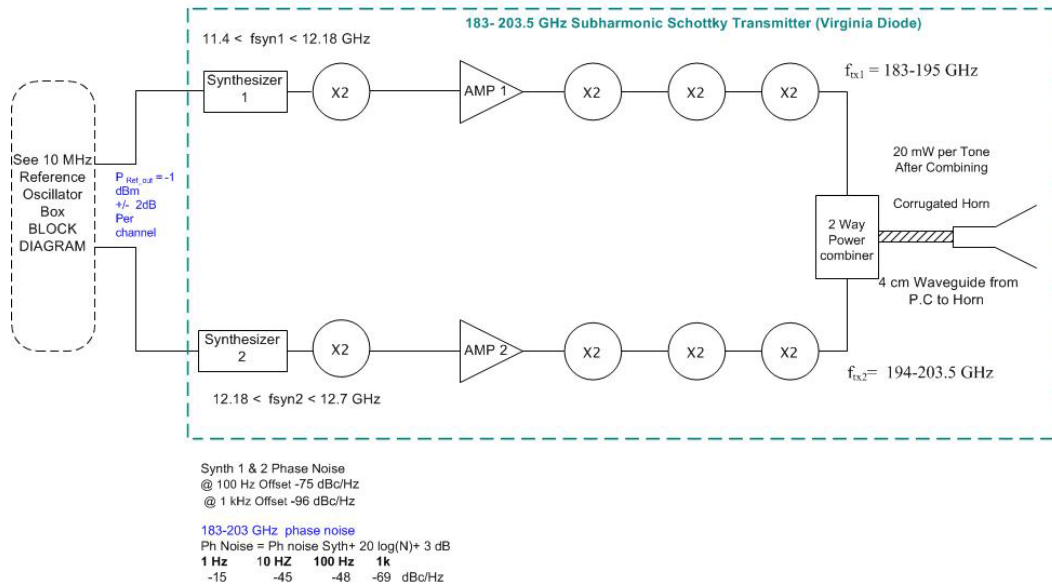


Figure I.5.6: The ATOMMS 183 GHz transmitter (top) and receiver (bottom) system block diagrams.

I.5.3. 183 GHz frequency

The 183 GHz subsystem is based on a two tone transmitter and subharmonically pumped Schottky mixer receiver front end from Virginia Diodes. The transmitters each provide 40 mW

of power from 180-203.5 GHz, and are power combined using a waveguide magic tee. Power monitoring diodes before the magic tee record the transmitted power level of each channel, for later removal of differential amplitude effects. After power combining, the transmitted power is ~20 mW per tone. The subharmonically pumped Schottky receiver has a measured noise temperature of ~1100K, and is flat across the band. A low noise amplifier with a 1-12 GHz bandwidth relays the IF signal to a downconverter module. The receiver IF downconverter is identical in architecture to the 22 GHz receiver system with the exception that tunable synthesizers are used to generate the LO signals rather than fixed tuned oscillators. Block diagrams of the 183 GHz subsystem are shown in Figure I.5.6.

A detailed link budget simulated the performance of the instrument using realistic antenna parameters and estimated losses. This link budget was used to specify all the components of the ATOMMS transmitter and receiver systems please see APPENDIX A for details of the link budget.

Figure I.5.7. shows the ATOMMS-A instrument, completely assembled and awaiting system testing. With fully assembled electronics modules, we have completed testing of the electronics systems at the box level, and we are now verifying that instrument performance meets the specifications necessary to accomplish the scientific mission.

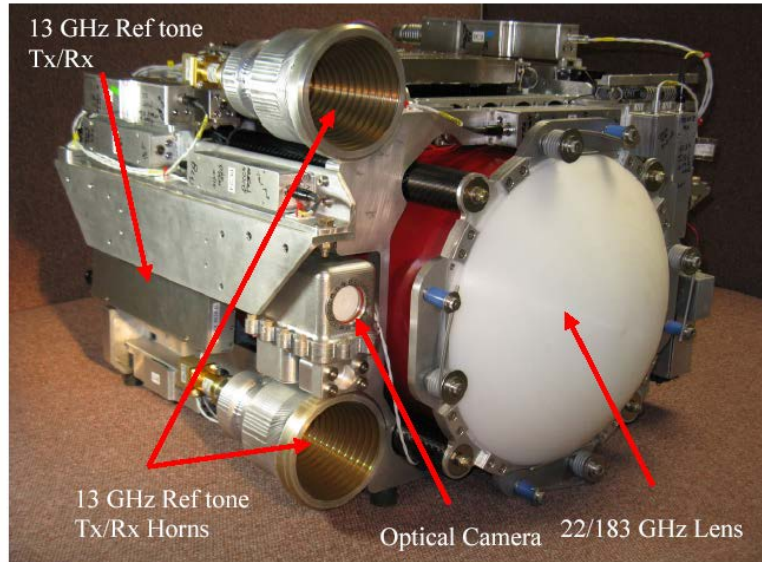


Figure I.5.7: The fully assembled ATOMMS A instrument. Visible components are labeled. The 183 GHz Tx and 22 GHz Rx modules are not visible.

I.6. Precise Positioning System

From the occultation geometry shown in Figure (I.6.1) the aircraft to aircraft occultations. The atmospheric Doppler shift is much smaller than for the spacecraft occultation case because the aircraft move much slower (~ 200 m/sec) than the spacecraft (several km per

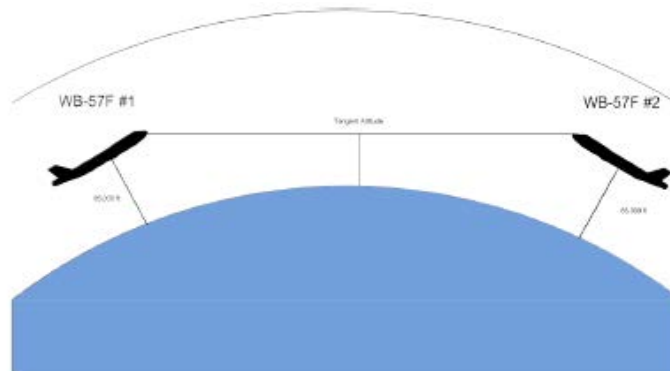


Figure (I.6.1) An the aircraft to aircraft occultations

second). At the uppermost altitudes, just below the altitude of the aircraft, the atmospheric bending angle is quite small. Therefore the atmospheric Doppler shift is quite small. In order to precisely determine atmospheric temperature and pressure, the ATOMMS system must measure very small bending angles at high altitudes. The system goal is to estimate the motion of the aircraft to an accuracy of 0.1 mm/sec.

Over the course of the experiment design, we refined our understanding of the necessity of this goal and how to achieve this small error. The ATOMMS Precise Positioning System consists of accelerometers and GPS receiver on each aircraft. Positions can be estimated very accurately from the GPS receiver data about every 100 seconds. In profiling the atmosphere via the ATOMMS occultations, we determined that we will use integration times of ~10 seconds or less. To achieve the high vertical resolution and performance over these short intervals, we determined that very accurate accelerometers must be used. Essentially the precise reconstruction of the time-varying aircraft positions and velocities will integrate the acceleration measured by the accelerometers to obtain the velocities of the two ends of the ATOMMS instrument. The GPS receiver data will essentially be used to estimate the bias and scale factor of the accelerometers. Extremely low-noise accelerometers (Endevco Model 86), developed for seismic research, were selected for the ATOMMS experiment after extensive analysis by the ATOMMS team at the University of Arizona and JPL.

High performance GPS receivers have been selected that could satisfy the ATOMMS requirements that were also familiar to JPL. The receivers already in the WB-57F aircraft were deemed insufficient to deliver the quality of phase data needed. JPL suggested a high performance Ashtech receiver that they use for other applications.

I.7 WB-57F Aircraft

NASA has been providing the WB-57F aircraft time for the ATOMMS experiment. ATOMMS presently holds two flight slots in the WB-57F schedule, and a third is planned to be added.

Currently, the first flight slot is a combination engineering test flight, followed immediately by an air to ground RF testing flight series. The second is a full up air to air, two aircraft flight test series. A minimum of 3 flights are anticipated for each flight series. As a risk reduction measure, it is planned to separate the engineering test flights and air-to- ground single aircraft test flights, allowing more time to address any issues identified in the engineering test flights.



Figure I.7.1: The WAVE system mounted on the nose of a WB-57F. ATOMMS will replace the optical telescope in this system. A microwave transparent radome will replace the front skin and optical window.

In support of these flight tests, Southern Research Institute and the University of Arizona have been defining the desired flight plans for each flight series, along with the task load for the WB-57 flight backseat operator (FBO).

The following chapters will cover the optical design and characterization for the two instruments that we performed. Chapter II and III will discuss the optical phase correction for the Photonic

Local oscillator signal as it is transmitted down the fiber to each antenna and Chapter IV and V will cover the quasioptics design and analysis of ATOMMS instrument.

Chapter II: Optical phase correction/stabilization for ALMA Photonics LO [Early Development]

In this chapter we will first review some of the existing methods used to measure and control phase in optical fiber and lay out the foundation of how we choose the design that is most suitable to stabilizing the phase for the Photonic LO. Then we will define the major physical factors that will impact the change of the Photonic LO phase. In the preceding section we will evaluate the concept by testing the OPSIF system using a high stable laser from collaborators in Japan with only fiber that is not moving. Followed by this we will be describing and analyzing some of the technical challenges and specifications limitation that this design have, specifically looking into the dispersion effects in optical circulator and how it will impact the performance of the phase correction in fiber.

II.1 Optical phase correction Background on existing approaches

In this section I will review the state-of-the-art of optical phase measurement and correction in fiber, and we will find that the ALMA phase drift specification requires an order of magnitude improvement over the most advanced systems that have been previously built.

1. The Smithsonian Astrophysical Observatory (SOA)

The SOA operates the Sub-millimeter Array (SMA) on Mauna Kea. This is a six element interferometer with a similar frequency coverage as ALMA [29]. The SMA does not use an active phase correction. The longest baseline for the SMA is less than one km. In addition, the fiber that they use for distribution is a special, expensive, fiber with extremely low temperature coefficient of phase. The secondary coating of the fiber is made from a liquid crystal polymer with a negative thermal expansion coefficient which compensates the positive expansion coefficient of the silica glass core [30]. This fiber has a temperature coefficient that is in general less than 1 ppm/deg C, but at the mean ambient underground temperature on Mauna Kea (5.5C) it is less than .03 ppm/C for small deviations. Using this fiber, and a special torsionally controlled azimuth fiber wrap, the

SMA hopes to achieve phase drift of less than 10 microns per hour. This special fiber was discontinued by Sumitomo and is now reportedly manufactured by Furukawa. However, it would be of limited use for ALMA since the cost would likely be prohibitive and the phase drift would still be much larger than the ALMA goal.

2. Optical carrier modulation scheme

Several groups have done some version of a round trip phase correction based on a microwave reference modulated onto an optical carrier. Previous work at NRAO includes a round trip phase measurement scheme using the microwave reference technique [31]. Using a 500 MHz modulation, and simple inexpensive components, the technique was used to measure phase with resolution below 1 psec. A similar technique has been used at Jet Propulsion Lab (JPL) and National Astronomical Observatory of Japan (NAOJ) using more expensive components such as a narrow linewidth laser for transmission and an optical modulator [32,33]. The JPL work was a reference frequency distribution for the Cassini-Deep Space Network experiments. The highest frequency used in the experiment is 32 GHz and the longest fiber length is 16 km. In this case an optical wavelength of 1310 nm was used and the modulation frequency was 1 GHz. The signal is detected, frequency shifted, and retransmitted at the antenna end. The returned signal is detected, phase compared to the outgoing signal and then used to drive a temperature controlled spool of fiber so that the round trip phase is unchanging. This system has resulted in phase stability of approximately 100 fsec on time scales from a few minutes to a few hours. The NAOJ work was similar, except a 1.4 GHz microwave carrier was used and 100fsec phase drift was measured over only 100m of fiber. Neither of these techniques would meet the ALMA specification. Also, on shorter time scales, changes in fiber length due to antenna motion or cable wrap perturbation

would be corrected very slowly (tens of seconds) by either of these techniques. There is also a commercial company that sells products meant to send coherent timing signals by fiber. A paper on that is available on their web site describes their measurement/correction system that is based on comparing the phase of a microwave modulated reference signal over fiber [34]. Their system achieved an RMS phase stability of 650 fsec. Both the EVLA and CARMA (Combined Array for Research in Millimeter Astronomy) have plans to do real-time measurement of the fiber round trip path delays [35- 36]. These measurement systems will be similar to the NAOJ and JPL systems, except that the phase correction is not applied to the fiber but rather in the backend. The ALMA phase drift specification of the fiber is 0.09 degrees at 119 GHz, which is 0.6 microns or 2.1 fsec which is less than half of a wavelength at the 1.55 micron optical carrier wavelength. For the longest fiber length contemplated for ALMA (25 km), 0.6 microns implies a fractional fiber length stability of 2.4×10^{-11} . All the case of phase measurements reviewed falls well short of the needs of ALMA.

II.2 Characterization of the physical factors affecting the LO phase error and the ALMA instrument coherence.

The fiber drift has two components, drift due to the above ground fiber which is exposed to diurnal temperature fluctuations, and drift due to the buried fiber which has much lower temperature fluctuation. Several sources have reported on the phase vs. temperature coefficient of single-mode fiber [37-39], which is approximately 8 ppm per degree C for bare single mode fiber. Other reports have measured cabled fiber of various types [40], with temperature coefficients ranging from 10 ppm-60 ppm per degree C. For purposes of estimating the maximum likely propagation delay due to temperature for the ALMA fiber, we will assume a worst case value of 15 ppm per degree C. This is likely to be an upper value on the cabled fiber. In ALMA memo #314 [41], the predicted

maximum diurnal temperature variation is .006 deg K for fiber buried to a depth of 1-meter. The above ground maximum diurnal temperature change is 30 deg K. These values were used along with a fiber temperature coefficient of 15 ppm/deg C to predict the expected fiber uncorrected path length changes [42]. That result used a longest fiber path length change of 25km. However, in the latest ALMA configuration planning, the so-called Y+ configuration is expected to have a longest baseline of 20 km [43], so the longest distance from the central building to an antenna will be about 10km. We will assume a longest fiber path length of 15 km to account for curves and spurs in the fiber routing, and recalculate the result from [38]:

Expected Fiber Path Length Change per day	
Elapsed Time	1 Day
Length change, 15km buried	1.3 mm
Length change, 25m above ground	11.2mm
Total length change	12.5 mm

Table II.1 Expected Fiber Path Length Change per day

This will be again recalculated using a shorter time scale of one hour. The underground temperature fluctuation in one hour should not exceed 1.6mK, and the above ground temperature change should not exceed about 5 K per hour [Ref. 41, Fig. 9]. We then get:

Expected Fiber Path Length Change per hour	
Elapsed Time	1 hour
Length change, 15km buried	0.36 mm
Length change, 25m above ground	1.9 mm
Total length change	2.26 mm

Table II.2 Expected Fiber Path Length Change per hour

In either case, the fiber path length change is dominated by the above ground sections. From previous work [36] it has been found that a large phase drift component was added by sections of fiber in and near fiber manholes. For ALMA, care must be taken to minimize the above ground

fiber run lengths and to insulate the fiber manholes so as to reduce the amount of compensation required in the round trip phase correction.

II.3 Technique used of optical phase stabilization for the ALMA Photonic LO

The chosen technique should be able stabilize the electrical length of the optical fibers used to distributed the LO reference signals from the center to each antenna which requires high resolution phase measurement. To achieve this, we chose to do this phase comparison directly at the optical wavelength, where the frequency is approximately 10^5 higher (at 200 THz) than in the other techniques. Phase comparison of an unmodulated lightwave is done by using a fiber optic Michelson interferometer. The optical length stabilization technique is dependent on use of a frequency-stable and Ultra-narrow master laser. This concept requires that the frequency of the master laser be maintained constant to better than $(1\mu\text{m}) / (25\text{km}) = 4\text{e-}11$. Such stability is required over time intervals of at least 100 sec, and preferably longer. In addition, the short term stability must be sufficient to maintain good coherence over the round-trip path of up to 50 km of fiber, or an interval of about 240 μ sec.

Using a very stable laser constructed at the University of Electro Communications (UEC) [46] in Japan, which has a very good long term stability and reproducibility of about 2×10^{-13} and 2.5×10^{-11} respectively. The UEC master laser achieves this good long-term stability by frequency locking its internal laser (an external cavity diode laser) to a molecular line, namely that of acetylene (C_2H_2) at 1542.3nm. Low-pressure C_2H_2 is contained in a glass tube that is embedded in a Fabry-Perot cavity. The cavity is first locked to the saturated, Doppler-free absorption line of the gas, and then the laser is locked to the cavity. To achieve the cavity-to-gas locking, it is necessary to modulate (or dither) the cavity length slightly. This causes frequency modulation of the laser

output at a rate of 1.6 kHz and a deviation of approximately ± 250 kHz. This modulation turned out to be a limiting factor in our tests.

Therefore the test instrument was brought to Japan and a series of measurements was made using the UEC laser with the goal of verifying the accuracy of the length stabilization technique. The tests allowed us to set an upper limit on the delay variation in the stabilized path of about 70 fsec over 1 hour. It is possible that the system meets the ALMA goal of about 6 fsec delay variation (1.26m fiber length variation) over at least 100 sec, but establishing this was beyond the limits of these tests.

II.3.1 Illustration of the proof of concept

A simplified block diagram illustrating the basic principles of the test is shown in Figure II.3.1. A tunable laser (“slave laser”) is phase locked to the master laser (UEC Laser) at an offset frequency determined by a microwave synthesizer. The master and slave optical signals are combined onto a single optical fiber, passed through the line length correction (OPSIF) assembly, then through the long fiber, then through a turn-around assembly, and then to a photodetector. The photodetector output is compared with the microwave reference in a phase detector, and the measured phase difference is recorded. The turn-around assembly takes a portion of the received light, shifts its frequency slightly, and launches it back toward the OPSIF on the same fiber. The OPSIF compares the returned light with the outgoing light at the master laser wavelength and drives a variable delay unit (fiber stretcher) so as to keep the phase difference constant.

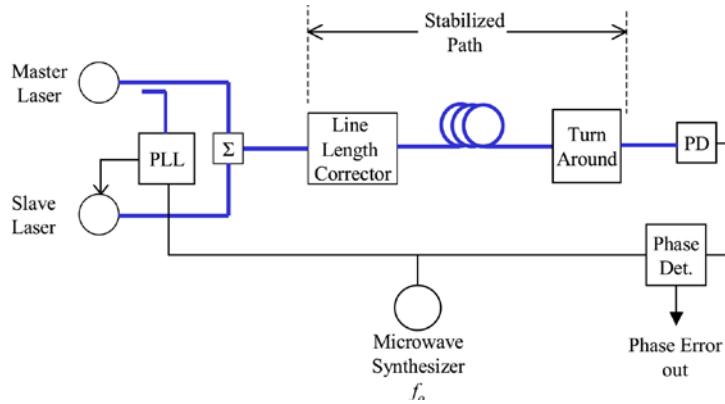


Figure II.3.1 Basic principle of the test.

II.3.2 Experimental setup

Figure II.3.2.1 shows the actual test arrangement. Most of the test set components are contained in a single rack-mountable box (“NRAO Test Box”) of dimensions 173x486x541 mm. The internal block diagram of this box is shown in Figure II.2.2.3. It contains the slave laser phase locking circuitry, the length correction system, the high frequency photodetector for the beat note, and a phase detector (double balanced mixer). The box implements, in one place, both the central components and the antenna-based components of the ALMA reference transmission system. Optical signals from the two lasers are brought into the box via Diamond E2000/APC connectors.

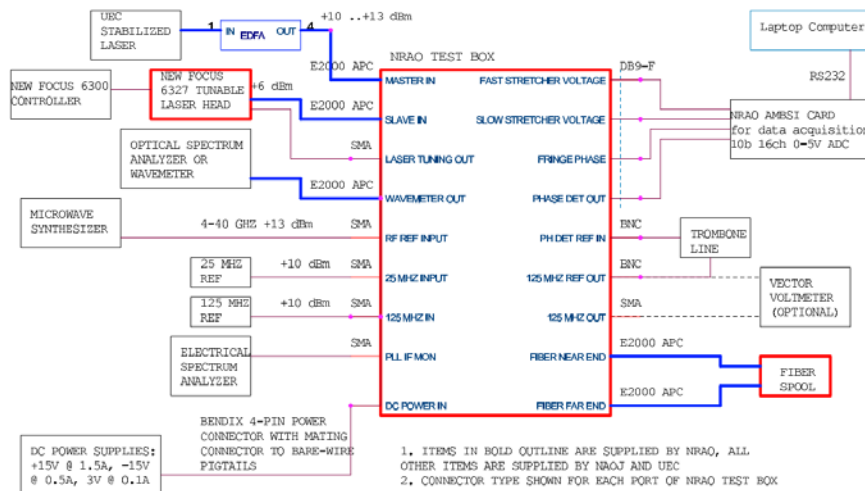


Figure II.3.2.1 The actual test arrangement

The slave laser, a New Focus Model 6327H external cavity diode laser, is coarsely tuned to the desired frequency using a New Focus Model 6300 Tunable Laser Controller. To facilitate this, the combined signal from both lasers is brought out via a separate connector (“Wave Meter Out”) for connection to an optical spectrum analyzer or wavemeter. The slave laser head has been modified by NRAO to provide a d.c. coupled bias offset input. This is used to provide fine tuning for phase locking, and is driven by the PLL integrator inside the box.

When the PLL is locked, the slave laser frequency will be offset from the master by $f_0 = f_1 + f_2$.

These reference signals should have good short term stability, but they need not be phase locked to each other. They were provided by separate Agilent synthesizers. In all of the tests reported here, $f_1=26.5$ GHz and $f_2=125\pm 5$ MHz. The combined signal from the two lasers is passed through a voltage-variable delay with a range of about 5 mm (implemented by two piezo-driven fiber stretchers), and then to an output connector (“Fiber Near End”). A spool of optical fiber then simulates the long transmission path required by the ALMA telescope. The length of fiber can vary from less than 1 m to a maximum that is limited by the master laser’s coherence. After the fiber spool, the signal is returned to the box via another connector (“Fiber Far End”). The system has been tested at the NRAO with up to 10 km of fiber using an MPB model EFL-R98-T fiber laser with line width (10 kHz typical) and output power (20 mW). The line length correction (OPSIF) system operates by driving the variable delay line so as to keep the total phase delay through it and the external fiber equal to a constant number of cycles of the master laser signal. Details of this will be described in the next section.

At the “far” end of the fiber, a photodetector recovers the beat note signal at f_0 . This signal is mixed with f_1 to obtain 125 MHz, which is then compared in a phase detector with the 125 MHz reference f_2 . The phase detector output voltage is low pass filtered and amplified in an op amp with a single-pole RC time constant of 47 μ sec and a voltage gain of 9; the filtered signal is

available at the front panel for recording. The 125 MHz signal and reference are also brought out on separate connectors so that an external phase detector, such as a vector voltmeter, can be used. The internal phase detector is actually a double balanced mixer, so it provides maximum sensitivity only when its inputs are in quadrature. This can be adjusted using an external variable length coaxial line (“trombone line”), or by slightly varying the 125 MHz reference frequency. During all the measurements reported here, the internal mixer was used as the phase detector and its reference was the PLL IF monitor signal rather than the 125 MHz reference from the synthesizer. When the synthesizer is used directly, the noise on the measured phase includes the PLL residual phase error, which is substantial; most of this is cancelled by using the PLL IF as the reference. -6-Several internal voltages in the test box are available for monitoring at a front panel connector, including:

1. Line length correction phase detector (residual length error), filtered and amplified
2. Coarse fiber stretcher control voltage
3. Fine fiber stretcher control voltage

These signals, along with the filtered phase detector signal, were recorded during the tests using an ALMA AMBSI [47] board and a laptop computer. The ADC range is 0 to 5V with 10b resolution. All of the monitor signals were offset and scaled to fit within this range.

the coarse line stretcher, thus keeping the fine line stretcher near the center of its range. A front panel switch allows the coarse integrator to be reset to zero, setting the line stretcher near the middle of its range for initialization.

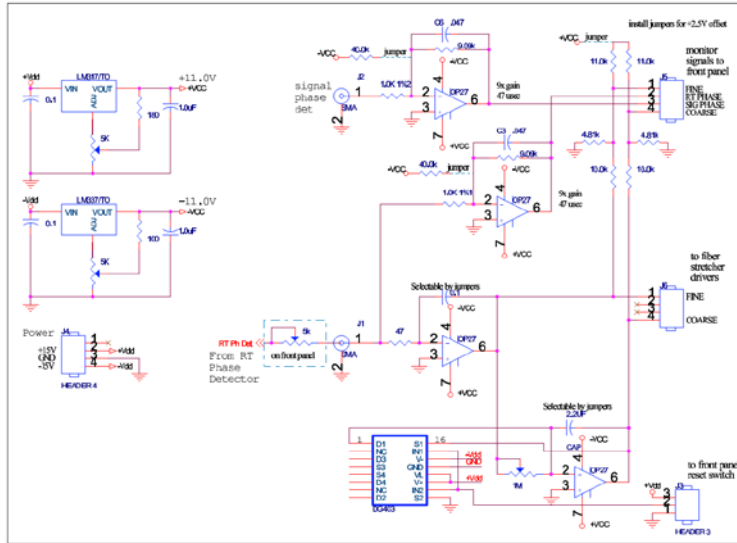


Figure II.3.2.3 Schematic of controller board for correction loop, including filter/amplifiers for monitoring phase detector signals.

II.3.3 Test Results and Analysis

There may have been excessive intensity noise on one or both lasers. Fourier analysis of the time series shows that it is nearly white noise, with no significant features over the Nyquist bandwidth of 0 to 0.5 Hz. Therefore, we think that the rms of the smoothed data or the best fit straight line provide a better upper limit to the residual error of the line correction system. That limit seems to be 60 to 70 fsec. This is far from the ALMA goal of about 6 fsec, but it is the best we could do in this test. The actual error may be much lower. The second plot in Fig. II.3.3.1 shows the residual round-trip optical phase. This signal is dominated by the 1.6 kHz frequency modulation of the master laser (see additional results below). The correction loop's gain was set as large as possible without oscillation, resulting in an integrator time constant of 50 sec. We think that the loop gain

is limited by the speed of the fine line stretcher, which has not yet been fully characterized (although its manufacturer claims a bandwidth >20 kHz). The fiber spool was inside a foam-lined box, and the box cover was opened part way through the test. Nearly one hour of data is shown. The rms signal phase is .0431 radian or 263 fsec; after 50 sec boxcar smoothing, this becomes .0109 radian or 66 fsec.

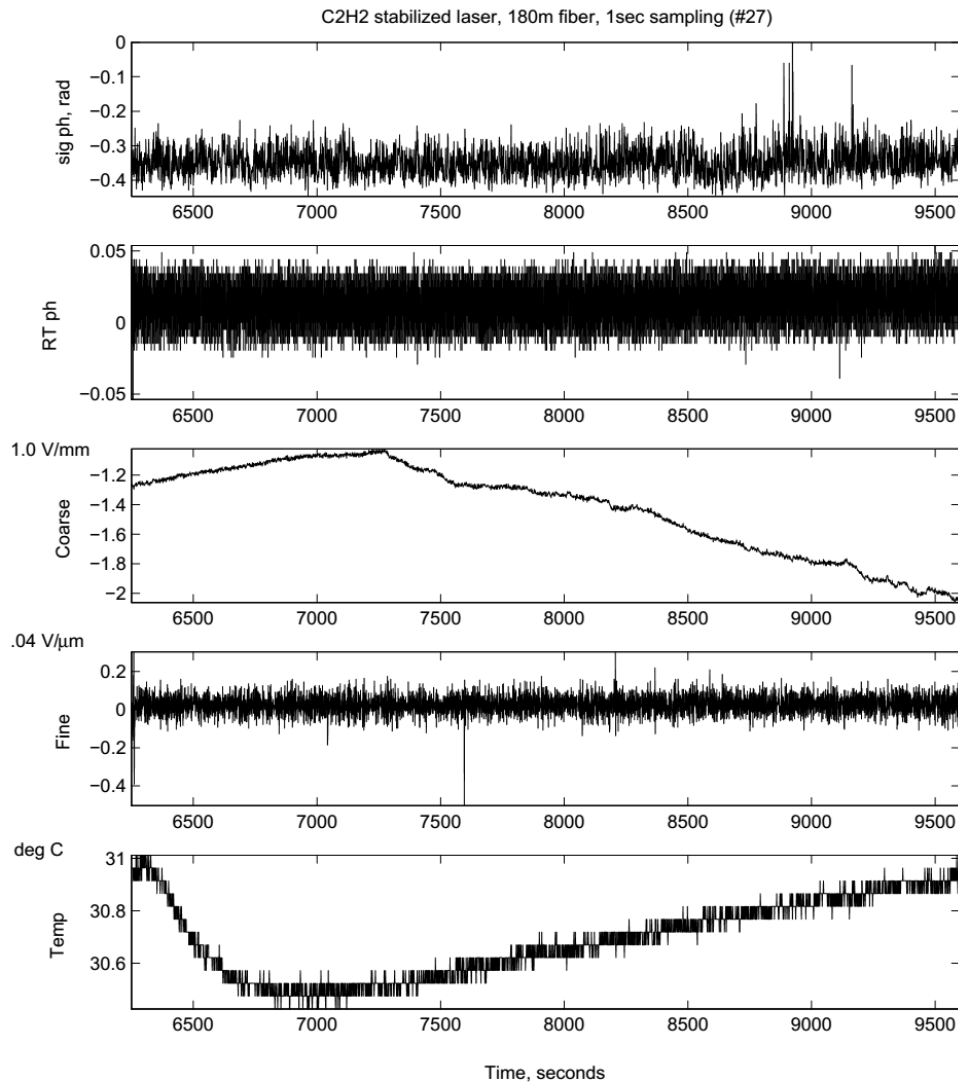


Figure II.3.3.1 Measurements using stabilized master laser with 180m of external fiber. (Top) phase of 26.625 GHz beat note after transmission through the stabilized fiber path. (2nd) is the residual round-trip optical phase error, (3rd) The control voltages to the fiber stretchers. (4th) is the temperature on the main component plate inside the test box. Vertical scales are in volts unless otherwise noted

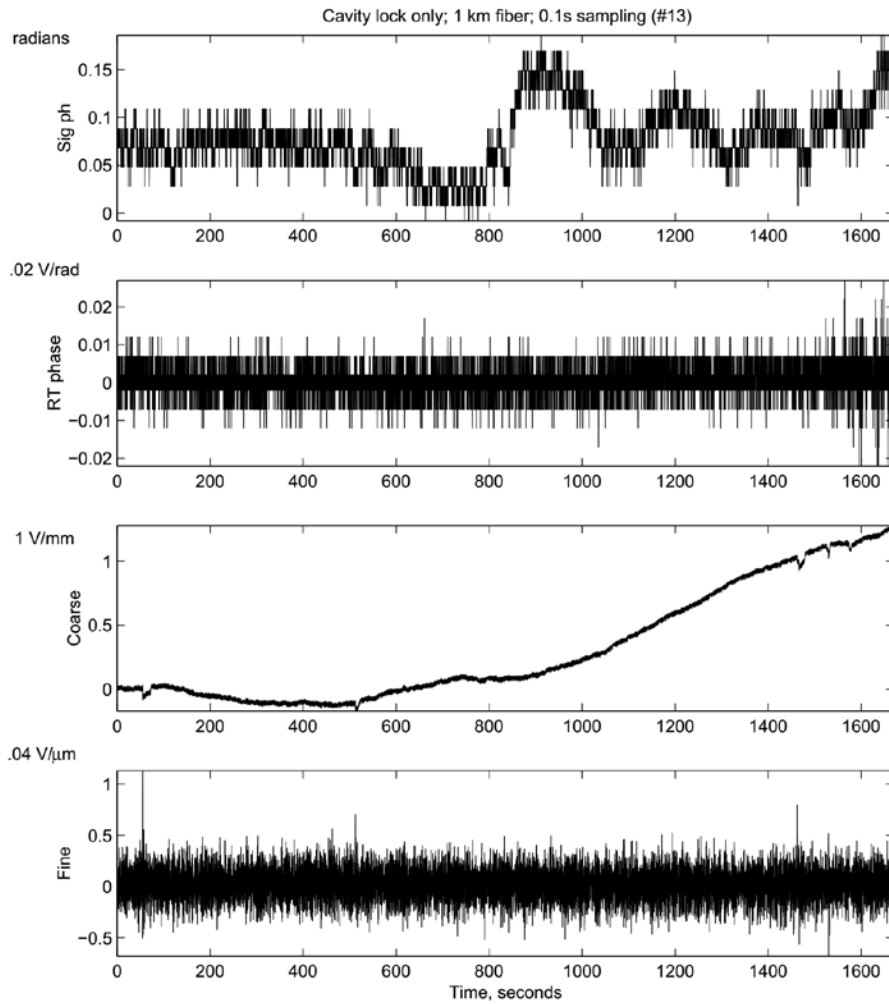
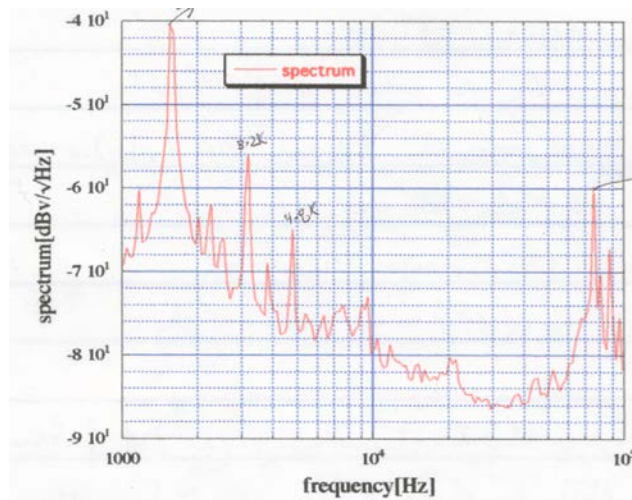


Figure II.3.3.2: Similar to Fig. II.3.3.1 but with 1 km of fiber and with the master laser locked to its optical cavity but not to the acetylene cell.

Figure II.3.3.2 shows measurements similar to those of Fig. II.3.3.1, but with 1 km of fiber and with the master laser's modulation off so that it was not stabilized to the C_2H_2 line. This measurement lasted about 30 minutes, and the laser frequency drifted very little even without the stabilization. Noise in both the signal phase and round trip phase data is dominated by the 5 mV quantization of the ADC. The rms signal noise is about 0.146 radian or 89 fsec at 26 GHz. The peak-to-peak signal phase variation was 0.118 rad or 704 fsec; if all of this is due to laser frequency

drift, as we expect, then the drift was 28.7 MHz peak-peak, and this is reasonable. Meanwhile, the third plot shows that the stretcher length range was 1.45 mm or 6.9 psec, about 10 times as much as the signal delay. Most of this is the intended correction for the change in fiber length, which would be explained by a temperature change of about 0.15 C.

Figure II.3.3.3 shows the spectrum of the residual round-trip phase as observed on a dynamic signal analyzer. The master laser was stabilized and the fiber length was 180m. The signal analyzed was taken directly from the phase detection mixer (not via the filter and amplifier used for the sampled data) and passed through a wide band (approximately 400 kHz) passive low pass filter. The dominant component is from the 1.6 kHz modulation, as expected; harmonics at 3.2 and 4.8 kHz are visible. Another component at 75 kHz is also from phase modulation of the master laser and is due to a low level oscillation in the its cavity locking loop.



FigureII.3.3:3 Spectrum of residual round-trip phase error obtained from dynamic signal analyzer. The UEC laser is used, locked to the C2H2 line and the external fiber length is 180m.

The scaling is 250 mV/radian.

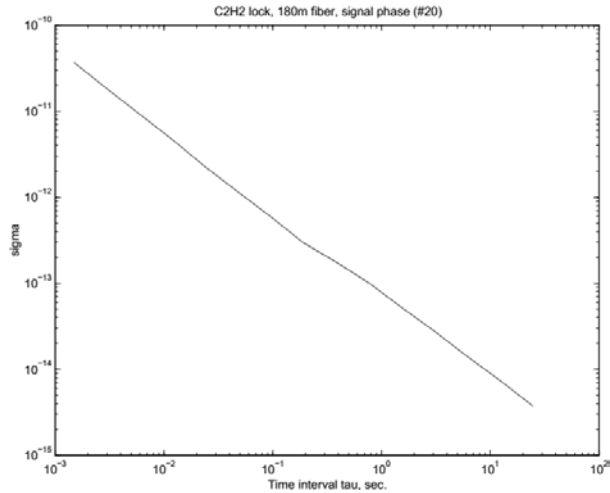


Figure II.3.3.4: Allan standard deviation of the signal phase data from Fig. II.3.4.4 at a frequency of 26.625 GHz.

Figure II.3.3.4 is the 2-sample Allan standard deviation computed from the signal phase data.

Correct operation of the line length correction system has been demonstrated with a wavelength stabilized master laser. The laser's frequency stability on time scales longer than 1 sec is such that it contributes no measurable error in the fiber length. These measurements were limited to a fixed fiber length of 180 m and a signal frequency near 26 GHz, so it was not possible to determine the performance to the precision required for ALMA. Nevertheless, an upper limit of about 70 fsec was placed on the residual delay error in the stabilized fiber.

In the next section we will test the capability of measuring and controlling the phase of a longer fiber span and while the fiber is moving to simulate the antenna motion.

II.4. Optical phase correction for the Photonics LO with a moving structure.

In the previous section we investigated the capability of the first prototype line length correction used with fiber lengths of 180 m and 1 km. In this section we will demonstrate the first attempt in systematic measuring the capability of correcting the optical phase while moving the fiber structure to simulate the ALMA antenna motion during operation. During these measurements we noticed an undesirable and unexpected phase fluctuation which was correlated with the antenna azimuth and elevation position. Through, these measurement we discovered that if the state-of-polarizations (SOPs) of the two lightwaves were different at the receiver end, then any movement of the fiber would cause a phase change.

II.4.1. Optical phase correction measurement at the ATF

The ATF (ALMA Antenna Test Facility) tests were conducted on the US prototype antenna. The test results are fully documented, including detailed schematics of the experimental setup and apparatus. The most significant result was that there was a spurious RF phase fluctuation that appeared to be due to the change in position of the fiber mounted on the antenna. The antenna was at various times moved in azimuth and elevation, and the phase fluctuations were repeatable and position dependent. The test setup that was used for these tests is shown in Fig.II.4.1 which is similar in principle to the one used in proofing the concept of phase correction in Section II.3. A plot of the phase fluctuation versus antenna azimuth position is shown in Fig. II.4.2.

fiber sections.

The effect of the polarization alignment was included in test reports written during that time, but it was not realized that the optical circulators were the largest contributor to the polarization misalignment in comparison to polarization changes due to the fiber movement alone..

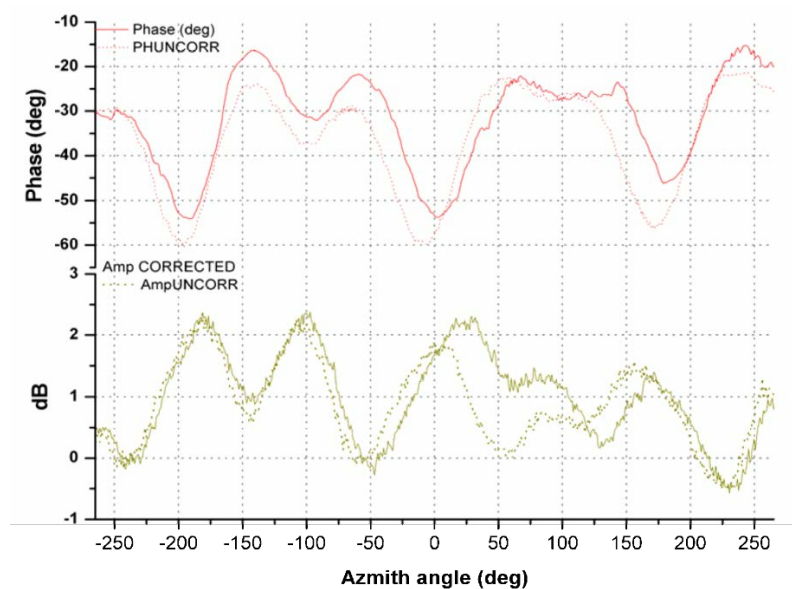


Figure II.4.2 - Phase fluctuation of the 20 GHz beatnote versus azimuth position (red trace– top). The solid line is with the line length correction ON and the dashed line is with the correction OFF. The phase artifact is not affected by the correction, and has some correlation with the variation of the beatnote amplitude (bottom trace).

II.4.1.1 Effect of Optical Circulators

The test setup shown in Fig. II.4.3 was used to measure the State-of-Polarization dispersion (SOPD) of the optical circulator that we had been using in our tests. A tunable laser feeds a polarization rotator and a free-space polarizer, which then goes to the circulator. A polarimeter measures the SOP of the transmitted light. By sweeping the laser wavelength, we can discern the effect of the circulator on the transmitted SOP as a function of wavelength. Also, by rotating the

free-space polarizer, we were able to test this effect as a function of the input polarization.

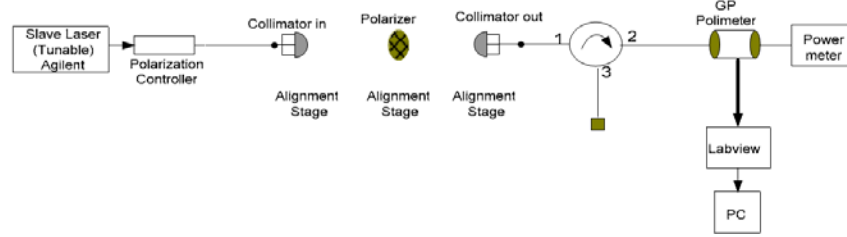


Figure II.4.3: Test setup for measuring State-of-Polarization dispersion of the optical circulator.

The test result is shown in Fig. II.4.4.

The polarimeter measures the Stokes parameters (s_0, s_1, s_2, s_3) – which together completely specify the total power (s_0) and arbitrary general elliptical polarization of the lightwave (s_1, s_2, s_3). For this measurement, the wavelength was swept from 1549.1 to 1550.5 nm. This range exceeds the maximum separation of the two laser comprising the LO reference beatnote (142 GHz is approximately 1.2 nm wavelength separation at 1550 nm). The parameter in equation (8) below which is the root sum of:

$$S_T(\lambda) = \sqrt{[s_1(\lambda_i) - s_1(\lambda_f)]^2 + [s_2(\lambda_i) - s_2(\lambda_f)]^2 + [s_3(\lambda_i) - s_3(\lambda_f)]^2} \quad (8)$$

squares of the difference between the measured Stokes parameters and the initial value of the Stokes parameters. Each of the Stokes parameters can vary from $\{-1..1\}$ so the S_T parameter can range from zero to two. Zero corresponds to a match of the initial polarization, and two corresponds to the point at which the polarization has become completely orthogonal to the initial polarization (maximum SOPD). From the figure it is clearly seen that, depending on the input SOP, the output SOP can become nearly completely orthogonal over a wavelength range of only 0.7 nm, which corresponds to about 88 GHz. Thus, the two-lightwave beatnote could enter the device in perfect polarization alignment, and leave it with completely orthogonal polarizations. For our measurements which were done at 20 GHz the effect was somewhat smaller than this but nevertheless caused very significant polarization misalignment.

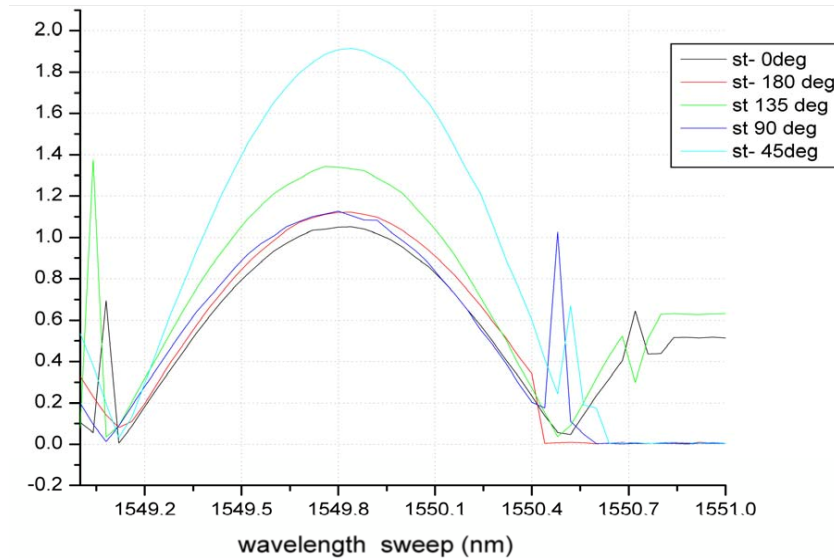


Figure II.4:4 Test Result of State-of-Polarization-Dispersion of Optical Circulator. The vertical axis is S_T (see Eq(1) above). Each trace corresponds to a specific input polarization angle as shown in the key. Peaks and jumps occurring outside the 1549.1-1550.4 range are artifacts of the data acquisition and should be ignored

The reason for the high SOPD of the optical circulator is made clear by examination of the principle behind the operation of a polarization-independent optical circulator. Fig. II.4.5 below shows a sketch from US Patent #4,650,289 “Optical Circulator – Polarization Independent Input Type” Mar 17, 1987. Light entering Port A is split at polarizing beam splitter P1, and in both paths undergoes two 45 degree rotations via a Faraday Rotator (FR) and a birefringent wave plate (OA). The light recombines and goes to port B. Light entering port B is similarly split, but on the return path the Faraday rotation and the birefringent rotation are in opposite directions (Faraday rotation is non-reciprocal). Thus the polarizations are unaffected on the return path and light is transmitted from port B to port C. That is how the optical isolation is achieved, and closer examination is require to see why Sate-of-Polarization Dispersion occurs. Assume that the input

light at port A is linear and splits in equal amounts to the two split paths. At port B the light is recombined. If the two paths have a path difference of a quarter-wave, then the light at port B will be circularly polarized instead of linearly polarized. So the beam path difference causes a polarization change, and this change must clearly be wavelength dependent. The response is different when the input polarization is varied because as the split ratio becomes more unequal, there is less effect due to the beam path difference. In fact, if the light were polarized so that 100% of the light went on one path, the SOPD from this effect should be zero. However, with 1-m fiber pigtails, the light incident on the first beam splitter is likely to be elliptically polarized and it is not surprising therefore that we did not find a polarization angle at which the effect went close to zero. What amount of beam path difference would cause the amount of SOPD that we have measured? If complete orthogonality occurs when the beam path difference changes from one wavelength to another by a half-wave, then the formula is:

$$\Delta L = \frac{1}{2} \left[\frac{\lambda_1 \lambda_2}{\lambda_2 - \lambda_1} \right] \tag{9}$$

We measured orthogonal polarization at difference of 0.7 nm, so that yield $\Delta L = 1.7\text{mm}$, or about 5.6 psec. This is equivalent to the PMD of the device, and represents a very high value. It is necessary to use devices with much lower PMD to eliminate the undesired phase shift effect that we have measured.

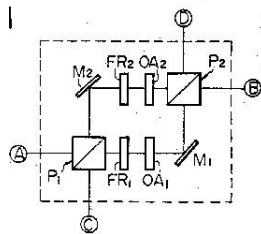


Figure II.4.5 - US Patent #4,650,289 “Optical Circulator – Polarization Independent Input Type”

Mar 17, 1987

II.4.1.2 Measurement of the Phase Fluctuation with Polarizations Aligned and Optical Circulators Removed

The fiber optic circulators were in the system to facilitate the return of the round-trip signal and to diplex the outgoing and returning lightwaves. The large phase fluctuations that we had been observing were present whether the line correction system was operating or not. However, in both cases we used the same test setup incorporating the circulators, simply because it was built into our test apparatus. Therefore, when the effect of the optical circulators was realized, we designed the following test to measure the phase fluctuation without the circulators present. The test incorporates a polarizer at the beginning of the transmission, and light travels as before through a moving fiber section. In the test setup the 20 GHz phase-locked beatnote is detected before and after transmission, then down-converted and phase compared in a vector voltmeter, see Fig. II.4.6. The polarizer guarantees alignment of the two lightwaves going into the moving section of fiber.

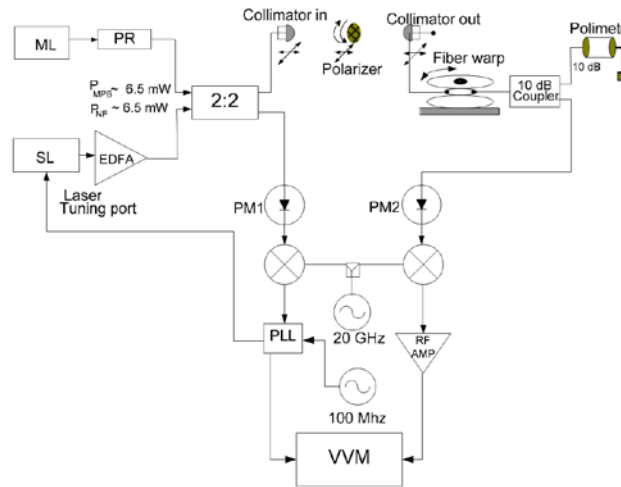


Figure II.4.6 - Test setup for measurement of phase fluctuation due to fiber movement, using two lightwaves with polarization alignment enforced by use of a free-space polarizer. There are no circulators in the receiving system.

The result of this test is shown in Fig.II.4.7. The test shows the phase before, during, and after the movement of the fiber drum through a 300 degree rotation. The movement is then repeated in the reverse direction. The phase fluctuation is now very small, in fact it is difficult to say if there is any fluctuation at all. The RMS phase fluctuation of about 0.4 deg (16 microns or 80 fsec) that is systematic obscures any smaller effects. On the other hand, there is clearly a polarization change that is associated with the movement of the wrap. This test explains the large phase variations at the ATF with the circulator in line. As the fiber was moving it induced large SOPC for both lightwaves, this SOPC was magnified as seen at the output of the circulator as the signal completed the round trip path resulting in high PMD uncorrectable by the OPSIF.

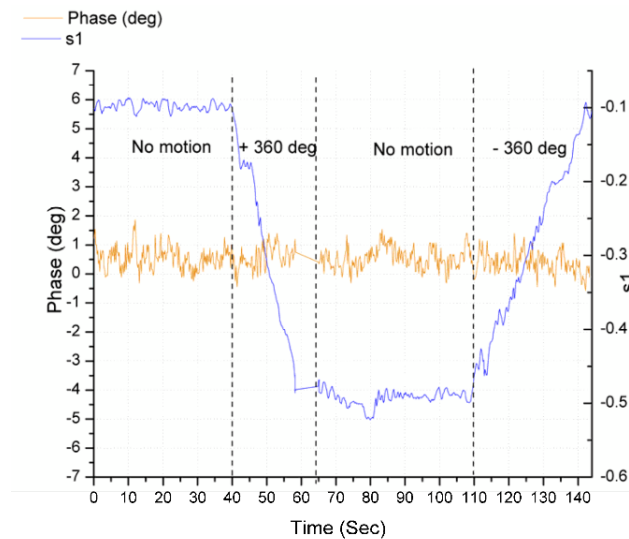


Figure II.4.7: Results of test setup Figure II.4.6 The phase fluctuation resulted by moving the fiber by +360 azimuth rotation and back by -360 deg while recording the change in the polarization due to the fiber move. The Master and slave lasers are fully aligned in this test results.

Ideally, this test would be repeated by adding a fiber spool in series with and before the moving section of fiber. However, without the line correction system in place, the phase changes too quickly due to the thermal drift of the spool, and any change taking place in the phase due to the moving fiber is obscured. However, we expect the long fiber preceding the moving section will cause the two lightwaves polarizations to become misaligned (by introducing SOPD, smaller than the circulator but still potentially significant). This, when coupled with the polarization change induced by the moving section, might be enough to cause a significant phase change.

To determine the level of polarization misalignment that might be expected from the buried fiber, we ran a series of tests on the buried fiber installation at the VLA site [48]. The reference contains a lot of data and experimental description that will not be fully covered here. In principle, however, the measurement was similar to the test of the SOPD of the circulator as shown in Figure II.4.3. The circulator in this case is replaced by length of buried fiber (either 29 km or 58 km -determined by what was available to measure at the site). Unlike the circulator measurement, in this case we did not have a means of orienting the input polarization. The test setup for this experiment is shown in Figure II.4.8. For purposes of comparison, the test was also conducted using a 30 km spool of fiber.

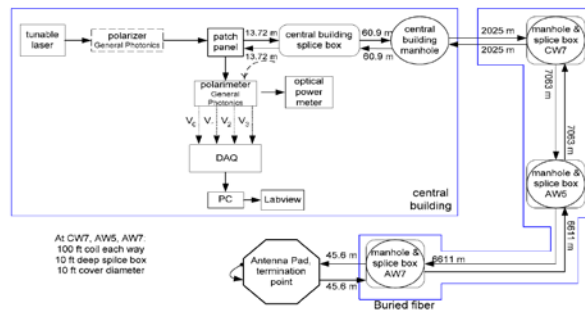


Figure II.4.8: Test setup for measuring the variation of the polarization of the laser light traveling through the buried fiber cable of the EVLA site while scanning the wavelength of a tunable laser source.

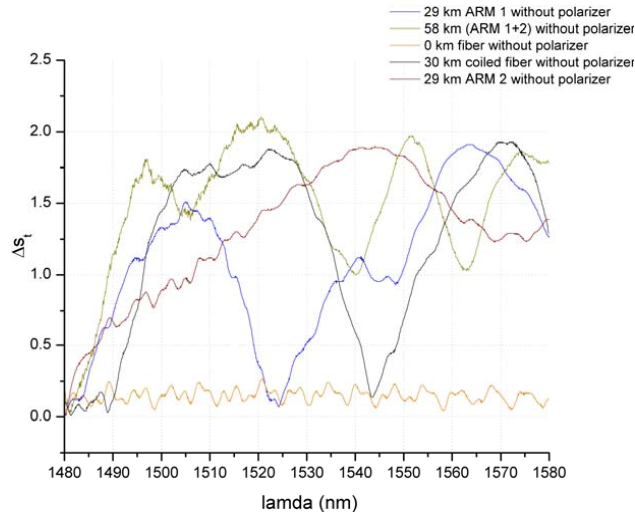


Figure II.4.9: Relative polarization change (from initial value) for various fibers-under-test as wavelength is scanned from 1480 to 1580 nm. The vertical axis is S_T -see Eq (1).

The data in Fig. II.4.9 show that there is a large variation between the various samples, even the two 29 km sections that were in the same fiber cable. The fiber spool variation was not marked greater or smaller than the buried fiber sections of similar length. The bottom curve shows the polarization variation of a length of fiber that was just the sum of the pigtail lengths from the laser to the polarimeter, about 2-m (orange curve). The periodicity of several cycles of variation every 10 nm is partly due to the polarimeter and partly due to the laser source. The wavelength was scanned from 1480 to 1580 nm (100 nm). The SOPD is represented again by the S_T parameter as defined in Eq. (1) The SOPD range is as before from zero to two, with two representing orthogonality between the input and output SOP at 1480 nm. Although the polarization variation can be quite large, it is not so large over the ALMA 1st LO reference maximum frequency of 142 GHz or 1.2 nm in wavelength separation. The maximum possible SOPD between two wavelengths separated by 1.2 nm is what we are interested in. To get this, the data is re-plotted in Fig. II.4.10, but instead of having the S_T parameter normalized to the initial output SOP as before, it is instead normalized to the output SOP of the wavelength that is

1.2 nm preceding it. This is described as follows:

$$S_T(\lambda) = \sqrt{(s_1(\lambda) - s_1(\lambda - 1.2nm))^2 + (s_2(\lambda) - s_2(\lambda - 1.2nm))^2 + (s_3(\lambda) - s_3(\lambda - 1.2nm))^2} \quad (3) \quad (10)$$

The maximum value of the S_T parameter is 0.3 for the 29 km sections and about 0.37 for the 58 km measurement. Since the maximum fiber length for ALMA is about 18 km, it is reasonable to assume that the ALMA SOPD will be no greater than 0.3.

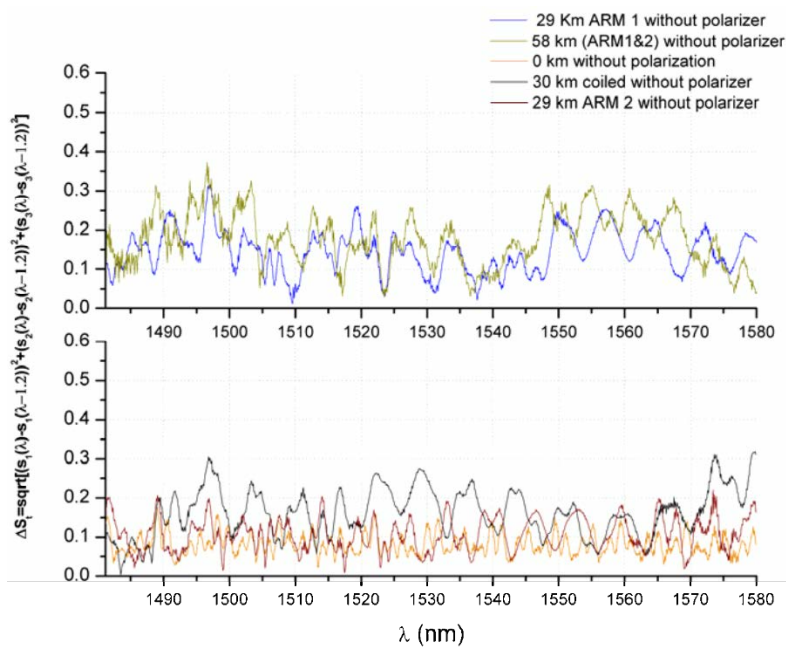


Figure II.4.10 The 1.2nm-variation in S_T (as described by Eq3). The S_T parameter is normalized to the output SOP of the wavelength that is 1.2 nm preceding it

CHAPTER III. OPSiF Performance

As shown in Figure III.1, the two lightwaves are phase-locked at the first 2x2 fiber coupler, by means of a “Near-End” photomixer generating the 20 GHz beat note. This beat note is offset locked by two RF references at 19.9 GHz and 100 MHz. An Optical Amplifier was used just after the Master Laser to provide a decent signal-to-noise for the measurement, but it also will contribute uncorrected phase drift to the measurement. The magnitude of this phase drift has not been studied but for ALMA a special low-phase drift optical amplifier will be used. After the optical amplifier, there is a polarization rotator (PC) used for aligning the polarization of the master laser to the slave laser. This test used a cascade of two commercially available piezo fiber stretchers. The first had a stroke of about 25 microns and bandwidth of 1 kHz, and the second had a stroke of 5 mm and a bandwidth of a few Hz, with a driver voltage range of 20 V. A second PC is used to align the two lasers to the correct orientation at the input of the polarization beam splitter (PBS). The PBS serves the same function as the optical circulators used in our previous work: the outgoing light passes through the assembly and the returning (round-trip) light is reflected to the third port. The output light from port 3 then passes through the fiber stretcher assembly and a 5 km fiber spool and an assembly that simulates simple movements of the fiber. (At the “far-end” there is a 3-dB coupler, so that half of the light goes to the turnaround assembly and half goes to the far-end photomixer. The turnaround assembly consists of the fiber-frequency shifter and a faraday-rotating mirror. The fiber-frequency-shifter contains an acousto-optic cell, and the light receives twice the frequency shift in this type of reciprocal arrangement [49]. The far-end photomixer phase is measured against the near-end phase by means of an offset mixer and a vector voltmeter, as in the earlier measurements shown in Figure III.1. All of the RF references are locked to the same 10 MHz instrument reference. The dotted box around the optical amplifier (OA) in the setup indicates that we have done some of the measurement with an optical amplifier at the “far end.” The need for an

optical amplifier at the far end is likely in the ALMA so that the optical power budget can be met. The main issue that we need to examine is how much phase drift an optical amplifier adds to the overall phase variation since the OA is located outside the optical phase correction path.

III.2 Phase correction with different length spools of fiber

A baseline test was first conducted in which a 1-m length of fiber was used instead of the spool of fiber and the section of bended fiber. The test was run for 1-hr while the correction is on and 27min while the correction is off. In this test we wanted to get the maximum resolution in phase drift that the test setup could provide the calculated RMS phase drift was 0.123 deg at 20 which corresponds to 17.33 fs. The following figures represent the test performed for different fiber lengths with their calculated perspective Allan Variance Structure average with the phase correction OFF and ON to show the capability of performance of the new OPSIF design, without introducing the fiber motion.

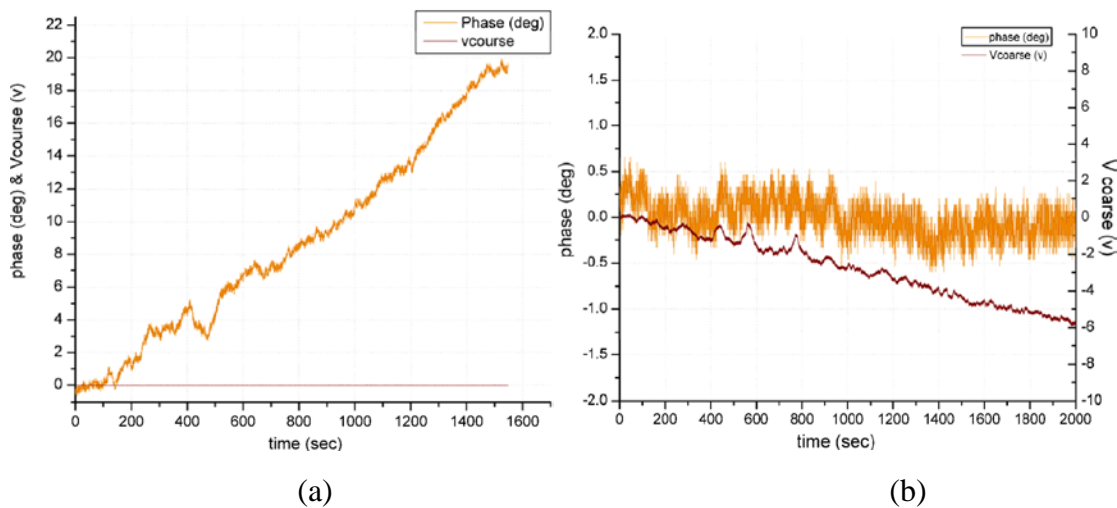
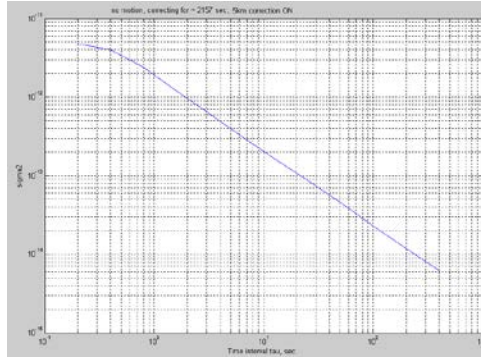
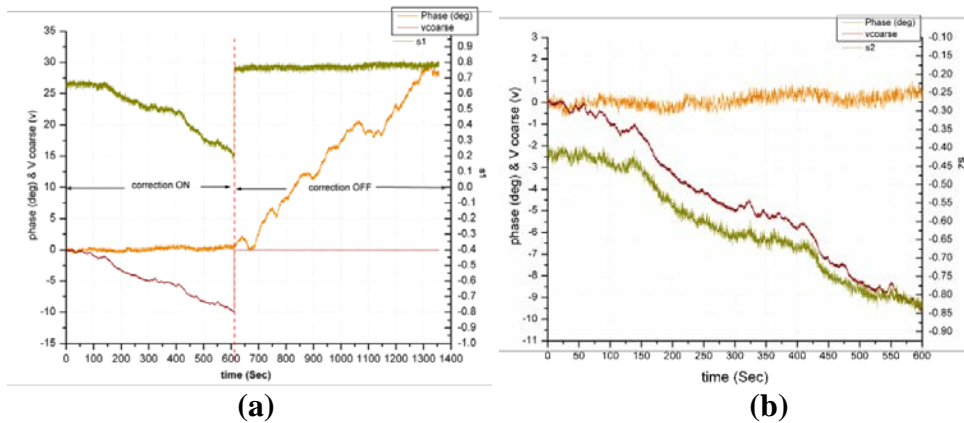


Figure III.2.1: Optical phase stabilization of 5 km of fiber at 20 GHz with
 (a). the correction System OFF
 (b) the correction System ON
 (c) The Allan Standard Deviation for the phase measurement in (b).



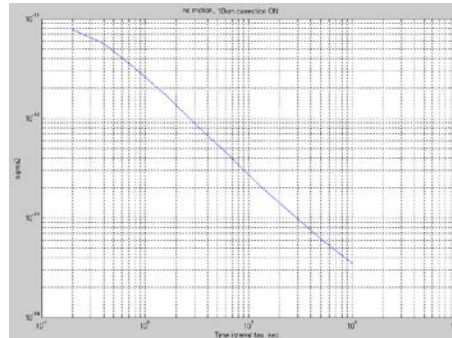
(c)

Figure. III.2.1 (a) clearly shows the phase drift in the 20 GHz phase due to the fiber length change mainly due to temperature effect on the 5 km of fiber. The slope is ~ 0.77 deg phase/sec which equates with phase change of 0.032mm/sec. Assuming a Coefficient of Thermal Expansion of 10^{-5} for the fiber, this implies an average temperature change of 0.2 deg/min during the measurement. In Figure III.2.1 (b), the phase of the 20GHz was measured for 2000 sec while the correction is ON, The residual RMS phase in this case is 0.241 degrees (33.4fs). The peak to peak phase drift for the 2000 sec time was ~ 1.4 deg which corresponds to 194 fs. The coarse voltage changed by ~ 6.6 volts which is equivalent to 1.009~ 1 mm of fiber stretch.



(a)

(b)



(c)

Figure III.2.2 (a): 10 km of fiber at 20 GHz with the correction ON and OFF

(b): zoomed version of 10 km of fiber at 20 GHz with the correction ON.

(c) The measurement of the Allan variance of the phase

In Figure III.2.2 the test repeated for a 10 km length of fiber, with the correction on for 600 sec and OFF for 700sec. The green line represents one of the polarization Stoke's parameters (s_2) which shows the polarization change in the fiber. A zoomed view of the part with the correction "on" is illustrated in Figure III.2.2 (b). The first significant observation the plots of Figure III.2.2. is the obvious correlation between the polarization and the coarse correction voltage. This occurs because the fiber stretcher causes not only a length change in the fiber, but also a birefringence change that in turn causes a polarization change. This is undesirable given the results of our previous measurements; clearly we want to minimize any time variable polarization changes. It may be possible to use a fiber maintaining coarse fiber stretcher to eliminate this effect. For the 10 km section, the rms phase change with the correction on was 0.3 degrees (41.6 fs) and the peak-to-peak total drift over 600 seconds was 1.7 degrees (236 fs).

III.3 Phase correction with the Fiber Movement:

a. Controlled bending with variable radius of curvature.

Bending was applied to the fiber in a very controlled manner and reasonably slow and controlled speed. Ideally we would like to see the system correcting for all possible fiber movements including a sudden or rapid motion. But we have learned from testing that the system is very sensitive to sudden and very fast motion of any part of the fiber. For this reason, it will be necessary to consider and evaluate different fiber movements and different fiber wrap configurations. Three test results are shown for the case of the fiber bending:

1. 5 km with the correction off
2. 5 km with the correction on
3. 10 km with the correction on and off in sequence

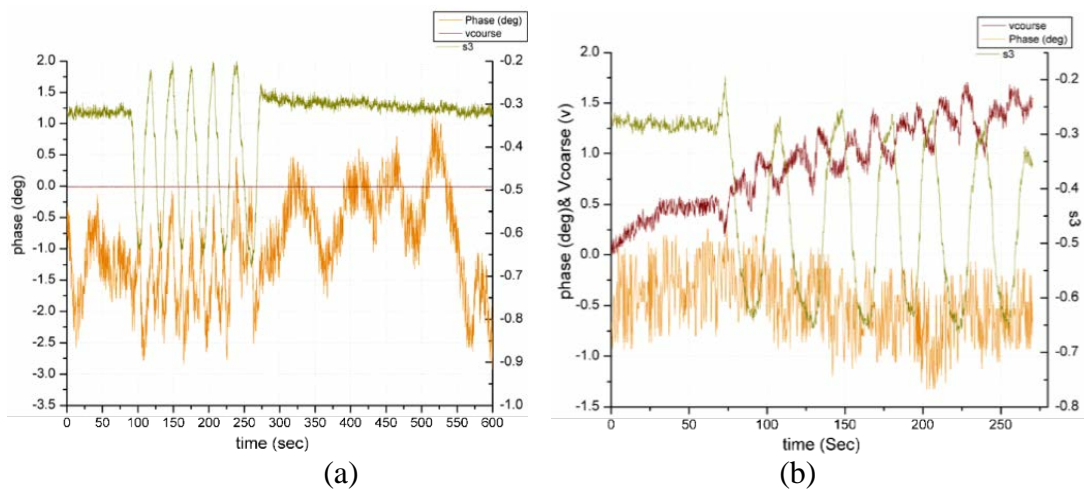


Figure III.3.1: (a) 5 km correction is OFF while bending the fiber (b) 5 km correction is ON while bending the fiber

Figure III.3.1 (a) shows the phase change while bending 20 meter of fiber after 5 km of distance, with the correction is off. It is very clear to see the impact of bending the fiber on the polarization. In this case only one of the Stoke's parameters (s_3 in this case) was plotted. The steady and repeatable change of $s_3 \sim 0.85$ correlates with the change in the 20 GHz phase of about (average p-p) 1.98 deg peak-to-peak. The fiber bending occurs only from 100 sec to 275 sec. From 275 sec to 600 the phase was fluctuating due to the 5 km of fiber. Figure III.3.1 (b) the correction is ON all the time. From 0 to 75 sec the fiber is not moving (or bent). From 75 to 270 the fiber is bent multiple times, the bend radius was changing from 2.5 inch to 26 inch. The brown line represents the change in the control voltage that is driving the slow stretcher. The phase change due to the fiber motion is clearly suppressed in this measurement. This is obviously a large improvement over Figure II.4.1. The important information - how much residual phase change is caused by the bending? – is difficult to determine due to the fact that it is lower than the rms residual phase noise level. Further analysis or measurement might yield a functional relation between the bending and the phase change after correction.

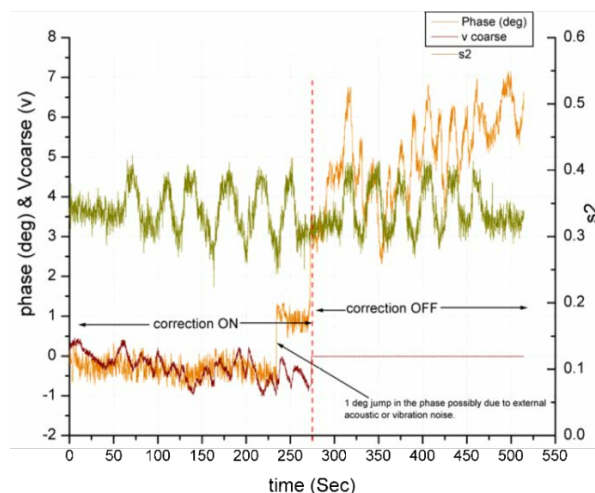


Figure III.3.2 10 km length of fiber with controlled bending correction is on and undergoes cyclical bending from 0 to 275 sec., then the correction is turned off from 275 sec to 525sec. The bend radius was changing from 2.5 inch to 26 inches.

Figure III.3.2 shows that in case of 10 km of fiber, the maximum phase variation while bending the fiber with the phase correction ON was less than 0.7 deg (97 fs). However while applying the bending to the fiber while the correction is off (from 275 sec to 525 sec) the 20 GHz phase changes by 4.5 deg.

b. Fiber Twisting

Figure III.3.3 shows the phase variations while twisting $\frac{1}{2}$ inch of fiber after 5 km length of fiber, the maximum phase variation while twisting the fiber with the phase correction is OFF was ~ 7.1 deg (from 0 to 130 sec) and 6 deg (from 350 to 500sec) . However while applying the twisting to the fiber while the correction is ON (from 130 to 325 sec) the 20 GHz phase changes by 0.9 deg.

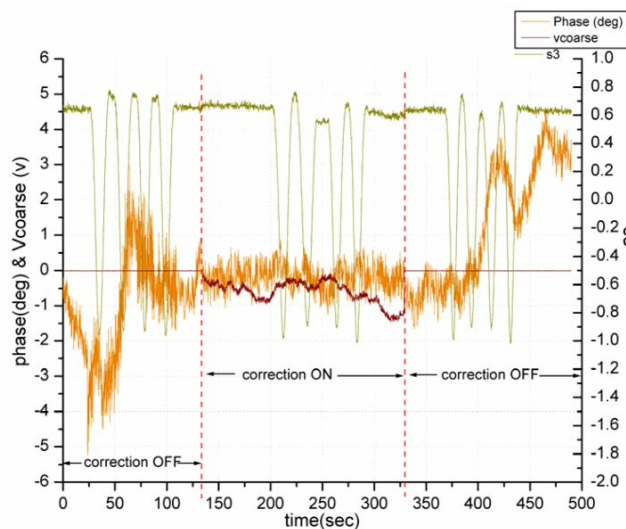


Figure III.3.4: 5 Km with twisting $\frac{1}{2}$ inch of fiber from 0 to + 360 deg and then back from

+360 to 0 deg . The correction is OFF from 0 to 130 sec, then the correction is ON

From 125 sec to 327sec, and finally correction is OFF from 327sec to 490 sec.

III.4. Phase drift due to the Optical Amplifier

Figure III.4.1 represents the phase change of the 20 GHz beatnote for 5 km fiber distance while inserting an OA before the photomixer at the far-end.

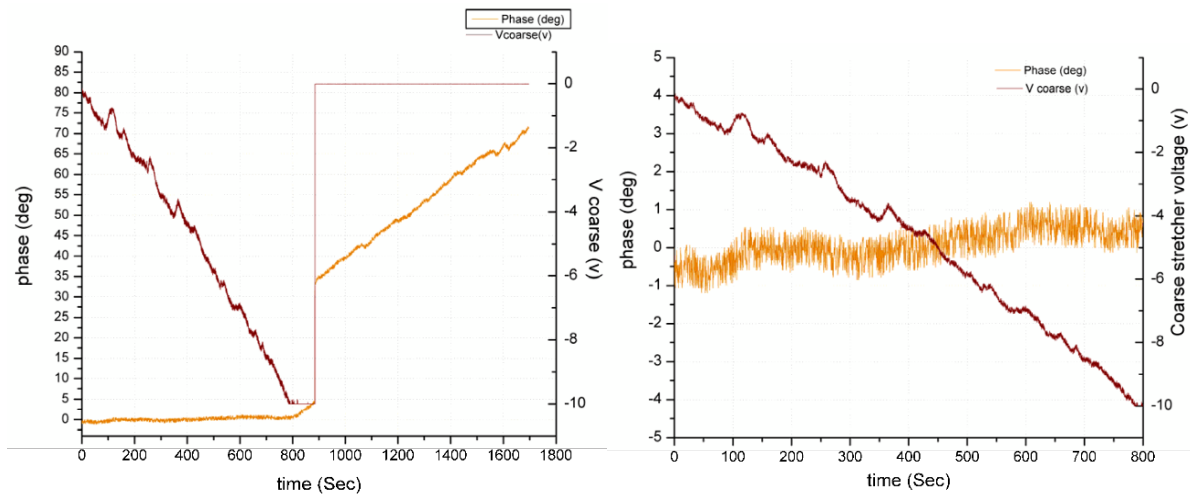


Figure III.4.1: (a) Test of the phase incurred on 5 km of fiber at 20 GHz with the correction system ON (from 0 sec to 800 sec) and OFF from (800 sec to 1700 sec) with an OA located just before the far-end photomixer (refer to Figure III.1). No movement of the fiber has been applied. (b) Zoomed version of the correction ON part of (a).

From Figure III.4.1 (b) above, the maximum phase change while the correction is on was ~ 2.3 deg which corresponds to 319.4 fs. By comparing the results to Figure III.4.1 (without an OA at the far-end), the RMS phase change is 0.455 deg (63.2 fs), yet the maximum phase change was 1.4 deg (194 fs) for 2000 sec. The OA at the far end (located outside the zone of the fiber correction loop)

seems to have added ~ 0.9 deg of phase drift (125 fs) to the overall 20 GHz beatnote phase at the far end. The OA that was used in this test was from JDS model# ONA 2017 , it was turned on for several hours before this particular measurement was taken. We have noticed that the OA adds much more phase drift at the 1st 1 hr of operation due to warm up and stabilization. Several other measurements (not included in this section) were performed on other OAs that had shown larger drift in the phase of the far-end 20 GHz beatnote.

III.5. phase correction 2 ALMA antenna System implementation

In this section we demonstrate the ability of generating and distributing high frequency photonic based microwave reference in a single mode fiber of 14 km to 2 of the ALMA radio telescopes. 81GHz photonic LO reference is generated and transmitted over the single mode fiber to the receivers of the 2 antennas. The section will also present the method used to measure and dynamically stabilize the phase of the microwave photonics reference transmitted to 2 antennas while simulating antenna motion. The photonic phase correction system will null the unwanted phase in the microwave reference resulted from the motion of the telescope, maintaining coherence between the 2 antennas.

As indicated in Chapter I the ALMA instrument will consist of fifty 12 meter diameter antennas, separated by a maximum distance of 15 km, and will be installed operating at an altitude of 17000 ft in the Atacama desert in northern Chile [50]. The instrument will allow a break through research into the physics of the cold universe, regions that are optically dark but shine brightly in the millimeter portion of the electromagnetic spectrum. Providing astronomers a new window on celestial origins, ALMA will probe the first stars and galaxies, and directly image the formation of

planets [51]. In order to achieve this capability, the instrument phase stability and coherence specifications are quite stringent. The array will be operating between 31-950 GHz using cryogenically cooled heterodyne receivers. The millimeter wave receivers have YIG Local Oscillators (LO), ranging between (12-25 GHz) which are multiplied up and amplified to reach the desired reference sky frequency. For those bands that require an LO, the LOs must be phase stable and coherent among all the antennas. This is accomplished by locking the phase of the YIG LOs using Phase Locked Loop (PLL) to a common low phase noise microwave reference (first LO reference) [52]. Due to the large frequency operating range of the ALMA instrument, the first LO reference must be able to provide reference signal that covers all the receiving bands. Table III.4.1 below covers some of the important first LO reference specifications.

<i>Requirements</i>	<i>Value</i>	<i>Notes</i>
Frequency Range	27-142 GHz	Design Choice
Switching Speed	<100 ms	
Phase Noise	<38 fs	1 Hz-10 MHz
Phase Drift	<13fs	20s to 1000 s
Power Level	>50 nW	

Table III.5.1: A subset of ALMA photonic LO reference specification

The selected design for the first LO reference generation and distribution implements photonic based systems to generate, distribute and convert the photonic reference into a microwave reference at the receiver in each antenna. The design for the prototype hardware provides excellent performance capability, yet there are technical challenges. The next section provides a description of the ALMA photonic system and its principle of operation. In later subsections of this section will cover past and recent phase measurements and stabilization experiments for the

first LO reference and characterize the phase stability under certain ALMA operational modes.

III.5.1 PHOTONIC SYSTEM DESIGN DESCRIPTION

The ALMA photonic first LO reference system can be broken down based on functionality into 4 parts as shown in Figure III.5.1. The first three parts are mounted in the central LO rack located in the control building in a central location within the ALMA array. The last part is located in the receiver cabin of each antenna. The first part consists of the Master Laser (ML), Slave Laser (SL), Laser Synthesizer (LS) and a Central Variable Reference (CVR). It is responsible for generating a highly stable photonic LO microwave reference. The photonic LO reference is generated by combining the optical signal output of both lasers operating at 1550 nm and creating a millimeter beat frequency that is detectable by a High Frequency Photodetector (HFPD). The LS generates the photonic reference beat note signal at frequency ($f_{LO-Ref} = f_{ML} - f_{SL}$) which is tunable depending on what is the desired astronomical observation frequency needed at the receiver. The CVR is a low-noise microwave reference ($f_r = 8-12\text{ GHz}$) such that $f_{LO-Ref} = f_{ML} - f_{SL} = n f_r + 125\text{ MHz}$. The CVR is externally locked using a 5 MHz highly stable crystal RF reference that is locked to a maser source. The 5 MHz crystal reference is also used to generate the lower frequency LO signals needed to lock other hardware at the antenna. The low frequency LO signals (25 MHz, 2 GHz and 48 ms) are amplitude modulated using a laser light at 1532 nm, and transmitted to the antenna via the same optical fiber running between the central building and the antenna. The second part is the photonic distribution system that consists of 2 pieces. The first piece creates copies of the LS signal that are amplified and distributed to each antenna, and the second creates copies of the ML signal and distribute them through the system for phase stabilization. The optical signals are launched into SMF cable that is buried 1 m under the ground, and terminates at each antenna's receiving cabin. The signal runs through each antenna pedestal and steel construction passing through both azimuth and elevation fiber wraps. In this

configuration, the phase of the photonic 1550 nm LO signal will change differently at each antenna due to two main effects. The first effect is the external environmental effect that includes vibration and temperature fluctuations which induce unequal variation in the fiber length at each antenna, and the second is the antenna motion in both azimuth and elevation angles while making a dynamic astronomical observation. The phase measurement and stabilization of the first LO is accomplished using the third part which is Optical Phase Stabilization in Fiver (OPSIF). The OPSIF is designed to measure the round-trip phase of the transmitted signals to each antenna interferometrically, and dynamically stabilize the phase of the first LO signal at the receiver. Taking advantage of the highly phase stable ML and its narrow line-width, an optical fringe of the roundtrip phase is obtained and controlled. The fourth part is the LO Photonic Receiver which contains identical 1.5 μm HFPD to the one in the LS acting like a mixer. The HFPD has a limited range of ~ 150 GHz [53, 54]. The HFPD will recover the photonic LO reference beatnote $f_{\text{LO-Ref}}$ which is fed directly to the ALMA receiver to lock the YIG LOs. The fibers are kept insulated, and their lengths are equally minimized since they are located outside the phase correction region of the OPSIF. Any perturbation in the particular fibers will induce phase drift in the first LO photonic reference feeding the receivers that is not detected and corrected by the OPSIFs in the central building. The $f_{\text{LO-Ref}}$ is set at 81 GHz in the experiments described in this section.

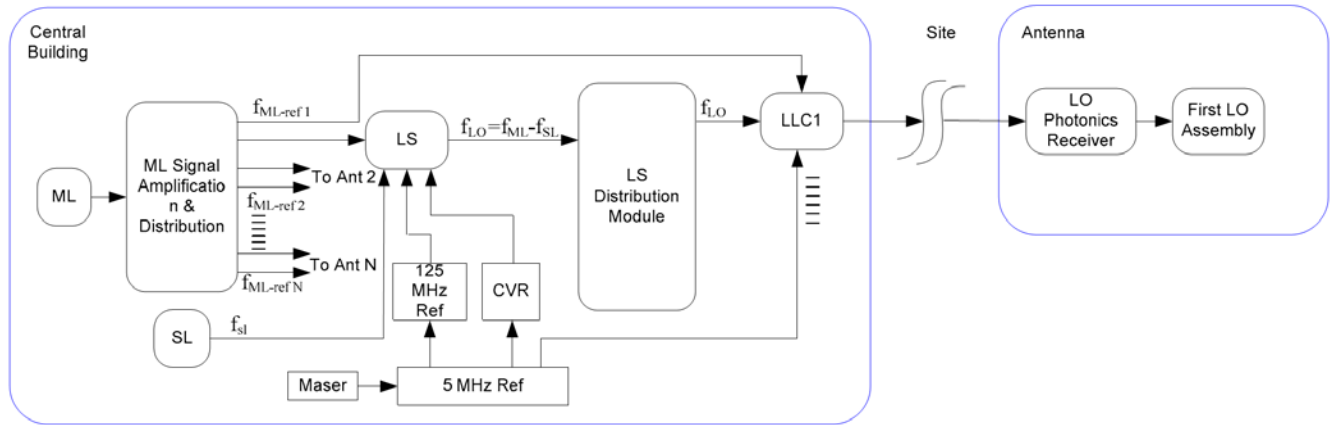


Figure III.5.1 Simplified ALMA Photonic LO System Diagram

III.5.2. The Laser Synthesizer

The basic configuration is shown in the block diagram in Figure III.5.2.1 The ML used is one of two specially built ALMA prototype units. This source is obtained by frequency-locking a 1556-nm narrow linewidth DFB fiber laser to a two photon transition in rubidium 85 at 778 nm after second harmonic generation in a non-linear waveguide crystal. The prototype yielded an absolute wavelength of 1556.210 843 nm, a stability of 2×10^{-12} at $\tau = 1$ s, a linewidth of 2 kHz over ~ 1 ms, a coherence of 40% at 50 km over 1 ms, and a RIN below -145 dBc/Hz for $f > 10$ MHz [55]. The SL is non-stabilized narrow linewidth DFB-FL. The output frequency of the SL is tuned using an internal PZT. The ML and SL are combined using a Polarization Maintaining Coupler (PMC) and photo-detected using a local HFPD. In order to obtain high optical power, the two light wave's State of Polarizations (SOP) must almost the same. Any small difference in the SOP between the two laser signals could a low output power and a poor locked resulting beatnote signal. A manual polarization rotator is used in the path of the ML signal to align the ML light to the SL light which is driven by a PM fiber. The generated f_{LO}-Ref beatnote is phase compared with nfr-125 MHz using a harmonic mixer (HM). The resulting phase error is used to drive a correction loop circuit.

In this case, the correction is made by driving a Fiber Frequency Shifter (FFS) which is an acousto-optic modulator Bragg cell. The FFS is driven by a 45-77 MHz Voltage Controlled Oscillator (VCO) which provides the higher bandwidth part correction to the phase error. Additionally, the lower bandwidth phase error correction part is implemented by altering the frequency of the SL using the internal PZT to the SL. The LS configuration has many challenges such as the State of Polarization Change (SOPC) of the resulting beat note that must be minimized since the resulting SOPC can be converted into phase [56] which could reduce the sensitivity of long term phase stabilization measurement. The resulting f_{LO-Ref} phase noise result is compared with the scaled reference from a commercially available microwave synthesizer is shown in Figure III.5.2.2 Ref [57].

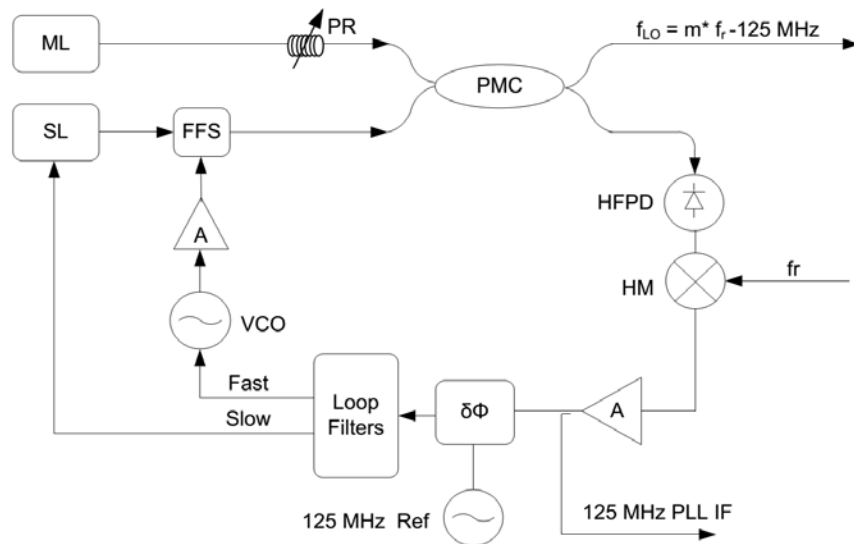


Figure III.5.2.1 The schematic of the ALMA prototype Laser Synthesizer (LS)

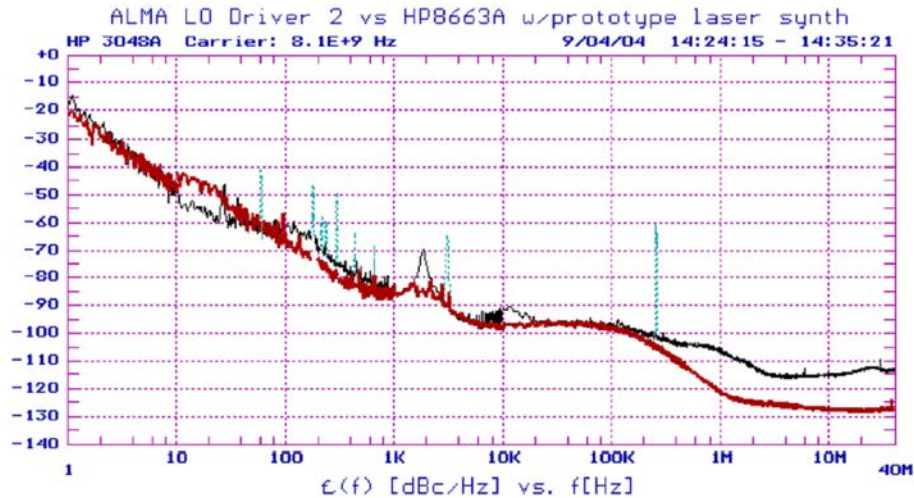


Figure III.5.2.2 The phase noise results comparing the LS first photonic LO output at 81 GHz (black) and the scaled microwave reference to 81 GHz (red), phase noise (1KHz to 10 MHz) = 0.017 rad= 35 fs.

III.5.4 The Optical Phase Stabilizer

The OPSIF is a very crucial device used to maintain phase stability of the first LO reference between the central building and each antenna. Since the length of the optical fiber will change due to temperature, vibration and due the motion of the antenna in the azimuth and elevation, the OPSIF ensure a constant length of fiber in maintained between the two ends, leading to a constant phase of the transmitted first LO reference. The OPSIF uses the length of the fiber as an optical interferometer to measure the phase of the roundtrip signal The combination of the master and slave laser signals are sent to every antenna, then reflected back using a faraday mirror and shifted twice by 25 MHz via acoustic optical modulator and returned back to the central building. The faraday mirror reflects the 2 signals in an orthogonal polarization with reference to the incident beam. This technique isolates the transmitted beam from the reflected beam back to the source

[58]. The reflected and frequency shifted roundtrip signal from the antenna exits the third port from the PBS as shown in Figure III.5.4.1. The resulting $f_{\text{ML}}+50$ MHz signal is mixed with a Master Laser Reference $f_{\text{ML-Ref}}$ and fed to the low frequency photomixer to generate a beatnote of 50 MHz. The phase of the resulting 50 MHz beatnote changes directly with any possible disturbance occurring in the optical fiber between the central building and the antenna. A change in the fiber length of $1.56 \mu\text{m}$ will cause a phase shift in the 50 MHz beatnote of 2π . The output of the phase detector is amplified and fed to a frequency divider in order to increase the resolution of the phase correction system. The resulting 5 MHz phase is compared with the 5 MHz reference via a digital phase detector. The output error signal is then fed to a loop filter that will drive the fiber stretchers. Additionally, the circuit contains a frequency counter that converts the output of the digital phase detector to the number of optical fringes in order to correlate the number of optical fringes to the desired measured phase. The fiber stretchers use length of single mode fiber attached to a piezo transducer such that an applied voltage to the transducer will alter the tension applied to the fiber and eventually change the fiber length. In the production version 2 fiber stretchers are used, one with a longer range and lower correction bandwidth, and the second is with smaller range and higher correction bandwidth. The correction bandwidth is the reciprocal of the speed at which the transducer can apply change to the fiber stretching. The slow stretcher has a range of few millimeters up to 10 Hz of bandwidth, while the fast stretcher has a bandwidth of few hundreds of hertz and a range of 3 mm. The experiments that were run here used only the fast stretcher. An applied control voltage of 1 Volt causes the fast stretcher to stretch by 0.3191 mm which corresponds to change in the phase of 81 GHz photonics LO reference of 52° at the antenna. When using the OPSIF for the final ALMA system, the error signal generated from the phase detector is fed to two control loop circuits with different correction bandwidth settings to drive each stretcher.

When the two control loops are closed, the cascaded configuration of the two stretchers ensures that the slow stretcher keeps the fast stretcher below the limits of saturation, while the error signal is kept to zero. During the setup of experiments studied in this section, the slow stretcher was kept outside the loop and only the fast stretcher was engaged in the correction. The fast stretcher dynamic range was to 1.5 mm. Due to the limited dynamic range, the stretcher was operating between the middle set point and the lower saturation limit causing the stretcher to reset every 2 volts of change in the control voltage. This corresponds to 0.638 mm of length in the fiber stretcher. The OPSIF monitor and control parameters were implemented using a custom Labview code. The code is written such that it will bring the stretcher control voltage to the middle point of the dynamic range very time the stretcher reaches its saturation limit.

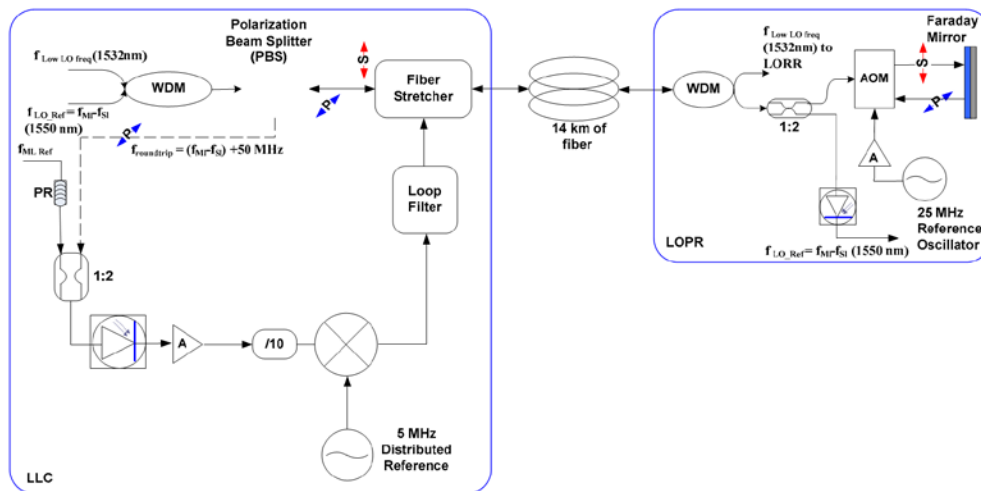


Figure III.5.4.1 A schematic of the ALMA prototype Optical Phase Stabilization in Fiber(OPSIF) and the photonic components in the LOPR

III.5.6 EXPERIMENTAL SETUP

The setup in Figure III.5.6.1 shows the test configuration used to test the relative phase stability of

the Photonic LO Reference. The diagram is broken into 2 parts: The upper part of the diagram is the Photonic LO system, which is generally represented in Figure III.5.5.1. Starting with the ML, the ML produces 3.3 dBm of optical power at a wavelength of 1556.2 nm. It acts as a main frequency stable photonic reference to the entire ALMA system. The output of the ML is fed as an input via a short SMF acoustically insulated fiber cable to the first Erbium Doped Fiber Amplifier (EDFA1). The output of EDFA1 is directly fed into 1:4 Photonic Reference Distribution (PRD) module used to create four copies of ML_{ref} signal. The first two copies are used as a reference signal for both OPSIFs in the path of the two antennas. The third output is fed as the main input to the LS. Since the polarization alignment between the ML and SL inputs is essential to create a higher microwave power beatnote for the desired Photonic LO Reference State of Polarization (SOP), PRs are used to manually adjust the SOP of the desired input light with the SL light that it is combined with. For example, PR1 in Figure III.5.4.2 is used to align the SOP of ML with the fixed SOP of the slave laser while they are combined and phase locked in the LS. The PRs are used across the entire experimental setup wherever is needed.

The LS serves 3 functions: First is to select the desired difference between f_{ML} and f_{SL} . The first LO reference frequency is $f_{LO-Ref} = f_{ML} - f_{SL}$, and is selected by tuning the PZT of the SL once a command via Labview is sent to the SL via the CAN Bus. Second is to lock the phase of the SL to the very stable ML phase. And third is to maintain the lock of the SL to ML. The output of the LS is fed via an optical attenuator (10dB) into the input of the EDFA#2. EDFA#2 is responsible for amplifying the Photonics LO Reference to 16 dBm, then creating two copies using a SMF optical coupler creating an output power level of 12.5 dBm for each output. Those outputs are then fed as inputs to both OPSIFs via polarization rotators (PR4 and PR5). Each OPSIF output is designated for each antenna analog rack input via the LORR module. Each OPSIF is designed to measure the

round trip phase change in the fiber between the central LO rack and the Analog rack and apply real-time correction by adding/subtracting fiber length using fiber piezo stretchers. In this particular experiment, only the fast stretchers were enabled in the both OPSIFs. The slow stretchers were disabled. The two optical signals centered at 1532nm that carries the low frequency LO signals, and the 1550 nm Photonic LO Reference are passed through the OPSIFs via a WDM device that mixes the two signals in one fiber that ends in the LORR-FO module. At the LORR-FO the two signals are split using another WDM device placed in an opposite configuration. Normally during ALMA operation the LORRs are placed in the analog racks that are installed in each antenna. However this experiment was performed in the lab with the analog racks and central LO rack are side by side. Such experiment will be impossible to perform in a real ALMA system. Since we are doing a relative phase measurement between the two arms, one arm has only ~10m of fiber length, and the second arm has 14 km spool of fiber to simulate the length of furthest antenna location from the Central LO rack. In order to obtain the best performance of the system, the spool of 14 km of single mode fiber was placed in a Styrofoam box to provide better temperature insulation from the rapidly changing lab ambient temperature. The temperature inside the box and in various places around the experiment was acquired using an Agilent DAQ card and a Labview gui was used to collect data from the DAQ. The maximum change in temperature reading inside the fiber box was 0.25 °C in the course of the first hour. The Local Oscillator Reference Receiver (LORR) is a module that received the 1532 nm optical signals and recovers the low frequency references those are: 2 GHz, 25 MHz and 48 ms timing signal. The LORR also performs phase locking for all three signals to local oscillators to ensure phase coherence of those signals between the central building and the antenna. The low frequency LOs were all locked during the experiment.

The LORRs also provide a phase locked 125 MHz reference to the FLOOG (Frequency Local Oscillator Offset Generator) modules to lock their 31.5 MHz internal clocks. And the FLOOGs provide the locked 31.5 MHz signal to both WMA to lock the YIG oscillators used for frequency switching during ALMA observation. The 1550 nm signals split from the 1532 nm in the LORR using another WDM, then is delivered to the WMA photomixers as the first LO reference to lock the WMAs as indicated in Figure 5. In this test analog PLLs were used in the WMAs. The goal of measuring relative phase of the Photonics LO Reference between the two simulated antennas is achieved by providing a common microwave beacon set in this case at 102 GHz to both receivers simulating a single sky source. The latter signal is produced by injecting a synthesizer microwave signal at 17 GHz into a harmonic mixer that produces harmonics.

III.5.7 Fiber Wrap Configuration

The unique in house design for the fiber wrap is suitable for both azimuth and elevation motions at each antenna. Both types of motions require that the fiber entering the wrap (which is 13.5in diameter) is fixed at one end and movable at the other end. The design ensures two important aspects. First that the fiber will exhibit a controlled bending only motion, and second that the bending radius stays constant throughout a complete rotation cycle of 360° turn. Both aspects help to minimize the induced SOPC while the fiber wrap is in motion. The wraps involve the use of cylindrical gears that are responsible for transferring the motion and keeping the bending angle of the fiber constant. The design of the fiber wrap was done in such way that every 1° of rotation in the wrap (θ_{wrap}) corresponds to 0.5° of antenna motion (θ_{ant}). Since one end of the fiber is fixed and the other is movable while the antenna is moving, the two prototype fiber wraps were connected back to back. When manually rotated, the two wraps will turn θ degrees of angle without causing any fiber twisting between the moving and fixed ends. The following result

section explains the test performed with the fiber wrap motion. Figure III.5.7.1 shows a picture of the back to back fiber wrap setup. The 2 wraps were moved manually in $\sim <1$ deg rotation angle per second. The applied rotation to both wraps simulates a wide range of antenna motion in both azimuth and elevation at the same time. It is important to note that the fiber wrap prototypes had an internal mechanical problem that caused the motion of the fiber in the internal cylinders not to be very smooth all the time. The effect is shown in the data and analysis section where the OPSIF correction loop filter and stretchers could not correct for the non-smooth motion of the fiber in the wrap causing large jumps in the phase of the 81GHz signal. The problem has been identified and will be corrected in the future production modules.

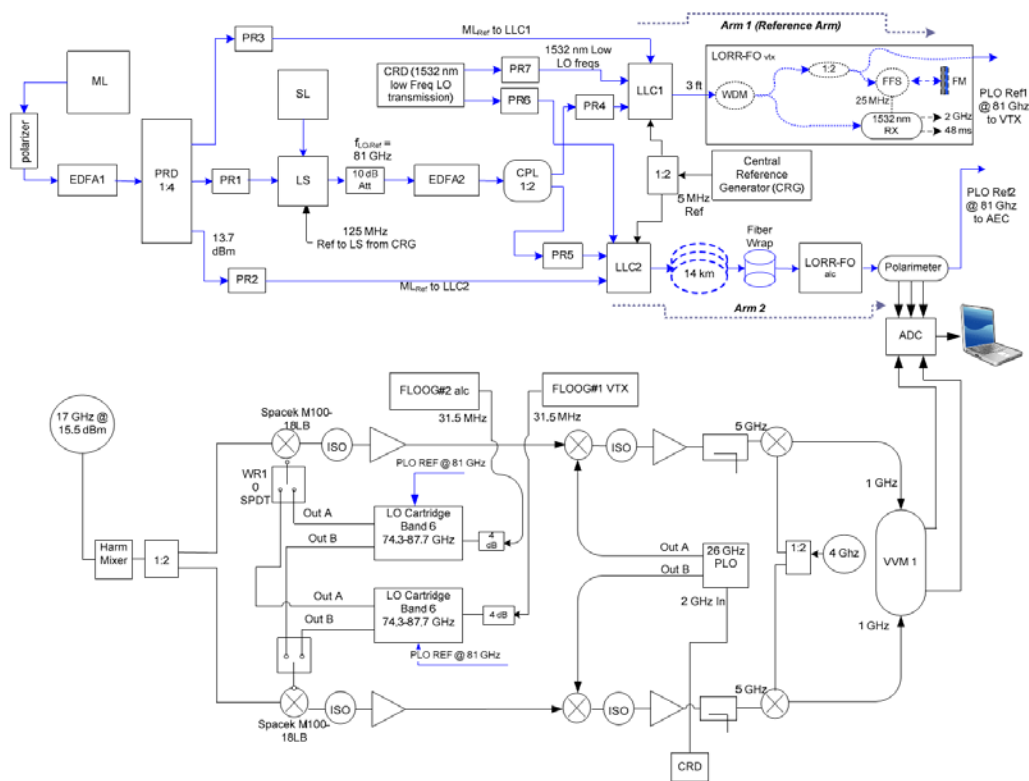


Figure III.5.6.1 A 81 GHz Photonic LO differential phase drift experiment simulating 2 ALMA antennas. The first is a reference length of 10 m (Arm1) and the second with 14 km spool of fiber and a fiber wrap assembly (Arm2).

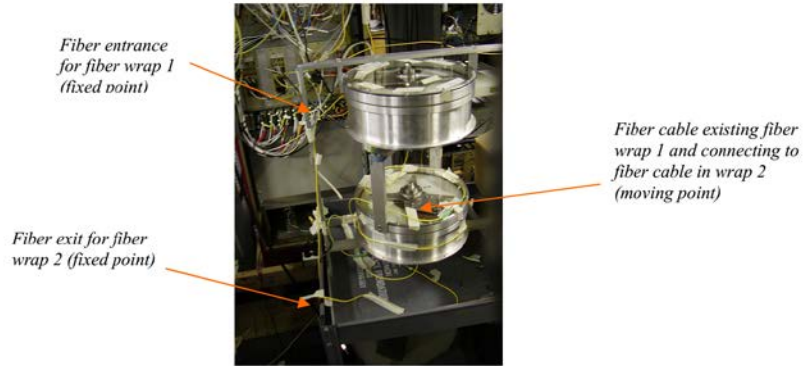


Figure III.5.7.1 A photo showing two units of the prototype fiber wraps that are used in the azimuth and elevation rotations in the ALMA antennas. The two wraps are connected back to back to simulate antenna motion in both azimuth and elevation angles at the same time.

The resulting 6th harmonic 102 GHz signal is fed equally to both arms of the simulated antenna receivers. The first Spacek mixers mix the 102 GHz with the 81 GHz Photonic LO Reference from the WMA cartridges to produce an IF at 21 GHz. That 21 GHz mixes again with the common 26 GHz LO to produce a 5 GHz IF from both antenna racks. We used a Vector voltmeter to measure the difference in the phase of this 5 GHz IFs; however we needed to down convert the 5 GHz signal down to 1 GHz using another identical pair of mixers with a common LO of 4 GHz generated from an Agilent microwave synthesizer due to the limited dynamic operational range of the Vector VoltMeter (VVM). The Agilent synthesizer was externally phase locked using a 10 MHz reference coming from a frequency doubler that doubles the common 5 MHz oscillator generated in the CRG. The two generated IF signals at 1 GHz are theoretically identical and exhibit marginal difference in their phase since they are generated using identical components and the mm wave waveguide equal paths are under the same environmental condition. The WMA used the 81 GHz Photonic LO Reference as a reference to phase lock their perspective YIG oscillators. Therefore in this setup, the phase difference between the 21 GHz signals fed to the VVM is a direct

result of the phase difference between the transmitted 81GHz Photonics LO Reference between antennas. Introducing longer fiber length in arm only or adding any perturbation to any of the arms fiber link will translate into $\delta\Phi$ in the received 81 GHz Photonic LO reference signal in each antenna.

This experiment was broken into two parts. The first is aimed to test the phase drift and evaluate phase correction by the OPSIF in a system that has a long spool of fiber without fiber wrap motion. The second involved measuring the phase drift of the Photonic LO Reference under fiber wrap motion simulating different antenna azimuth and elevation motions. A commercially available polarimeter was inserted in the path of second arm, in-line with the output of the second LORR-FO in order to measure the relative State of Polarization Change (SOPC). The SOPC is produced due to the long term change in of length of the spool of fiber due to temperature and vibration. It is also produced due to the motions introduced in the fiber wrap. The higher induced SOPC the larger the phase drift is. The analogue data produced from the VVM and the polarimeter are sent to a commercially available ADC and read and recorded by in house written LabVIEW code.

III.5.8 MEASUREMENT RESULTS AND ANALYSIS

III.5.8.1 Phase stability without antenna fiber wrap motion.

In this section the differential phase drift of the 81 GHz microwave photonic reference is measured between arm2 and reference arm (arm1) as shown in Figure III.5.6.1 without introducing the fiber wrap motion. Prior to this measurement a suite of baseline tests were performed in an attempt to measure the differential phase drift in the Photonic LO Reference in the instruments and in the common photonic modules. One of the tests was performed by bypassing the OPSIFs and LORR-FO pairs and making arm 2 identical to arm 1 with equally short lengths of cable connecting the output of the optical coupler to both WMA inputs. The main goal of this measurement is to

quantify the effectiveness of the operation of the OPSIFs in canceling out phase drift from a test fiber spool and movable fiber wrap assembly. For this test to work well, the phase must be steady before these two elements are inserted in either of the antenna paths. The Allan Standard Deviation (ASD Φ) for the phase resulted is $\sigma^2=0.1^\circ$ at 81 GHz for a averaging time scale $\tau = 1$ to 10 s, 0.2° at $\tau=100$ s, 0.4° at $\tau=300$ s, and 0.5° $\tau=500$ s. The ASD Φ to the 2-point is a deviation with a fixed averaging time, τ , of 10 seconds and intervals, T , between 20 and 300 seconds. $\sigma^2(2,T,\tau) = 0.5 * \langle [\varphi\tau(t+T) - \varphi\tau(t)]^2 \rangle / \varphi\tau$ = the average of the absolute or differential phase over time $\tau = 10$ seconds, $\langle \dots \rangle$ means the average over the data sample which should extend to 10 or $20 * T_{\max}$ seconds. The source of the differential phase obtained can be coming from any point the 1:2 coupler following the LS and EDFA1.

Next, a spool of 14 km of fiber is inserted in arm 2 while keeping the reference arm at fiber length of ~ 10 m. At first, both OPSIFs were INACTIVE (phase correction is OFF) for ~ 1.2 hrs and then ACTIVE (phase correction is ON) for approximately the same time period as shown in Figure 7. The left y-axis represents the differential phase measured from the VVM, and the right y-axis represents the fast stretcher voltage of OPSIF#2. The orange dashed curve represents the phase of the 81 GHz photonic LO reference in degrees. The saw tooth like profile indicates the resets that were taking place every time the phase of 81 GHz reading goes higher than the VVM dynamic range when the OPSIFs are INACTIVE. The solid orange curve represents the unwrapped 81 GHz phase reading from the VVM after removing the reset points from the dashed orange curve. The blue dashed curve and the blue solid curve represent the control voltage stretcher for OPSIF1 and OPSIF2 respectively. Since the 14 km of spool of fiber was inserted in arm 2 versus 10 m of fiber inserted in arm 1, a 14 km of spool of fiber exhibits larger change in length (ΔL_{fiber2}) than a 10 meter of fiber in arm 1 (ΔL_{fiber1}) due to the thermal expansion in the glass material of the cable.

Typical value for Temperature Coefficient of Expansion for SMF is $\sim 1\text{-}8\text{ppm}/1^\circ\text{C}$ Ref [59]. Due to the thermal expansion effects in a long distance of fiber, OPSIF2 will dynamically correct for a larger induced phase in the 81 GHz signal than OPSIF1 causing the fiber stretcher in OPSIF2 to reach it's minimum limit multiple times before OPSIF1 does. Due to the limited stretcher's dynamic range (1.5 mm in this experiment), a Labview program is employed to reset the stretcher correction voltage every time it reaches its maximum or minimum limit. Consequently, OPSIF2 stretcher resets multiple times from its lower limit to the middle point of the total range. In the first 1.2 hrs of the experiment, the relative phase of the 81 GHz changed by a slope= $814/\text{hr} = 2.26$ complete 360° cycles/hr @81 GHz while the two OPSIFs are INACTIVE. The latter corresponds to a fiber length change ΔL_{fiber2} of 5.58mm/hr assuming glass refractive index $n=1.5$. When the OPSIFs were activated (phase correction is ON), the OPSIF control loop filter applies a correction voltage to the stretcher to zero the relative phase of the 81 GHz transmitted beatnote. In a period of one hour, the fiber stretcher in OPSIF2 stretched a total length = $0.319 \text{ mm/V} * 17.55 \text{ Volts} = 5.59$ mm, which is in a very close proximity to ΔL_{fiber2} when the correction was OFF. The relative measured change in length of the round trip optical path is $\Delta L/2L$ (where $L=14 \text{ km}$) is $\sim 2 * 10^{-7}$ over 1 hour time period. Over one hour, the measured ΔT_{max} was 0.2°C , or $\Delta T_{\text{ave}} = 0.1^\circ\text{C}$. Therefore, for $\Delta T_{\text{ave}}=1^\circ\text{C}$ the $\Delta L/2L$ will be 2 ppm which is in close proximity to the previously reported Temp Coefficient of Expansion for SMF of $8\text{ppm}/1^\circ\text{C}$. A picture of the zoomed version of OPSIFs ACTIVE region only of Figure III.5.8.1 is shown in the top right hand side of Figure III.5.8.1. Resets in the stretcher voltages due to the limited range are translated into jumps in the measured phase of the 81 GHz of $\sim 69^\circ$ indicated in the orange dashed curve. This phase jumps result approximately matches the 2.05 volts change in stretcher voltage during resets, which causes stretcher fiber length to stretch $\Delta L_{\text{fiber}}=0.654 \text{ mm}$ in physical length (electrical length $\Delta\lambda$ of 0.436

mm). Therefore the calculated $\Delta\Phi_{81\text{GHz}}=2\pi*\Delta\lambda/\lambda_{81\text{ GHz}}=62^\circ$. The Allan deviation calculations resulted in a $\Delta\Phi_{81\text{GHz}} < 0.5^\circ$ for $\tau < 300\text{sec}$

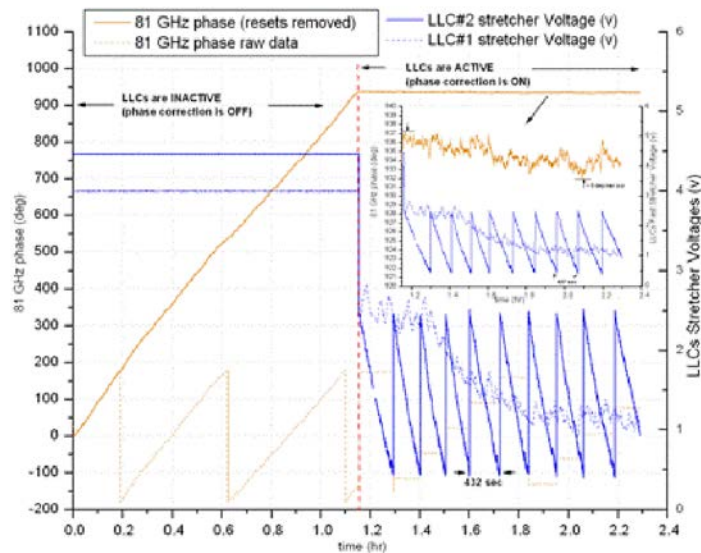


Figure III.5.8.1 The result of OPSIF2 and OPSIF1 correcting the optical phase induced due to fiber lengths of 14 km in arm2 and 10 m in arm1 reference, arm respectively. The orange curve represents the measured $\Delta\Phi_{81\text{GHz}}$ in degrees, and the blue curve represents the correction voltage applied to the fiber stretchers. The OPSIFs were INACTIVE in the first half of the experiment and ACTIVE in the second half.

III.5.8.2 Phase stability with simulated antenna motion

In this experiment, controlled motion was applied to the fiber wrap assembly while the 14 km spool of fiber was still in line in arm2. Accordingly, the total phase drift in the photonic LO consists of two parts. The first is the drift due to the 14 km+10m of fiber in arm 2 &1, respectively. And the second is the drift induced in the system due to the applied rotation of the fiber wrap. The goal of this test is to determine the OPSIFs phase correction ability when the ALMA antennas are in motion. Such mode of operation is essential in the ALMA final system when making a dynamic

observation in the sky. First the test was performed while the OPSIFs are ACTIVE (The correction is ON) as shown in Figure III.5.8.2. Then, the OPSIFs were INACTIVE (The correction is OFF) as shown in Figure III.5.8.3. In each test the assembly of the two fiber wraps were manually and carefully rotated from the initial state of $\theta_{\text{wrap}}=0$ to 720° simulating an antenna motion in both azimuth and elevation $\theta_{\text{ant}}=0$ to 360° at the same time, followed by a back rotation from $\theta_{\text{wrap}}=720$ to 0° which is the initial state. The wrap rotation was performed in a sequence of 8 times when the OPSIFs were ACTIVE, and 4 times when the OPSIF were INACTIVE. The time stamp for the beginning and ending of each rotation event was recorded as shown in the dashed red lines in both Figure III.5.8.2 & 3. In all cases a period of time (80-100 s) was inserted in the sequence where no rotation was applied to the assembly in order to isolate the performance of each rotation and simplify the data readings. The maximum change in phase produced by each wrap rotation is noted in both Figures III.5.8.2 and Figures III.5.8.3. The angular speed at which the rotation was applied varied between 18 deg/s to 8 deg/s. That is 6 to 2.7 times faster than the typical ALMA antenna angular speed in azimuth or elevation direction. Due to the mechanical problem in the prototype fiber wrap addressed earlier in section III.5.7, the 81 GHz phase exhibits few large jumps mostly at the beginning or the ending of each rotation. The recorded phase jumps range between 1.5° to $\sim 9^\circ$. The work in determining the sources of these jumps and the needed design correction for them will be investigated. However, throughout the rest of the cycle of 0 - 360 or 360-0 each wrap assembly rotation the maximum phase change $\Delta\Phi_{\text{max}}$ measured ranged between 0.8° to 1.7° while $\Delta\Phi_{\text{max}}$ ranged from 29° to 45° when the OPSIFs were INACTIVE. The profile of positive slope in the 81 GHz phase drift over time is indicative of the thermal expansion of the 14 km of fiber during the OPSIFs in an INACTIVE state. A much smaller slope in the phase drift plot in the OPSIFs ACTIVE case indicates the OPSIFs phase correction. One

way to quantify the results is to apply the Allan Standard Deviation function ASD_{ϕ} . However due to the limited number of collected samples per rotation and the short time period of each rotational measurement, using the ASD_{ϕ} is not quite revealing. A simpler method is applied here by taking the average of the total RMS values of each measured $\Delta\Phi_{\max}$. In other words $\Delta\Phi_{\text{ave-rms-81 GHz}} = 1/n \cdot \sum \Delta\Phi_{\text{rms}}$, where n is the number of each applied rotation to the fiber assembly. In doing so we get $\Delta\Phi_{\text{ave-rms-81 GHz}} = 16.2^{\circ}$ for the OPSIF INACTIVE case and 4.1° for the OPSIF ACTIVE case. Figure III.5.8.4 summarizes and compares the $\Delta\Phi_{\text{rms-81 GHz}}$ (including the undesirable phase jumps observed) for the case when the OPSIFs were ACTIVE and INACTIVE. The data includes the undesirable phase jumps mentioned earlier. The OPSIFs were able to dynamically phase stabilize ~75% of the total induced 81 GHz RMS phase shifts related to the fast rotation of the fiber wrap assembly and the thermal expansion of the 14 km of spool of fiber in arm 2 of the test setup.

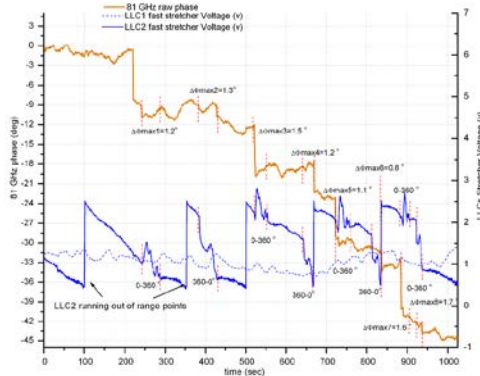


Figure III.5.8.2 The differential phase measurement of 81 GHz Photonic LO reference between 2 antenna racks with 14 km of fiber and fiber wrap assembly between central LO rack & antenna2 & 10 m between central LO rack and antenna#1. Both OPSIFs were **ACTIVE** when the fiber wrap assembly was under 8 separate controlled rotations from 0° - 360° and 360° - 0°

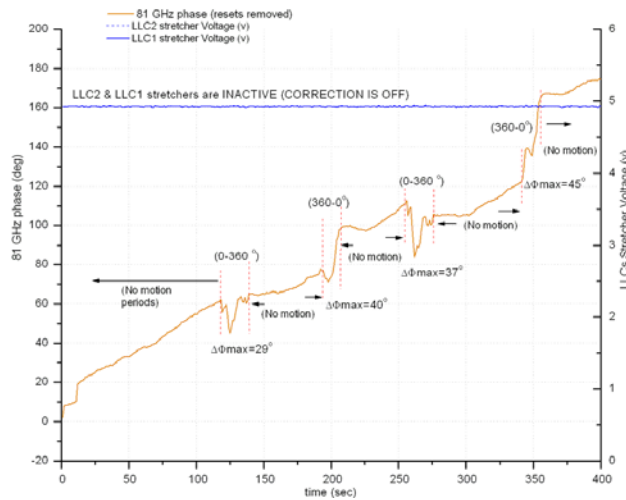


Figure III.5.8.3. The differential phase measurement of 81 GHz Photonic LO reference between 2 antenna racks with 14 km of fiber and fiber wrap assembly between central LO rack & antenna2 & 10 m between central LO rack and antenna#1. Both OPSIFs were **INACTIVE** when the fiber wrap assembly was under 4 separate controlled rotations from 0° - 360° and 360° - 0° .

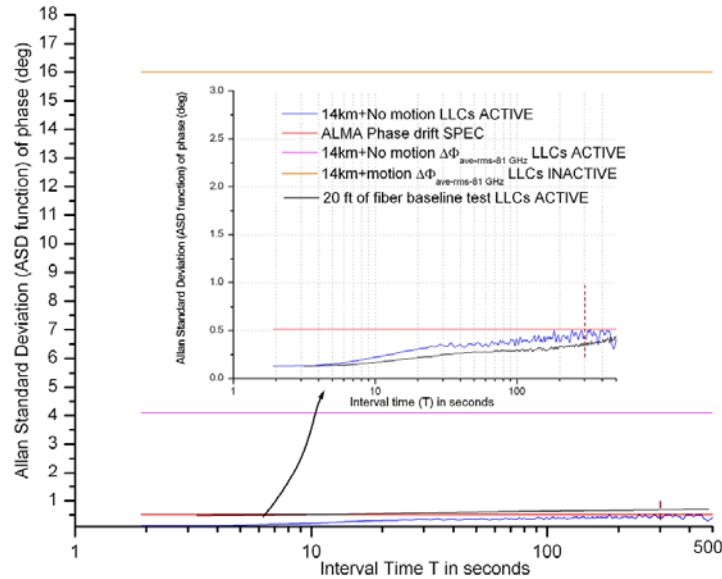


Figure III.5.8.4 The Allan Standard Deviation Φ calculation for the residual 81 GHz phase in case of the baseline with 20 ft of cable length (black curve), 14 km of fiber without applied rotation to the fiber assembly with OPSIFs ACTIVE (blue curve) compared to the ALMA phase drift spec of 0.51deg at 81 GHz (red line). Added to that is the calculated $\Delta\Phi_{ave-rms-81\text{ GHz}}$ in the case of 14 km of fiber with applied rotation to the fiber assembly while OPSIFs ACTIVE (pink line) and INACTIVE (orange line).

The results of the phase drift are compiled and shown in Figure III.5.8.4. The figure lists phase drift measured using ASD_{Φ} to quantify the phase drift in the case of no fiber assembly rotation applied, and using the calculated $\Delta\Phi_{ave-rms-81\text{ GHz}}$ for the case of rotation applied to the fiber assembly with OPSIFs ACTIVE and INACTIVE. A clear comparison can be made at fixed interval time (such as $T=300s$) showing the phase correction in all listed cases. It also shows some of the limitation of the OPSIFs phase correction while rotating the fiber assembly in not meeting the required ALMA specifications.

This section describes and details the basic concept of operation of the major elements of the photonic LO microwave reference generation and distribution system for the ALMA prototype array. The high coherence and ultra-sensitivity requirements for the ALMA resulted in developing hardware systems that are frequency stable and have very low phase noise and phase drift characteristics. Employing photonic based systems that utilize highly stable and narrow line width lasers, together with careful design of the control phase locked loops made it possible to achieve the measured phase frequency stability and low phase noise. The technique used by the OPSIFs to interferometrically measure the round trip phase of the distributed photonic LO to each antenna was very successful. The OPSIF's capability to dynamically correct the unwanted phase changes due to the simulated motion of the antenna was demonstrated. Work is still underway to enhance the performance of the OPSIFs and the fiber wrap assembly. Future work on the OPSIF will focus on reducing the resulting SOPC inherent in the system and optimizing the feedback loop system to better stabilize the phase to several ms. currently, the operational production antennas are being evaluated in Chile. The Photonic LO production will be installed and test in middle of 2008. Once the ALMA instrument is fully operational, it will provide a new, powerful window into the workings of the Cosmos.

CHAPTER IV: ATOMMS QUISIOPTICS LENS

DESIGN

In this chapter a detailed design of a HDPE (High Density Poly Ethylene) anti-reflection grooved lens antenna that is illuminated by 2 separate corrugated coaxially located Feed-Horns (FH) is presented. The lens antenna is placed coaxially with the feed horns for the two different frequency bands. We present the design, optimization and initial testing of the feed and lens system. The lens design was needed to complete the 1st prototype quasi optics system for the ATOMM's instrument.

The limited space inside the gimbal system put some constraint on the design options for the quasi-optics. It would have been easier to design the system such that the 22 GHz and the 200 GHz had their own separate feed and antenna, or to use reflective based antennas. The configuration is shown in Figure (V.1) where the 2 FHs are coaxially placed, separated by the total length of the 200 GHz FH and the polarizer that is attached to it. In this design configuration (MARK I.) the FHs are designed to symmetrically illuminate their beams into a single common refractive lens antenna, this scheme was used both in the receiver side and the transmitter side of the ATOMMS instrument

The earlier system performance evaluation suggested that this configuration might cause an obscuration of the 22 GHz beam by the 200 GHz FH and the plastic spider that holds it both in the transmitter and at the receiver. However, the previously analysis carried out by an outside consultant showed that the impact on the system performance such as pointing error, amplitude stability will be minimal such that it was safe enough to carry on with that design (MARK I.) of a single lens optical system. The decision was made then to build the system and therefore a lens antenna was needed to be designed. In the next chapter we show that earlier analysis was crude and its findings were not accurate. The later measurement carried out coupled with full analysis showed that the MARK I design caused the obscuration of the 22 GHz which lead us to redesign

the optical system. The latter work is covered in Chapter V.

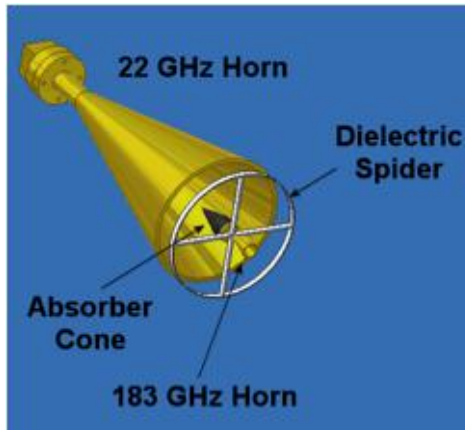


Figure IV.1: The simplified quasi-optics system diagram showing both the 22GHz & 200 GHz FHs, 30 cm lens antenna, a dielectric spider and absorber cone.

IV.1 ATOMMS QUASIOPTICS SUBSYSTEM

The goal of the quasioptics subsystem is to produce two coaxial collimated beams using a single lens antenna. The performance was optimized for the 200 GHz such that the 22 GHz optical beam didn't suffer from too much losses. The maximum allowed space for a lens to fit in that small geometry is about 40 cm. However, as a first step in the design, a lens of diameter $D=30$ cm was chosen, since it is a standard size commonly used in the past, especially in the satellite industry. Free space Gaussian beam propagation theory has been used to analyze the beam propagation entering or existing the FHs and the lens antenna assembly. Since we illuminate the lens symmetrically, conical FHs are used with corrugations to minimize the VSWR. Corrugated conical FHs generate a balanced hybrid mode (HE₁₁) if they are sufficiently large such that $2\pi a/\lambda > 1$, where a is the largest dimension of the source of radiation which is estimated to be 1.7cm for the case of this 200 GHz FH. The HE₁₁ modes have field distributions that are azimuthally

symmetric and are uniformly polarized. The axial symmetry of the field distribution provides an excellent coupling to the lowest Gauss-Laguerre beam mode ($m=0$). A maximum power coupling ratio $|c_0|^2$ of 98% of the fundamental mode of Gaussian beam and HE₁₁ mode can be achieved if beam radius w is equal to $0.644a$ of, where a here is the diameter of the FH. Some of the design guidelines used in this chapter have been well researched and well established in the literature, such as the coupling of Gaussian beam into the radiating elements is well covered in chapter 7 in [60] The following sections will show the steps taken for the design of the on-axis Gaussian beam parameters for the 22 and 200 GHz bands. Once that is done the specifications for the FH are chosen, basic type of antenna choice is made with estimated losses associated with it. We used ray tracing with (Zemax) in order to optimize the spot size at focus.

IV.1.1 200 GHz Quasi-optics system

One of the 200 GHz science requirements is to meet a pointing accuracy between the two aircraft of 0.57° . Roughly speaking that forces the diameter of the lens antenna to be 15 cm. Since we are using a 30 cm diameter lens, the 200 GHz FH is used to illuminate the lens with very Using $G_{193.5G}=20\log(\pi D/\lambda)$ with $D=15\text{cm}$, and $G_{193.5G}=49.66\text{ dB}$, the 1-D HPBW is determined from (11) [62]:

$$G_{193.5G} \sim 30'000/(\varphi_x \cdot \varphi_y) \quad (11)$$

$\varphi_x=\varphi_y=0.57^\circ$ for symmetrical antenna illumination.

The 1-D edge taper (T_e) defines the normalized E-field at the antenna with respect to its aperture radius [63].

$$T_e \text{ (dB)} = [\varphi \text{ (in rad)} / (\lambda/D) - 1.02] / 0.0135 \quad (12)$$

From equation (2), T_e is found to be 67 dB at 193.5 GHz. From the T_e we determine all the parameters of the Gaussian beam propagation at the lens, and propagating the beam backward to the FH to determine the beam waist w_o . The beam radius at the 30 cm antenna aperture is easily calculated also from [62].

$$\alpha = 0.115 * T_e \text{ (dB)} = (r_a/w_a)^2 \quad (13)$$

For 1-D, $w_a = 5.4$ cm, and selecting an initial distance from the FH to the back surface of the antenna to be $z_{193.5G} = 12.1'' = 30.73$ cm, we can solve for w_o , and then for z_0 using (14) and (15):

$$z_0 = \pi w_o^2 / \lambda_{193.5G} \quad (14)$$

$$w(z)^2 = w_o^2 [1 + (z/z_0)^2] \quad (15)$$

$$R_{193.5G} = Z_{193.5G} (1 + [\pi w_o^2 / (\lambda_{193.5G} Z_{193.5G})^2]) \quad (16)$$

$$\theta_o \sim 1.18 \lambda / (\pi w_o) \quad (17)$$

Where:

The $z=0$ plane is defined to be at the aperture of the FH and $z_{193.5G}$ is the distance away from the aperture of the FH to the back surface of the lens.

$z_0 =$ confocal distance (Rayleigh length) = 14.9 mm.

$w_o =$ beam waist = 2.701 mm (where the E- field is at maximum) and the wave front is flat (or plane)

and the on-axis phase shift φ_o is 0.

$R_{193.5G} = 31.46$ cm at the back surface of the lens (at $z = z_{193.5G} = 30.734$ cm away from the 200 GHz

FH.

$\theta_0 \cong 12.4^\circ$ is the far-field divergence angle. In most quasi-optics system designs it is important to address the location of the phase center of the beam with respect to the FH aperture Δpc (offset of the phase center relative to the beamwaist) [62]

$$\Delta pc = -\frac{(\pi \omega_0^2 / \lambda)^2}{z} \quad (18)$$

$$z = \frac{R_h}{1 + |\lambda R_h / \pi(0.644a)^2|^2} \quad (19)$$

R_h is the slant length of the FH. Δpc becomes more important if higher modes of the Gaussian beams are included in the design. The calculated value for Δpc was ~ 1.11 cm. Typically the E-field that excites the waveguide feeding into the FH is linearly polarized, however in order to minimize the losses due to the relative orientation between the 2 aircrafts while in the air, we chose to have a circular polarizer to be placed between the waveguide and the FH, the output then is RHC (Right Hand Circular) for one of the instrument and LHC (Left Hand Circular) on the other one. Adding the polarizer makes the total length of the assembly to be 6.06 cm, which causes the 22 GHz band FH to be placed at least 6.06 cm behind the 200 GHz FH. Since the transmitted and the received power through the 22 GHz system are considerably higher than those of the 200 GHz system, it was important to make sure that the lens antenna was designed to have maximum gain and minimum losses at the 200 GHz center band. Consequently, the 22 GHz signal will see more losses, both due to the FH blockage and due to the defocusing of the lens. However, it was decided that these losses can be mitigated by increasing the transmitter power.

The output beam waist (w_{out}) and the distance from the system output plane to the output beam waist are calculated using Gaussian beam transformation method. Since $z_{in}=f=30.73\text{cm}$ (the beam waist is located at the front focal plane), $z_{out}=f$ (output beam waist (image waist) is found to be at the back focal plane of the lens with $w_{out}=5.37\text{ cm}$. This is very different from the imaging in geometric optics, since we expect placing a source at the front focal plane would produce an image at infinity. The Gaussian beam will behave much more like a spherical wave if z_o/z approaches 0, or $z \gg z_o$. As a result the output divergence angle is found to be close to 0.5° , and the output beam is for the most part collimated. Also $z_{o_200Gout}=5.89\text{ m}$ with system magnification at maximum $M_{max}=20$.

IV.I.2 22 GHz Quasi-optics system

As a first step, in the evaluation of 22 GHz quasi-optic system design, the outside consultant used CST microwave to examine the quality of the 22 GHz beam pattern in the far-field region when the spider and the 200 GHz FH obscuration are placed 6.06 cm in front of the 22 GHz feed. In order to shorten the simulation time the model was over simplified. The spider was included in the simulation without the 200 GHz FH, it was thought that adding Microwave absorbers [MODEL ECCOSORB MFS-124] will eliminate any unwanted effects of diffraction and will minimize reflections inside the 22 GHz beam path in particular, and reduce unwanted reflections in general. The dimensions of the 22 GHz FH were estimated for 22.5 GHz excitation. Figure IV.1 shows the simplified geometry used without including the 183 GHz FH.

Figure IV.2 shows the 22 GHz FH E and H-plane beam patterns, at the spider legs and 45° away from spider legs. The dotted and solid lines represent the orthogonal polarization patterns (E & H-planes). While the 22 GHz beam pattern is degraded by the presence of the spider and the central

blockage, the overall system performance didn't show the effect of the blockage which lead us to accept the current design configuration. However, as we will see in the next chapter, a much more thorough evaluation of this design configuration showed large diffraction effects due to the 200 GHz FH which found to be in agreement with corresponding measurement made.

The Gaussian beam propagation calculation for the 200 GHz system was repeated here for the 22 GHz with a few differences. Assuming 0.55 aperture efficiency, the gain of the circular lens antenna at the middle of the 22 GHz band is 34 dB using Eqn (20).

$$G \approx 10 \log [0.55(\pi D / \lambda)^2] \quad (20)$$

Using, the same Gaussian propagation equations for one dimension we find that for the 22 GHz beam, $\phi_x = \phi_y = 3.304^\circ$, $T_e = 20.5$ dB, $w_a = 9.99$ cm at the antenna back surface. At $z_{22G} = 36.79$ cm (30.73+6.06cm) away from the lens, $w_{o-22G} = 1.58$ cm, $z_{o-22G} = 5.9$ cm, and the radius of curvature at the back surface of the lens is $R_{22GHz} = 36.92$ cm, $\theta = 18.2^\circ$.

IV.1.3 Lens selection and Zemax simulation

The distance between the 2 aircrafts is very large (from 20 km to 1000 Km). With this configuration modeled as having a point source at a vey large distance such that received waves behave like plane waves ($R_{in} \sim \infty$). We use a single lens to focus the incoming beam to a smallest spot possible at the 200 GHz FH aperture. Using the thin lens equation below:

$$1/R_{out_200GHz} = 1/R_{in_200GHz} + 1/f_{200GHz} \quad (21)$$

$R_{out_200G} = f_{200G} = 30.79$ cm. Since we are interested in a simple, low-cost design, low absorption loss, therefore the smallest central thickness is desired. However, at the same time the material of the lens needs to be hard, mechanically stable, relatively inexpensive for higher altitude

environment, cheap and easy to machine. At first two materials were considered, Rexolite ($n=1.59$ @ 200 GHz), and HDPE [63] ($n=1.529$). Rexolite was found to have high losses (close to 4.8 dB for a center thickness $t_c = 6.5$ cm), therefore HDPE (High Density Polyethylene) was chosen as the basis of the lens design. The estimated absorption losses of < 1 dB for the same t_c . At first our model used values of index of refraction found in the literature [70]. We were then able to use empirical values based on an in-house index of refraction measurement of samples of the actual material the lens was fabricated from. Using Time Domain Spectroscopy (TDS) techniques for 30 samples the average measured n at 193.5GHz was $=1.520$ with maximum sample-to-sample measuring error of 0.092%.

The empirically obtained index of refraction was used to improve the Zemax lens design parameters. Spherical-plano shaped lenses were avoided for this application as they tend to be thicker ($t_c=10.85$ cm) compared to hyperbolic-plano lens designs. In a first step we optimized the lens design for the 200 GHz beam only without including the 22.5 GHz beam. The optimization criteria chosen were: First, to achieve the smallest focused spot size, and second, to achieve the lowest optical path difference (OPD) with respect to the chief ray in the y direction (the x -directions results are identical), all this while keeping the thickness as small as possible, and therefore minimizing transmission loss. . The optimized spot size, and the OPD are shown in Figure IV.3 top and bottom, respectively. Previously, the estimated aperture diameter of the 200 GHz FH was 11.36 mm.

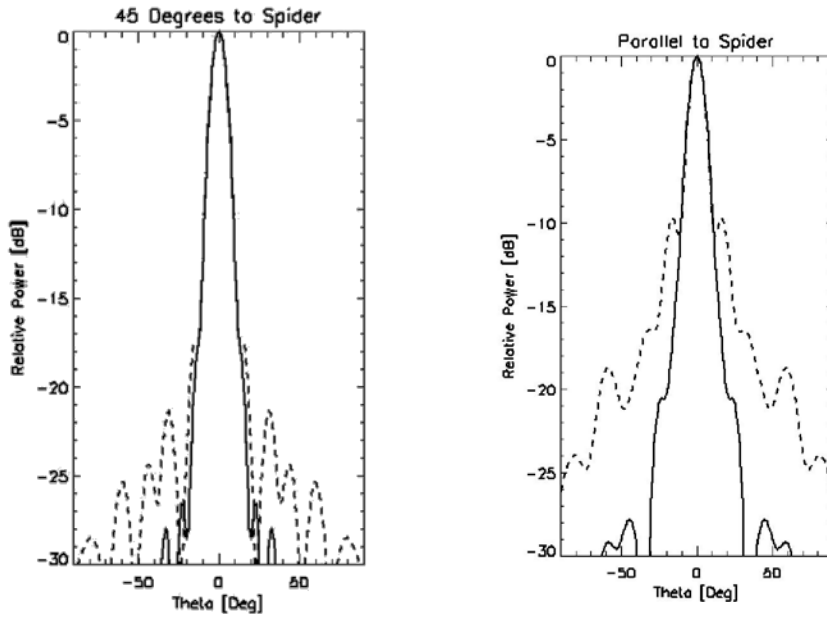


Figure IV.2 E & H-field beam pattern (solid and dotted line respectively), with respect to the angle θ , with $\theta=0$ (top) (parallel to the dielectric spider), and 45° tilt away from it (bottom).

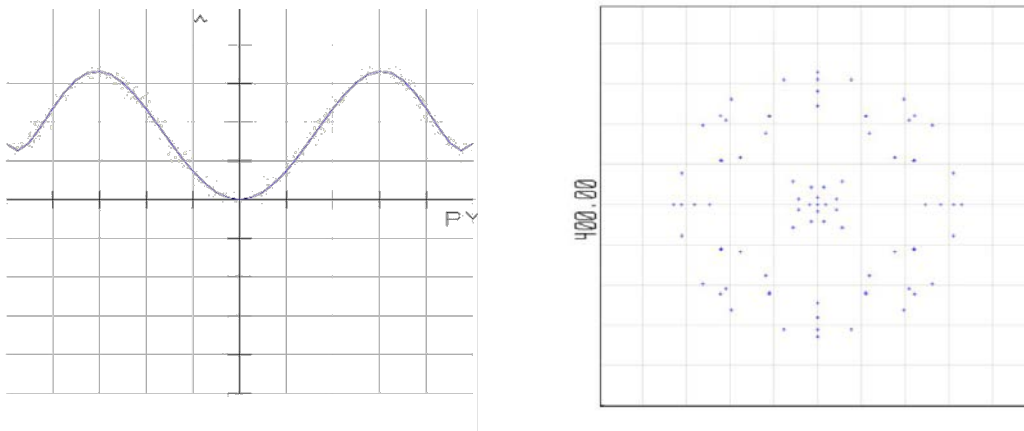


Figure IV.3. The spot size in in μm at the 200 GHz FH aperture (top), $40 \mu\text{m}/\text{div}$ and the optical path difference (bottom) with respect to chief ray in waves at the wavelength of 0.155 cm.

The design and manufacturing of the FHs were done by Quinstar microwave after providing them with required Gaussian beam parameters. A spot size of $\sim 260\mu\text{m}$ is well centered within the 10.58

mm diameter of the FH. The optimum value of the central thickness of the lens was 7.5 cm. The first Zemax optimization for the 200 GHz beam caused the incoming 22 GHz beam to be focused at ~ 5.3 cm to the right of the 22 GHz FH aperture, which caused the 22 GHz system to operate in a defocused mode. The antenna gain reduction due to the defocus can easily be calculated using (12) in [62]. (12)

$$\varepsilon_a(\delta) = \frac{\varepsilon_a(0)}{1 + (\delta/z_o)} \quad (22)$$

Where $\varepsilon_a(\delta)$ is the antenna efficiency for a Gaussian illuminated beam with a defocusing distance of $\delta=5.3\text{cm}$, and $\varepsilon_a(0)$ is the antenna efficiency when the Gaussian beam is in focus. The defocusing losses becomes $10 \log (\varepsilon_a(\delta)/\varepsilon_a(0))$ which results to about 2.3 dB gain reduction. As mentioned earlier, the losses in the 22.5 GHz system are easily compensated by the provided extra gain provided through various attenuators placed in the 200 GHz microwave chain. The resulting defocused beam radius centered at the edge of the 22 GHz FH is obtained to be $w_{22\text{GHz}_{\text{new}}}= 2.24 \text{ cm}$, indicating a growth of only 6.5 mm from its $w_{o_{22\text{GHz}}}$ location. After a sequence of design optimization in Zemax, the resulting lens surface produced fits exactly polynomial of the 10th degree.

IV.2 LOSS CALCULATION & MEASUREMENTS

Since the goal of this design is to balance the performance of the 200 GHz system with that of the 22 GHz system, we designed and produced an AR-layer in the two lens surfaces to reduce reflections of the 200 GHz transmitted and received beams. Our approach has well been

established and has been used for many years in radio astronomy [64]. The method involves machining circular grooves in the two surfaces such that the resulting surfaces acts like a matching layer with an effective index of refraction n_{eff} , such that $n_{\text{eff}} \sim n^{1/2}$. This procedure provides better matching impedance to free space resulting in a reduction of reflection loss. For frequencies up to 400 GHz, grooving the surfaces with circular grooves is done via micro machining with a CNC milling. This method creates a well-defined topologies with depth $d=\lambda/4n^{1/2}$ depth and pitch values, and a filling factor that determines the value of the n_{eff} . In [65] and [66] 1-D structures have been investigated and used in the past such as rectangular, multi-step, or sine wave-grooves, and 2-D structures are also known with structures like rectangles and holes. 1-D structures are more likely to be polarization dependent and might be birefringent than 2-D structures. The design selections for the groove's specific pitch, depth and filling factor were done by studying examples in the listed literature as well as by using the program "SCATTER " written by R. Padman [67]. Reflection losses for a single surface dielectric material can be expressed for normal incident as in Eqn. (23):

$$L_{\text{ref}}=10\log\frac{(n-1)^2}{(n+1)^2} \quad (23)$$

Calculating L_{Ref} show that for $n=1.52$, $L_{\text{Ref_ungrooved}}=-13.7$ dB, however for a grooved surface with estimated $n_{\text{eff}}=n^{1/2}=1.23$, $L_{\text{Ref_grooved}}=-19.7$ dB. The above calculation ignores the effect of variation of index of refraction with frequency, which will have small impact on the calculated reflection. The effect of the second surface reflectance is also small compared to the material loss for a center thickness of $d=7.6$ cm. In order to count for the 2nd surface reflection, we reduced and suitably parameterized eq (59) in [68] for normal incident in air media ($n_1=n_3=1$), which resulted in $L_{\text{Ref_2surf_ungrooved}} \cong -14$ dB, and $L_{\text{Ref_2surf_grooved}} = -19.75$ dB. From the reported values of loss

tangent $\tan(\delta)$ for dielectric materials, its found to be $\cong 4e-4$ for HDPE. The resulting material attenuation loss for a 7.6 cm thick is found to be -0.85 dB at 183 GHz and -0.94 dB at 203 GHz, which is much larger than the extra loss added due to the 2nd surface reflection. The result of the averaged through transmission and material loss of simulating two grooved surfaces sandwiching the lens material using program “SCATTER ” with thickness of 6.4 cm is shown in Figure IV.4.

The total transmission T_{total} , where $T_{\text{total}} = T_{\text{surface1or2}}^2 + A$ (the material loss = -0.85 dB) is found to be -0.92 dB at 183 GHz. Therefore:

$T_{\text{surface1or2}}$ is found to be 0.992. The reflection of a single grooved surface based on $R=1-T$ is then \cong -20.9 dB. Repeating the same calculations for $f=203$ GHz results in a single surface reflection - 19.34 dB. The simulation and the earlier calculations above are in a very good agreement showing approximately an average reduction in reflection of about $\cong 6$ dB. The concentric lines of grooves were applied to the center of the two surfaces of the lens up to $r=15$ cm, since the main lobe of the 200 GHz beam will be centered on that area. Comparative reflection measurement was performed using a THz Time Domain Spectroscopy (THz-TDS) system. In THz-TDS ultra short pulses are generated that last only a few picoseconds. Each pulse creates broadband radiation from 0.05 to 2 THz. At the receiver the E-field of the terahertz pulse is sampled and digitized. A delayed femtosecond optical pulse gates the receiving dipole antenna “ON” through an identical LT-GaAs semiconductor. By repeating this procedure and varying the delay of the gating laser pulse, it is possible to scan the THz pulse and construct its E-field as a function of time with 0.1picosecond resolution over a 1 nanosecond time period. Subsequently, a Fourier transform is used to extract the frequency spectrum from the time-domain data. THz TDS was used to measure the reflection of the grooved lens surfaces as shown in Figure IV.5.

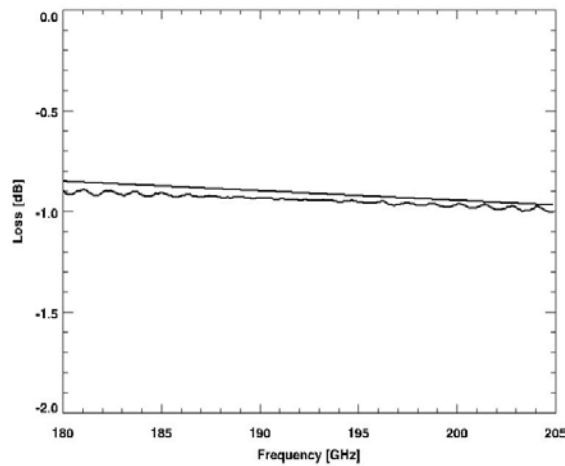


Figure IV:4 Reflection and absorption losses versus frequency for a grooved HDPE lens with $n=1.52$. The straight line is just the material losses, and the Fabry-Perot reflection line is material losses plus reflection losses, simulated using program “SCATTER” written by R. Padman [67].

The linearly polarized in the x-direction THz E-field beam is propagated through the Polarization Beam Splitter (PBS), and a Quarter Wave Plate (QWP) that changes the Polarization from linear to circular. As the beam reflects back from the lens surface, the incident circularly polarized beam changes its handedness. By the time it pass through the QWP in the second pass, it become linearly polarized in the same plane as the wires of the PBS such that it reflects into the THz Rx. In this experiment the QWP used was centered at $\cong 350$ GHz, which will make the polarization more elliptical rather than linear, which could introduce some coupling and or cross polarization losses into the receiver. The results of the reflection measurements are shown in Figure IV.6. The red curve represents the reflection coefficient of the grooved surface and the blue for the un-grooved surface. Since the majority of the incident beam will be transmitted through the lens in the case of grooved and the un-grooved surfaces, the measurement of the reflected beam in this case is clearly

dominated by the 1st surface reflection (-13.7 dB) since adding the material and 2nd surface reflection will give (-13.6 dB). At 183 GHz we see a difference of $\cong 8$ dB and 9 dB at 203 GHz between the grooved and un-grooved data plots, which is 2 to 3 dB higher than what was predicted in the simulation and calculations. Understanding fully the reasons of the differences between the calculated and measured values for both the grooved and un-grooved surfaces are not totally resolved nor concluded in this paper, and will continue to be a topic of an on going study in our group. However, it is our understanding that the factors that contribute to these differences could range anywhere between losses due to beam alignment errors, beam proper coupling, cross polarization and stigmatism losses. For example, it is highly likely that difference of $\cong 4.3$ dB observed between the calculated and the measured reflection in the un-grooved surface case could be related to the rise of polarization losses at the receiver. Since the QWP used is not centered at 200 GHz it will result in producing an elliptically polarized beam incident on the surface of the lens, which could cause polarization losses at the receiver after passing through the rest of system.

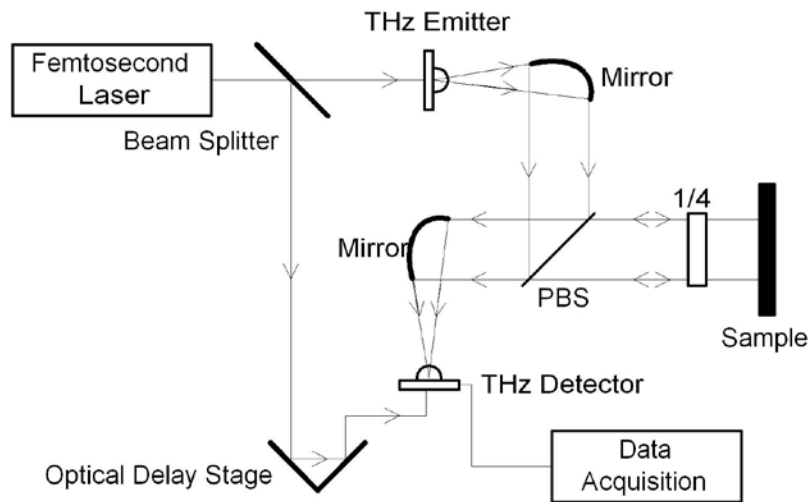


Figure IV.5 THz Pulse TDS reflection measurements setup diagram of the grooved and un-grooved surfaces of the HDPE lens.

Another example will be the observed difference of $\cong 6$ to 7.2 dB between the calculated and measured values of reflection in the case of the grooved surface could be due to the cross polarization losses and stigmatism. The latter loss factors might be present when a polarized wave is incident on a material with effectively an anisotropic surface. This situation is highly likely to occur since the index of refraction of the grooved surface exhibits a variation in the x-and y-directions due to the grooves, which that might not be symmetric. Cross polarization and stigmatism losses produced could both be in the order of 0.2% of the reflected beam which calculated to be $\cong (-7.8$ dB), as has been shown in J. Lamb analysis and simulation work in [69]. A much more comprehensive analysis for these previously discussed topics may be carried out in future publications. It is important to also mention that the design for a large bandwidth AR dielectric coating and optimized for selective frequencies using the grooving technique is extremely hard to make especially as the frequency of interest increases

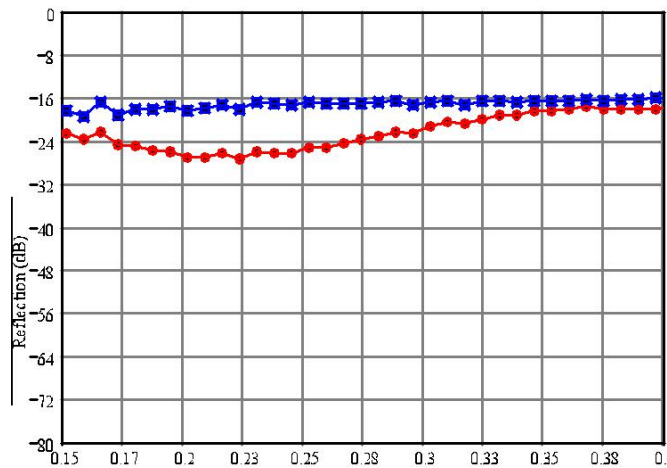


Figure IV.6: THz TDS reflected E-field measurements for the grooved (red) lens flat surface and un-grooved (blue) flat surface with respect to frequency (THz). Reflected losses for the un-grooved

surface at both 183 GHz and 203 GHz is $\cong -18$ dB, while at the grooved surface the total losses are -26 dB at 183 GHz and -27.2 dB at 203 GHz.

Our initial design specifications for the groove's depth it was such that the grooves will induce the maximum matching to air in the middle of the 200 GHz band $\cong 193.5$ GHz. The resulting desired groove depth was found to be 0.314 mm, however the measured grooves depth in the delivered HDPE lens that is under test was 0.264 mm exceeding the tolerance of ± 0.025 mm. The difference between the preselected and measured depths caused a shift of $\cong 36.5$ GHz in the minimum observed reflection from the grooved surface as shown in Figure IV.6, where at 230 GHz the reflection is at minimum of -28 dB. However, from the overall quasi-optics system design point of view, a minimum of a 6 dB reduction in the reflection across the desired 200 GHz band has been met, and is considered very acceptable.

In this chapter we describes the ATOMMS instrument MARK "T" quasi-optical system design. We have also covered the procedure used in designing a lens antenna for both the 22 GHz and the 200 GHz TX/RX optics system by means of employing Gaussian beam propagation, and geometric optics. The goal was to make the coupling of the 200 GHz & the 22 GHz beams into their perspective feed horns as high as possible, and to minimize both reflections back to the transmit FHs and losses. This chapter included the reflection measurements and the effect of anti-reflection coating the surface of the lens by adding concentric grooves, which resulted in a reduction in the reflection of 6 dB.

In the next chapter we will cover the first hand measurements that lay out the performance of this system and comparing it with the expected performance.

CHAPTER V: ATOMMS QUASIOPTICS

CHARACTERIZATION

V.1 Introduction

The results of the first mountain to mountain test of the ATOMMS prototype instrument with MARK “I” Quasi-optics design indicated two problems in the performance of the 22 GHz system. First, that the center of peak of the 22.6 GHz received beam by ATOMMA A is significantly reduced and second its amplitude is very unstable. These symptoms were observed for all the tones within the same band. The generated hypothesis was that there is a problem in the alignment of the feeds to the optical axis of the lens antenna. The misalignment problem was characterized in the lab using autocollimators (the detailed analysis is not covered in this chapter). The focus was drawn to the MARK “I” quasi optics design and more particularly the issue of the 200GHz FH position and its impact on the 22GHz band performance both in the TX and in the RX. A detailed and more thorough analysis coupled with measurements was needed to understand the results of the Mountain-to-Mountain obtained tests results. The test and analysis for this subject is covered in this chapter. This chapter is structured as follows: Section II will cover the far-field measurement for the MARK “I” design coupled using FRED simulation to back up the results of the far-field measurement. Section III will further analyze the problem using diffraction theory and the results are then discussed and compared to the ones found in Section 2. Section IV will summarize the design options and list the advantages and disadvantages for each. Section V will cover the detail design requirements as they are driven from the instrument performance requirements. Section VI will cover the lens methodology for the 22 GHz band finalized with zemax design and analysis results.

When the current design MARK “I” was complete and the prototype built, it was assumed that the blockage by the 183 GHz feed horn will not impact the 22 GHz beam quality and power significantly such that will jeopardize the performance of the 22 GHz feed system. Yet, we

indicated that the 22 GHz is not behaving as a correctly focused Gaussian beams. Therefore a further investigation to the effect of the blockade from the diffraction point of view is necessary for a better understanding of the problem.

V.2 The 22 GHz FH Far-field Measurements

The objective of this test is to understand the effect of the 200GHz feedhorn on the quality of the 22GHz beam transmitted by ATOMMS B and received by ATOMMS A. A simple test is done without the 30 cm lenses in place are to measure the beam pattern of the 22 GHz with and without the 200GHz in place. Two important criteria needed to be met:

(1) That we are operating in the far-field region such that other diffraction effects would not skew the results.

(2) Perform the measurement in an environment that exhibits minimum multipath effects. The ideal situation would have been done between two mountain tops, however given the constrains of project schedule it was decided to perform the test on the ground at the campus of the University of Arizona. The goal was to obtain the beam pattern from -45° to 45° range. In order to minimize Multipath reflections, sheets layers of Eccosorb MODEL EN-072 material were placed on the ground between the two instruments around, and inside the instruments behind the feedhorns) to minimize any large reflections and standing waves in the measurement path. Figure V.1 shows the test setup. The Far-field distance is the distance between the object/source and the observation plane L_{fh} such that it is in the Fraunhofer region which occur when $L_{fh} \gg D^2/\lambda$, with $D_{22GHzFH} = 5.1$ cm L_{fh} is listed below for all wavelengths of the 22 GHz band. However we should also consider the L_{fh} for the receiving FH as well. Therefore the minimum distance required between the instruments are shown in Table V.1

The distance between the two feedhorns when measured was 21 m \gg 0.63 m. The TX instrument was fixed in place while the RX was sweeping in azimuthal angle between -60° and $+60^\circ$, however only -20° to 20° were plotted since we are only concerned with center portion of the beam. Figure V.2 through V.4 through shows the test results of the beam patterns with and without the 200 GHz FH in place for 18.5, 22.5 and 25.5 GHz.

Lfh [m]	f [Ghz]	λ [mm]
0.4589233	18.5	16.216216
0.48373	19.5	15.384615
0.5333433	21.5	13.953488
0.55815	22.5	13.333333
0.5829567	23.5	12.765957
0.6077633	24.5	12.244898
0.63257	25.5	11.764706

Table V.1: Far field distances for the 22 GHz TX RX pair feedhorns.

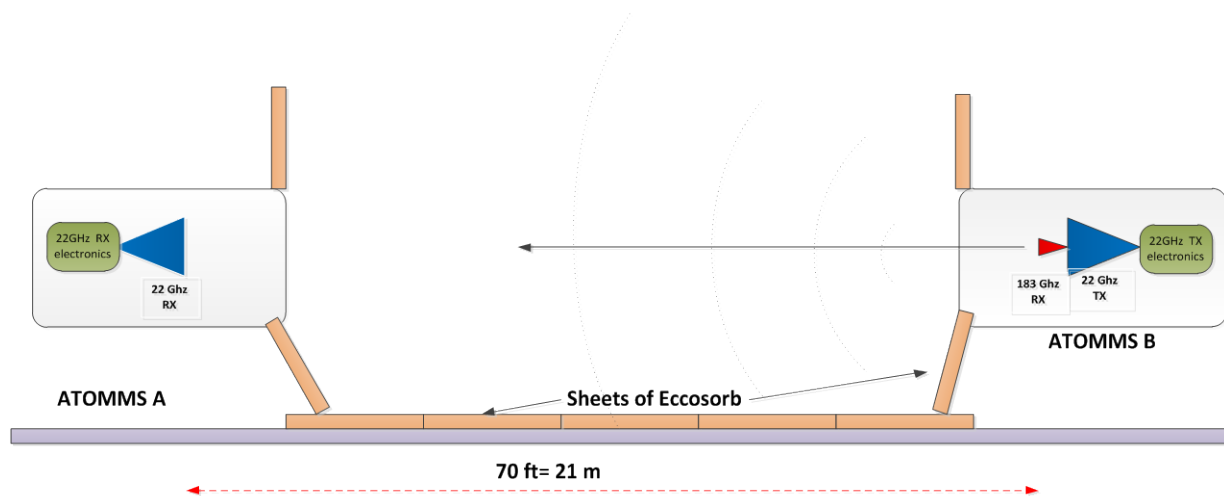
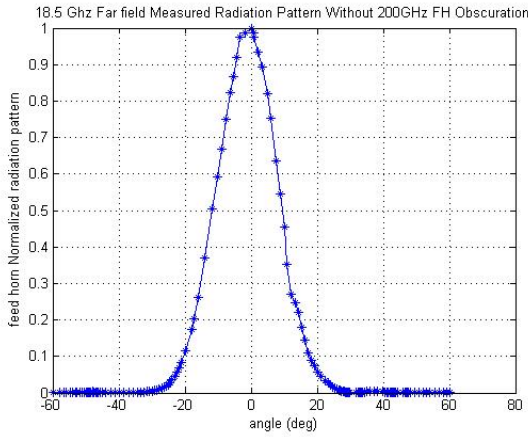


Figure V.2.1: The 22GHz Far-field beam pattern measurement with and without the 200GHz FH obscuration.

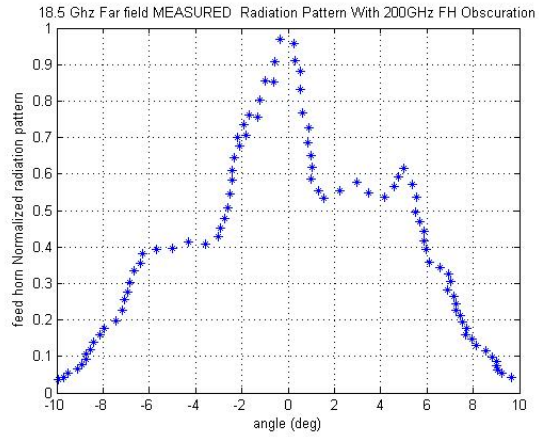
As we can see from Figure V.2.2 through V.2.4 comparing the measured beam pattern for the three frequencies with and without the 200GHz FH in place, all the beams show the diffraction effects in the center of the beam when the 200GHz FH was in place. On the other hand the beam pattern had a smooth transition without nulls in the center as expected from a Gaussian beam.

A. 18.5 Ghz

[MEASURED]



(a)
WITHOUT Obscuration

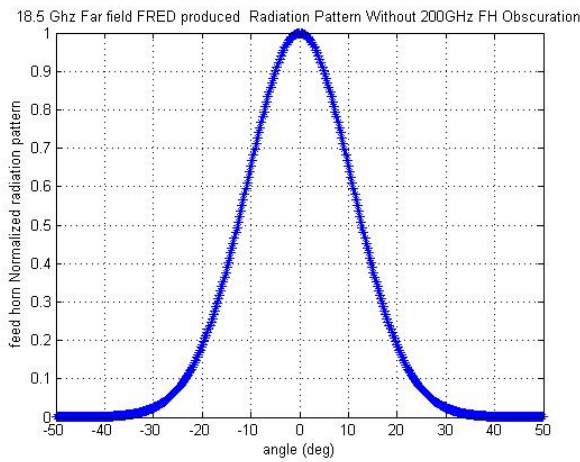


(b)
WITH obscuration

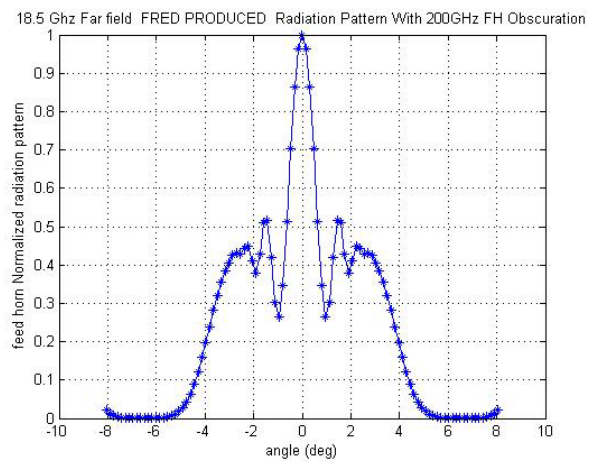
[FRED SIMUALTION]

WITHOUT Obscuration

With Obscuration



(c)
WITHOUT Obscuration

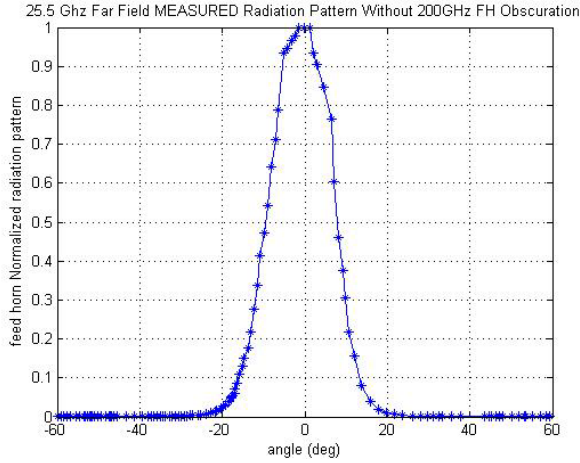


(d)
WITH obscuration

Figure V.2.2 Measured and simulated with and without obscuration results for 18.5 GHz

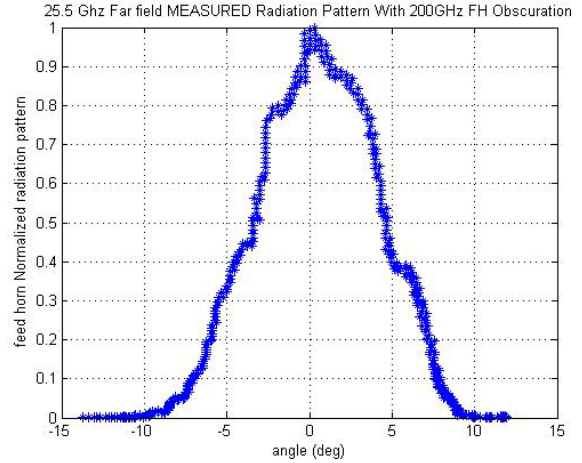
B. 25.5 Ghz

[Measured]



(a)

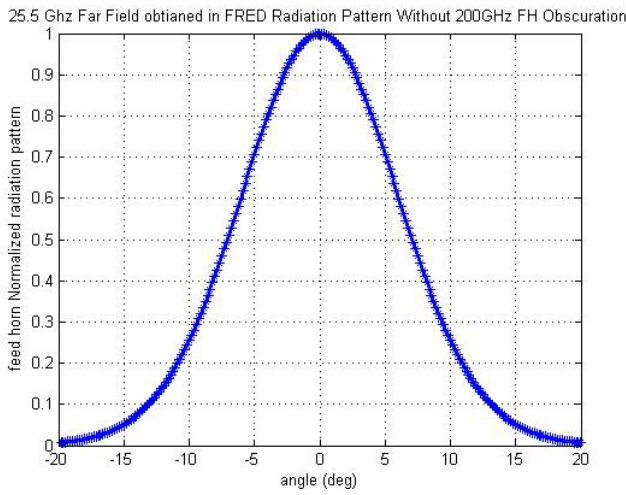
WITHOUT obscuration



(b)

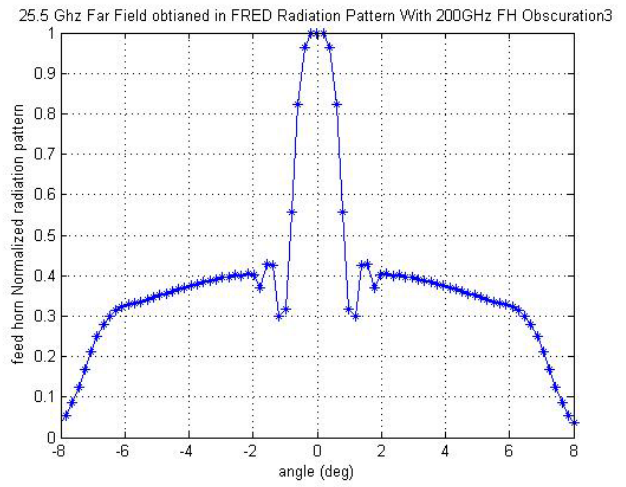
WITH obscuration

FRED SIMULATION



(c)

WITHOUT obscuration



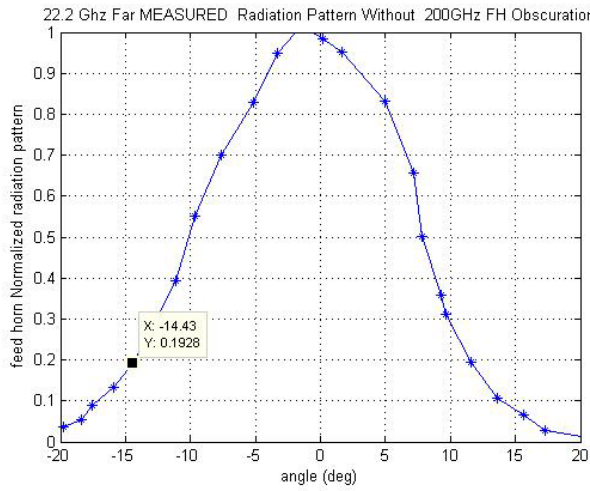
(d)

WITH obscuration

Figure V.2.3 Measured and simulated with and without obscuration results for 25.5 GHz

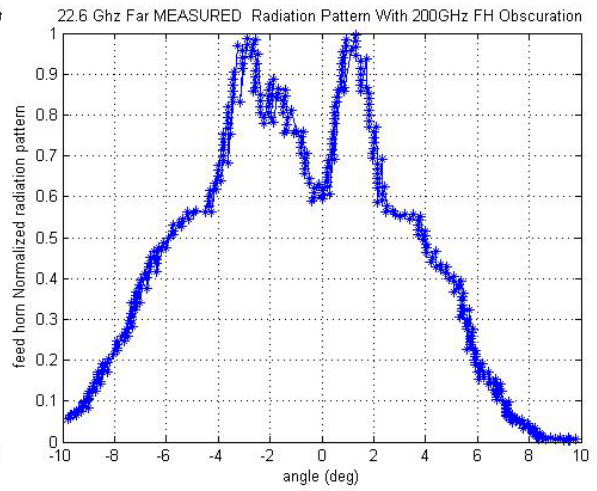
C. 22.2 Ghz

[Measured]



(a)

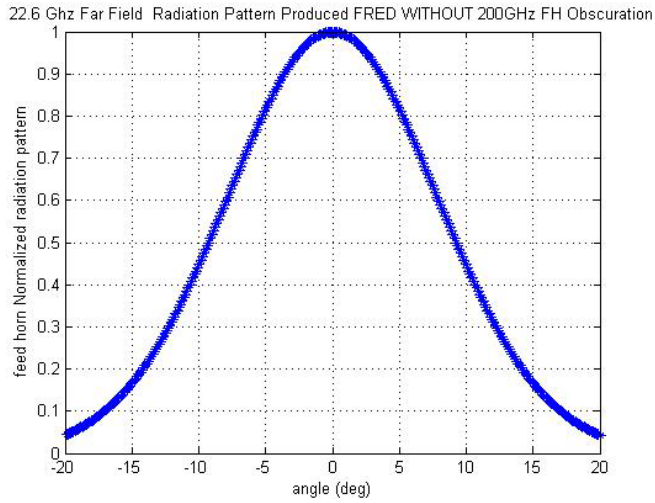
WITHOUT obscuration



(b)

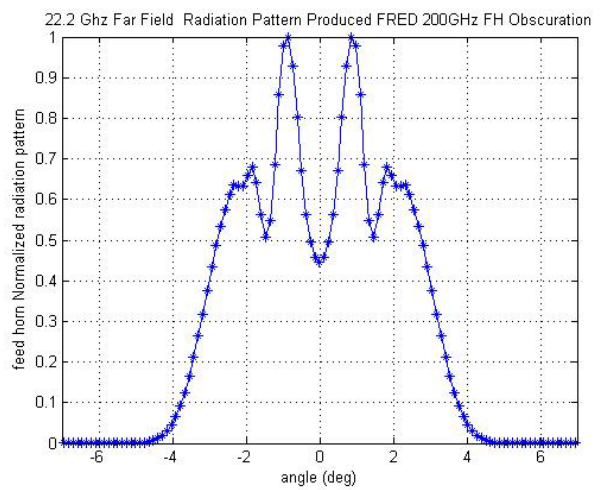
WITH obscuration

[FRED SIMULATION]



(c)

WITHOUT obscuration



(d)

WITH obscuration

Figure V.2.4 Measured and simulated with and without obscuration results for 22.2 GHz

A. Comparing the *measured* results with and without the Feed

1. The beam measured with the 200GHz FH all show larger widths which could be explained due to the other diffraction effect present due to the setup and the multi-reflection from surfaces that are not fully shielded with the Eccosorb absorptive sheets.
2. The entire beam shows some degree of tilt which is more likely due to the setup.

B. Comparing the *measured* and the *FRED simulated* with the Feed

FRED offers a unique capability in simulating diffraction problems by using the coherence property for sources and ray tracing. FRED uses a generalized form of Gaussian Beam Decomposition (GBD) to propagate coherent fields. The premise behind GBD, is that an arbitrary wavefront can be synthesized from a basis set of Gaussian beams that are propagated by raytracing. Conventional GBD methods limit the synthesis to one of two extreme conditions: **A.** A spatial decomposition using beamlets arranged on an evenly spaced grid, or **B.** A Fourier decomposition, based on the spatial frequency content, into beamlets at a single spatial position with different phases and directions [71], [72], [73], [74], [75], [76], [77], [78]. An extension of Arnaud's method, developed by Gabor [79] and implemented in FRED, allows these two methods to be utilized together in a flexible approach that is adaptable to a broader range of conditions.

With FRED, the optical field is represented by a superposition of Gaussian beamlets that are described and propagated using rays. A central "base" ray represents the trajectory of the beamlet and additional secondary "waist" and "divergence" rays track the evolution of the beamlet parameters. The relationship between a beamlet and its corresponding rays is shown in Figure V.2.5. The rays fully describe the beamlet characteristics as they undergo refraction, reflection, and diffraction. This process is referred to as "complex raytracing." At any plane in the system, the coherent field can be calculated by determining the contribution of each beamlet at each position

on the analysis surface and accounting for the phases.

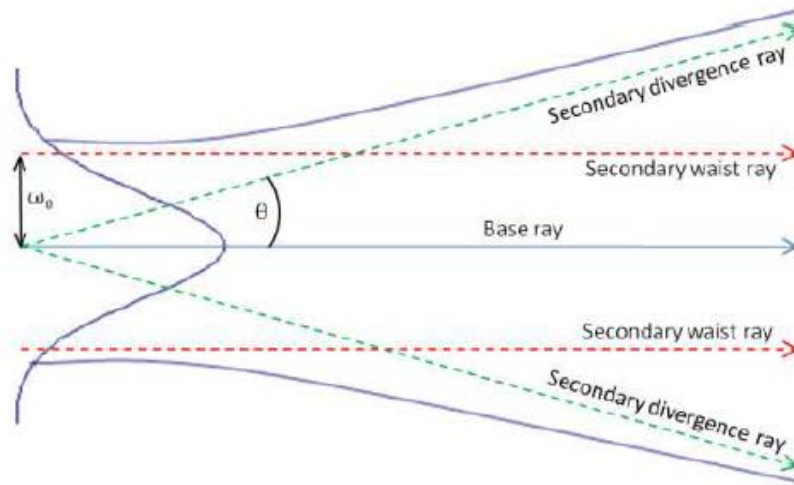


Figure V.2.5 Gaussian beamlet with corresponding rays

In order for the model to be accurate, the beamlets must remain Gaussian and perform best when they obey the paraxial approximation. This is perhaps the most important consideration in properly implementing coherent raytracing. Attempting to operate outside this paraxial limit negates the ability of Gaussian beamlets to accurately sample optical components as they propagate. Failure of secondary rays to remain well-correlated with their base ray may lead to coherent ray errors and erroneous irradiance calculations. Therefore we first evaluate the paraxial limit of this problem.

Plots (c) and (d) in each of the Figures from V.2.2 to V.2.4 shows the similarity of the diffraction features of the beam and it's behavior is very similar to the measured data with and without the 200Ghz feed. In order to further validate and confirm the diffraction problem it was determined to redo the analysis using the full forward diffraction propagation for Gaussian beam with an obscuration in place to obtain the resulting beam without making the paraxial approximation. The

following section will cover that portion of the analysis.

V.3 Diffraction analysis of the ATOMMS quasioptics system

The system design and the detailed elements of it are well covered in Chapter IV. Here we will develop a simplified model of the elements in the system. We will describe each element in the 22 GHz Transmitter part how they are modeled. Ideally we would have liked to model the FULL SYSTEM as shown in Figure V.3.1, however since measurement data for the beam pattern is not available it would be hard to compare the model. We will first model the system in the configuration similar to the tested one as shown in Figure V.3.1

1. The 22 GHz source FEED

The output from the 22GHz is a HE11 mode have a truncated circularly symmetric amplitude distribution represented by Eqn. (24) [80]

$$E_{ap} = J_0(2.405r/a) \exp(-j\pi r^2/R_h \lambda) \quad (24)$$

The J_0 Bessel function is what is found to be originally in the HE11 and EH11 modes and the spherical phase factor which is resulting from having a horn slant length of R_h . Generally speaking, it is safe to assume that the field distribution produced by feed horns and other feed systems can be easily and well represented by very few Gaussian beam modes or in some cases by only one mode, it depends on the type of feed. More complex analysis on the coupling performance between the feed modes and Gaussian field was been addressed [80]. In the following analysis we will use the single mode Gaussian beam radiating from the feedhorn expressed in Equation (25) below:

$$E(r, z) = E_0 \frac{w_0}{w(z)} \exp\left(\frac{-r^2}{w^2(z)}\right) \exp\left(-ikz - ik\frac{r^2}{2R(z)} + i\zeta(z)\right) \quad (25)$$

Where

$$w(z) = w_0 \sqrt{1 + \left(\frac{z}{z_R}\right)^2}$$

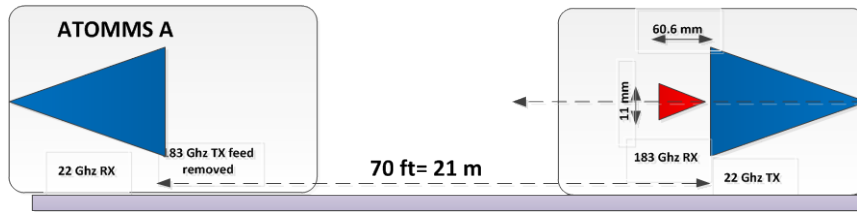
The list of the important Gaussian beam parameters are listed below for 22.6 GHz.

Parameter		[units]	
f	22.6	GHz	
λ	13.27	mm	
w_0	13.09	mm	Beam waist
a_22	30.5	mm	Radius of the 22GHz feed
W(z)	23.38	mm	beam radius at obscuration
k	0.471	1/mm	Propagation constant
zR	40.5	mm	Rayleigh distance
R(z)	87.5	mm	Radius of curvature at the obscuration

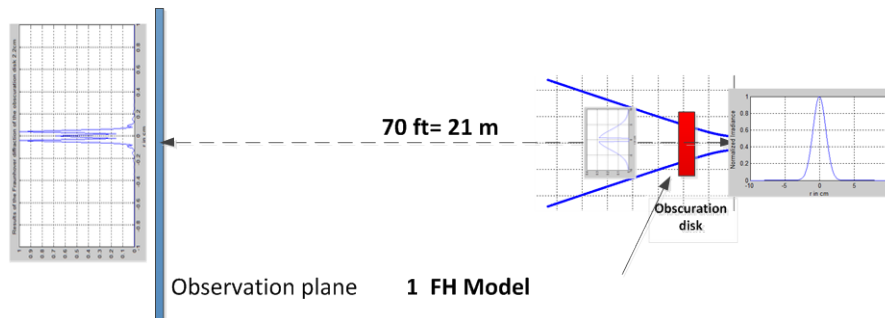
Table V.3.1: 22.6 GHz Gaussian beam parameters

2. 200 GHz FH Obscuration

For the purpose of this analysis the obscuration is simply represented by a the largest dimension disk that can represent the feedhorn aperture, is the cross section of the feedhorn seeing from the opening. The outer radius of the opening of the 200 GHz Feed horn is 5.5 mm. In the real design we have used absorbing material that is supposed to absorb the incident beams and reduce the reflected 22 Ghz beam back into the 22 GHz feedhorn in the receiver side and the opposite in the transmitter side. However we have not characterized the effectiveness of this material. So in this section we will ignore the present of the absorber and will model the 3D FH as a just a circular obscuration disk with a radius =5.5 mm. As we have mentioned earlier we are ignoring the volumetric diffraction effect of the cone shaped like FH and its reflective surface and the scattering of the edges. Figure V.6 shows a cartoon representing the model and the test configuration.



(a) Test Configuration



(b) Model

Figure V.3.1 Model and test configuration

Figure 4 shows the profile of the 22 GHz output Gaussian beam from the FH (its input to the system).

$$u(r,0) = u(0,0) w_0/w(z) \cdot \exp(-r^2/w_0^2) \quad (26)$$

Which can be represented as $U_{inc}(r,0)$ plane wave = $\exp(-ikz)$ @ $z=0$ incident on an amplitude aperture

$$t_{ap1} = \exp(-r^2/w_0^2) \quad u(r,0) = U_{inc}(r,0) \cdot t_{ap1}(r_0) = u(0,0) \exp(-r^2/w_0^2) = u(0,0) \exp(-r^2/r_0^2) \quad (27)$$

Let $u(0,0) = 1$

Figure V.3.2 shows the obtained normalized field, phase and normalized Irradiance without any obscuration. As expected the Gaussian beam radius become larger and the radius of curvature grows larger as well to become close to a plane wave.

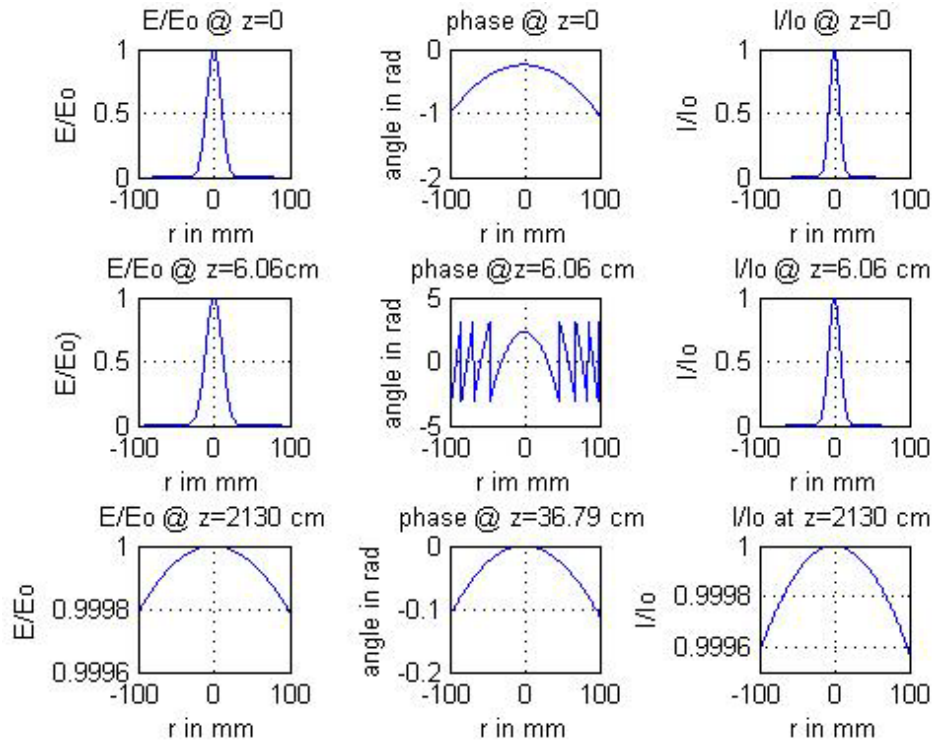


Figure V.3.2 The normalized fields and phase at the 200GHz feed and at the 22 GHz RX (2130 cm away)

The 200 GHz corrugated conic shape Feedhorn is modeled here as a circular disk with thickness = 0, with the diameter of the aperture of the feedhorn = 1.1 cm as shown in Figure V.3.3. We can represent this obscuration using babinet's principle. Figure V.3.3 shows the configuration, the shaded area is considered opaque and the solid white area is considered transparent. Therefore

$$u(r, z_1) \text{ after the disk} = u(r, z_1) \text{ before the disk} \times t(x, y)_{\text{disk}} \quad (28)$$

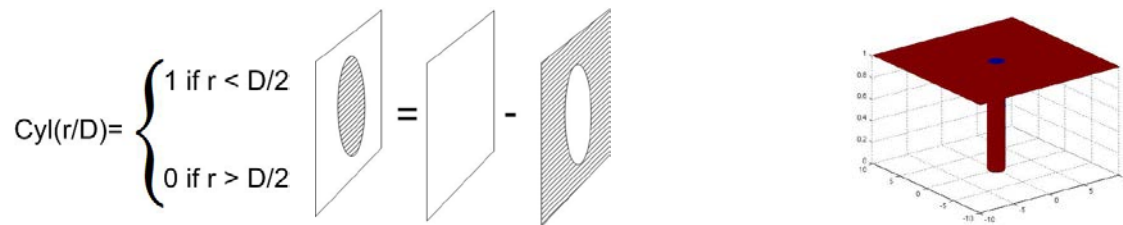
Applying Babinet principle we can write $t(x,y)_{\text{disk}}$ as

$$t(x,y)_{\text{disk}} = [1 - t_{\text{ap}}(r/D)] \tag{29}$$

where $t_{\text{ap}}(r/D) = \text{cyl}(r/D)$ which is an open aperture.

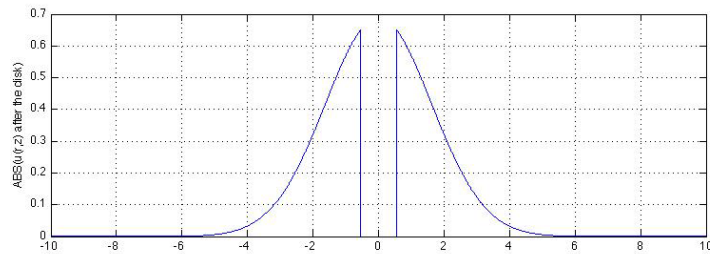
$$u(r,z)_{\text{after the disk}} = r_0/w(z_1) \cdot \exp(-r^2/r_0^2) \exp(-ikz_1) \exp(-ikr^2/R(z_1)) \times [1 - \text{cyl}(r/D)] \tag{30}$$

Where $D =$ diameter of the disk $= 1.1 \text{ cm}$ $\text{cyl}(r/D)$ is defined as

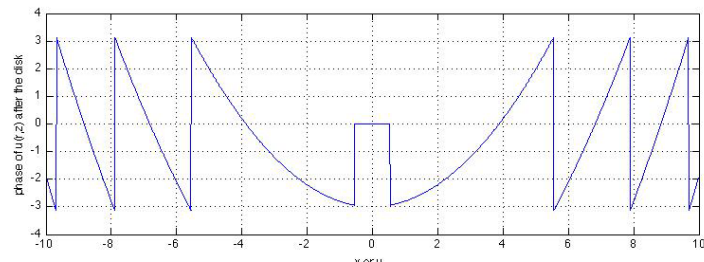


(a) The application of Babinet principle (b) The 2D representation of the disk

Figure V.3.3 Babinet principle



(a)



(b)

Figure V.3.4 $u(r,z)$ After the disk (a) Amplitude (b) Phase

Figure V 3.4 shows the resulting $u(r,z_1)$ after the disk (a) Amplitude and (b) phase. The multiplication of the field with the disk is done below using 1D since the system is symmetric. The resulting field in Eq (30) at the surface of the disk has lost its main lobe over a distance of $r \sim 0.55$ cm but is still axially symmetric which is expected. For this section we are interested in finding the field distribution at the receiver end which is 2130 m away from the 22 GHz Tx.

Rayleigh Sommer field diffraction integral is give below:

$$u(r,z) = (-1/2\pi) \int d^2 r_o U_{inc}(r,0) \cdot t_{ap1}(r_o) [ik - 1/R] \cos(\theta) \exp(ikR)/R \quad (31)$$

$$u(r,z) = (-1/2\pi) \int d^2 r_o u(r,z_1)_{after\ the\ disk} [ik - 1/R] \cos(\theta) \exp(ikR)/R \quad (32)$$

Where $R = \sqrt{|r-r_o|^2 + (z-z_o)^2}$, $z_1=0$ is at the disk,

$$\cos(\theta) = z / \sqrt{|r-r_o|^2 + z^2}$$

In this case we simply apply the Fraunhofer approximation since

$$Z_{fraunh} = 2130\text{cm} \gg (D/2)^2/\lambda = 14\text{ cm}$$

Effectively this approximation makes the exponential term in the Fraunhofer diffraction integral $\exp(j\pi r_o^2/\lambda z_{to\ lens})$ to go to 1.

The integral in eq (9) becomes simply a Fourier transform of the $u(r,z_1)$ after the disk. The results are carried out in Matlab and shown in Figure V.3.5.

If we compare all the results shown in Figure V.2.2 (b) measured V3.4 (d) simulated with FRED and V10.(c) we can easily see correlation between the figures:

1. All exhibits the two peaks on the side of the center/peak or null

2. The measurements shows broader pattern and that is can easily be explained that the during the measurements the beams suffered more diffraction effects that were not modelled in neither the matlab not the FRED; diffraction from the metal housing, the 30 cm open aperture in both instrument, the multipath effects.

3. In order to better model this geometry we MUSY refer to Volumetric diffraction theory since the obscuration is a 3D element that were not captured accurately in FRED nor in the maltab.

4. The diffraction effects from the 22 GHz FH is not accounted for

5. The more proper way of modeling this geometry is to use volumetric diffraction theory because scattering in both models (FRED and Matlab) has been fully not accounted for

However, the main goal for this section was to establish the root cause of the distortion seen in 22 GHz received beams during the field test. In the next section we will focus bring new design concepts in order to restore the functionality of the ATOMMS instrument.

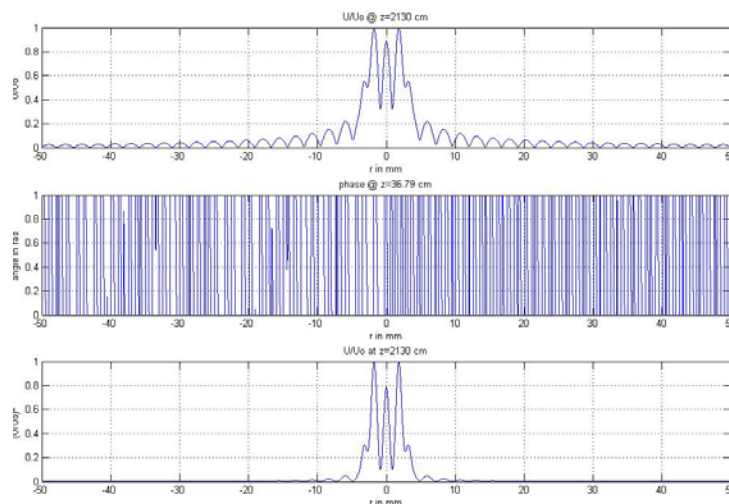


Figure V3.5: The Fraunhofer diffraction pattern seen at the 22GHz feedhorn 2130 cm away from the TX with the obscuration in place for $f=22.6$ GHz

V.4 New Quasi Optics Design Concepts

We have identified 3 design concepts to fix the problem in the original ATOMMS optics design MARK”T” caused by the blockage of the 22 GHz horn by the 183 GHz horn. The description of each design their pros and cons are summarized in Table V.4.1 below.

In this chapter we will discuss the details of the design III since it was selected to be the most feasible and practical given the very tight instrument development schedule. Some of the details of the other designs will be covered in APPENDIX B.

DESIGN	Advantages	Disadvantages
DESIGN I SINGLE LENS 30 cm + dichroic, beam splitter+ elliptical reflector	Uses existing lens Existing 183 GHz horn in current mount Existing 22 GHz horn	Requires dichroic, Dichroic design for circular polarization @ 22 Dichroic mount elliptical reflector elliptical mount new mount for 22 GHz horn Prone to unwanted diffraction effects which cause more amplitude instability Need custom Dichroic to operate in CP light Otherwise is limited by linear polarized light Possible more distortion
DESIGN II SINGLE LENS 30 cm + dichroic, beam splitter	Uses existing lens Existing 183 GHz horn in current mount No elliptical reflector Lighter than (I)	Modify 22 GHz horn ... It fits with small tolerance Prone to unwanted diffraction effects which cause more amplitude instability Need custom Dichroic to operate in CP light Otherwise is limited by linear polarized light Possible more distortion
DESIGN III. 2 lenses one for each band	No dichroic No elliptical reflector Less mass in 2 lenses ($\sim 1/3$ of present mass = $[2/3]^3 + [1/3]^3 = 1/3$, 4 lb savings) Shorter design (10 cm shorter using	Lower SNR _v by $\sim 4/9$ at both 22 and 183 Requires 2 new lenses Mounting for the new lenses Alignment of two optical systems May increase mass?

	current horns & each lens 2/3 of original) May lower mass overall Less Fabry Perot effect because lens surface is not parallel to nose skin 50% wider beams a bit easier to point	
--	--	--

Table V.4.1 A summary of the pros and cons for each design

V.5 Design III 2Lenses approach

The basic configuration of this concept is shown in Figure V.5.1. In this design we each feedhorn will be illuminating its perspective lens in the TX mode and will be receiving the focused received beams from their perspective lenses in the RX mode. From the ATOMMS development stand point the design eliminates many high risks items such as the needs for developing 2 new more quaioptics elements the elliptical mirror and the dichroic beam splitter. However, choosing design I and or II for the ATOMMS space/satellite version might be worth exploring. For the ground experiments tilt tip mechanical adjustments for and translation in Z will be added to optimize the pointing for each system, and Z-axis translation will help optimize the lens/antenna illumination which results in the Gain optimization. The choice for the lens material was still to be HDPE where the losses are much smaller in comparison to Rexolite. The losses for HDPE in these frequencies were measured earlier and reported in Chapter IV. Since the width of the instrument is limited to only 30 cm, a 20 cm lens will be used for 22 GHz and a 10 cm lens will be used for the 200 GHz system.

In the next section we will cover the detailed design for the 22 GHz system, a similar approach will be used for the 200 GHz however it will not be carried out in this chapter. Its very unfortunate that the ATOMMS project development was discontinued where the opportunity to qualify the designed lenses was not available. Therefore throughout the scope of this work the beam profile

measurement for newly designed lenses will not be covered, however future development of the ATOMMS optics system will include the lens test data and coupled with analysis.

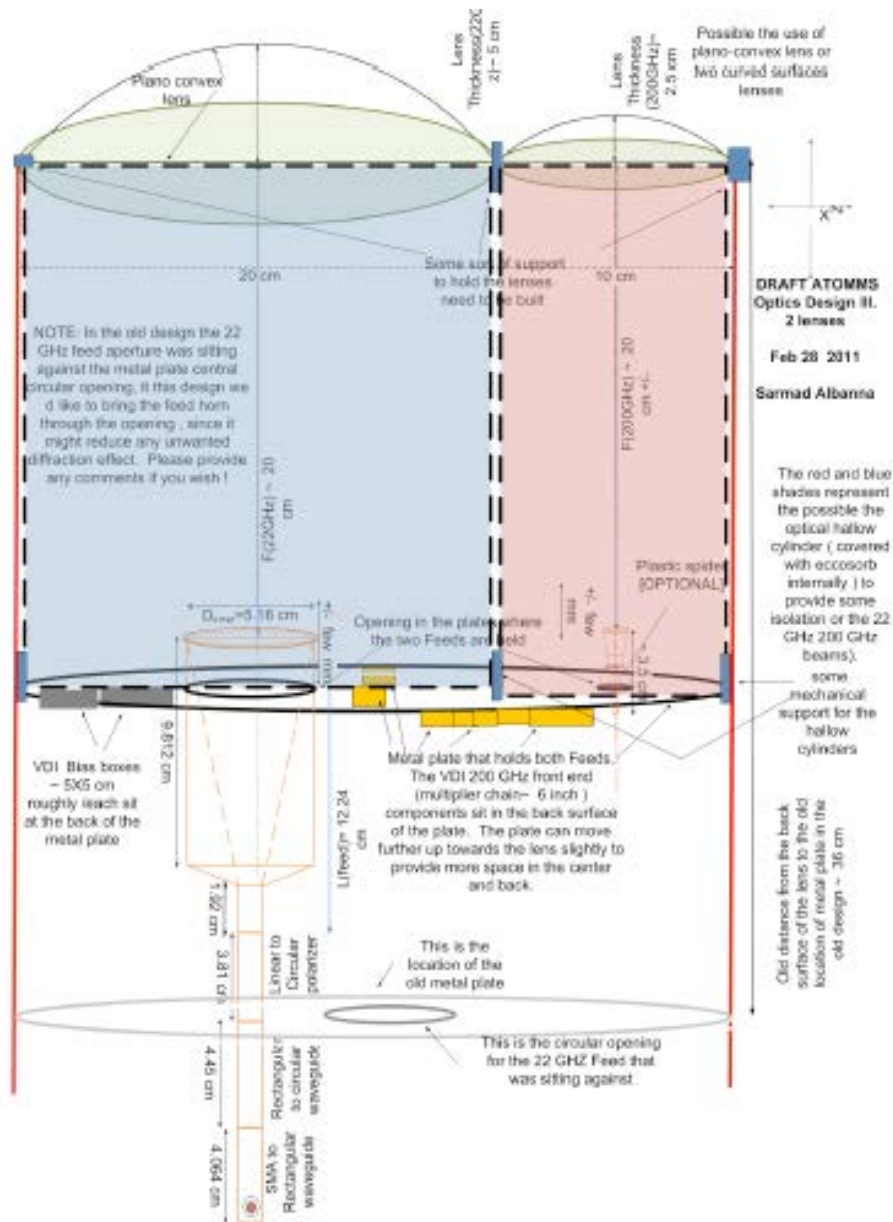


Figure V.5.1 Design III Dual Lenses basic configuration showing each feedhorn illuminating their perspective lens

V.5.1 Deriving the new optics design requirements from the ATOMMS System performance requirements.

I. ATOMMS Performance requirements

The instrument has two performance requirements one that is needed for the final aircraft-aircraft demonstration and one for the Mountain top testing which is hardly close to the tighter requirements for the real Aircraft- Aircraft experiments. Yet, for the Mountain top optics design, we are incorporating as many requirements as possible from the aircraft experiment into the mountain top experiment such that it can be easily optimized for the performance for the Aircraft experiment. So all the listed requirements below are based on the aircraft experiments

1. Water Vapor (WV) error

With ATOMMS the goal is to detect WV error to levels of <1%, 0.1% is an ultimate goal, therefore the error in amplitude variations should be <0.2%.

2. SNR For large separation distances ~1000 km SNR should be high which means antenna gains should also be high. An estimated value is:

For distances $L=984\text{km}$ between the TX and RX and $f= 22\text{GHz}$, therefore Gain need to be > 32.14 dB [based on Antenna efficiency $\epsilon =0.55$ (arbitrary)], $D= 20\text{ cm}$ $\lambda= 1.3274\text{cm}$] Please visit APPENDIX A for the path loss analysis.

Higher Gain indicates the need for higher D and /or high ϵ

3. Pointing Error With ATOMMS we will have a Gimbel pointing error (combined for both Gimbals)~ +/-0.5 deg will further increase the amplitude variation in the following matter:

Due to dispersion in the TX and in the RX quasioptic systems the beam pattern shape will be impacted due to two components: The second is the dispersive components of the lens material however the impact of that has not been included in this analysis. The first part which is more significant is due to difference in antenna/lens illumination resulting from having different tones transmitted from the 22 GHz feedhorn. Each will illuminate the lens slightly differently at the TX, and will produce different Airy pattern at the RX. Yet, the effect is large enough such the resulting beam patterns will exhibit variations versus angle due to different λ . those variations will not be factored out while ratioing the measured intensities I_1/I_2 for angles > 0.1 deg derived in [26] CHAPTER 1]. This source of pointing error will add more error in WV.

In order to estimate the error in WV we plotted the Airy disk pattern for the received beam for the two band center frequencies 22.6 GHz and the largest frequency in the band 25.5 GHz and 186GHz in the 200GHZ band frequency for the for the 30 cm diameter lens diameter, we ratioed the amplitudes for each case and plotted them with respect to the pointing error. Figures V.5.1 through V.5.4 show all those plots.

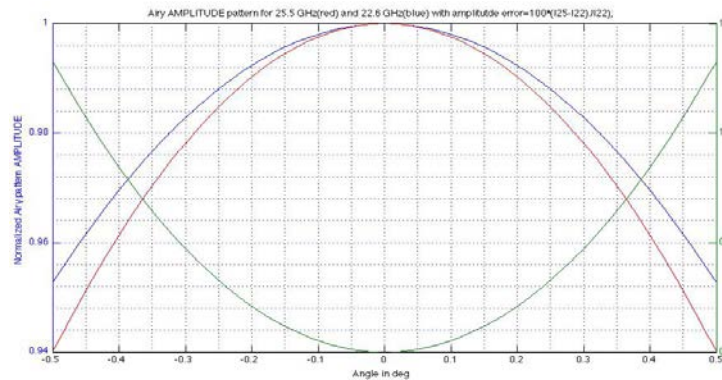


Figure V.5.1: Normalized gain at 18.5, 22.6 & 25.5 GHz and residual amplitude error in % when the ratio of the received amplitudes is formed for lens diameter of $D_{\text{lens}}=30$ cm. Maximum amplitude error $\sim 0.3\%$ at 0.25 deg pointing error



Figure V.5.2: Normalized gain at 183 & 186 GHz and residual amplitude error in % when the ratio of the received amplitudes is formed for lens diameter of $D_{\text{lens}}=30$ cm (only 15 cm of the diameter is illuminated) Maximum amplitude error $\sim 0.8\%$ at 0.25 deg pointing error.

Next we plot the same plots but using a 10 cm antenna diameter for the proposed 200GHz band and 20 cm antenna diameter for the 22GHz feed and compare the results with the 15 cm and 30 cm cases respectively.

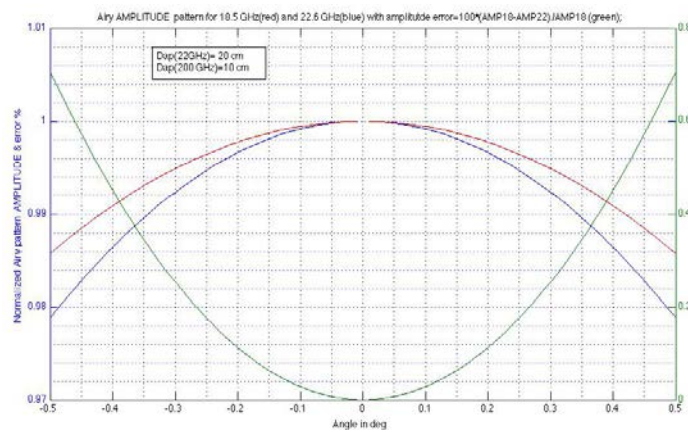


Figure V.5.3: $D=20$ cm: At 0.25 degree pointing error causes $<0.2\%$ differential amplitude error between 18.5 and 22.6 GHz



Figure V.5.4: .Normalized gain at 183 & 186 GHz and residual amplitude error of 0.3% at 0.25deg when the ratio of the received amplitudes is formed for lens diameters of 10 cm

The last four plots are combined in two next plots Figure V.5.6 and Figure 5.7 to show the difference in WV error when we choose smaller diameter antennas.

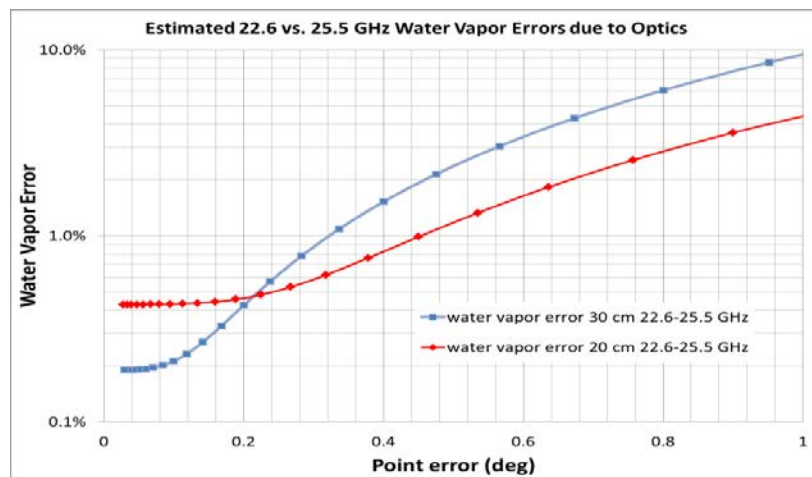


Figure V.5.5 Water vapor & pointing errors for different antenna sizes for 22 GHz

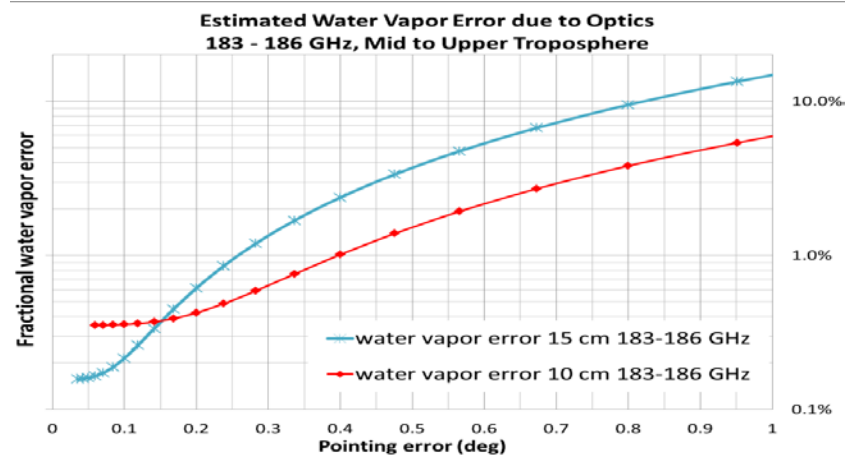


Figure V.5.6; Water vapor & pointing errors for different antenna sizes for 183 GHz

Therefore from the above we can conclude the effects of the Optics redesign on the instruments performance:

As D increases the Antenna gain G_{ant} increases and SNR_{power} increase leading to higher $SNR_{voltage}$, but that leads to smaller λ/D which means a narrower beam that leads to more sensitive to pointing, i.e. pointing error increases.

Based on the derived total fractional mean square error $\frac{\langle \epsilon^2 \tau_{12}^2 \rangle}{\tau_{12}^2}$ from [26]

Where τ_{12} the optical depth difference = $\tau_1 \cdot \tau_2$, and $\langle \epsilon^2 \tau_{12}^2 \rangle$ is the expected value of the error, we can estimate the total error assuming the following parameter: Altitude of 7 km, P= 400 mb, pressure broadening is at 3Mhz/mb~ Linewidth of 1.2 GHz, for 6 dB down from peak ~ 3 GHz of frequency spacing between tones; with the above we get the following impact on the two systems:

A. 22 GHz

22 GHz transmit power: 12.5 mW (=100 mW/8)

Aircraft separation (22.6 GHz) = 985 km

$$D_{\text{lens}} = 30 \text{ cm} \quad \text{SNR}_{v0}(22.6 \text{ GHz}) = 5400, \text{ SNR}_{v0}(25.5 \text{ GHz}) = 6085$$

$$D_{\text{lens}} = 20 \text{ cm} \quad \text{SNR}_{v0}(22.6 \text{ GHz}) = 2400, \text{ SNR}_{v0}(25.5 \text{ GHz}) = 2700$$

$$\text{Tau}(22.6 \text{ GHz}) = 2, \text{ tau}(25.5 \text{ GHz}) = 0.4$$

Amplification factor from fractional optical depth error to fractional water vapor error: 3.5

B. 183 GHz

183 GHz transmit power: 5 mW

Aircraft separation (183 GHz) = 783 km (mid-troposphere)

$$D_{\text{lens}} = 15 \text{ cm} \quad \text{SNR}_{v0}(183 \text{ GHz}) = 4555, \text{ SNR}_{v0}(186 \text{ GHz}) = 4630$$

$$D_{\text{lens}} = 10 \text{ cm} \quad \text{SNR}_{v0}(183 \text{ GHz}) = 2025, \text{ SNR}_{v0}(186 \text{ GHz}) = 2058$$

$$\text{Tau}(183 \text{ GHz}) = 2, \text{ tau}(186 \text{ GHz}) = 0.4$$

Amplification factor from fractional optical depth error to fractional water vapor error: 2.3

[26]

4. Mechanical constrains:

With 30 cm maximum allowable width choosing 2 lens antennas with $D_1=20$ cm and $D_2=10$ cm is possible. The proposed layout is shown in Figure V.5.1

V.6. 22 GHz 20 cm lens design

Given the following initial parameter: Lens Size: Maximum size $D=20$ cm using the existing feed horns for TX and RX, with the following parameters

1. $D=5.1$ cm, $a= 2.55$ cm

2. $R_h = 12.42$ cm

3. $H = 12.11$ cm

4. $\Theta_{\text{feed_FWHM}}$ 20 deg (E- field) 20.5 deg (H- field) at $f = 22.6$ GHz

$\Theta_{0(1/e)} H_w$ (rad) = $16.95 \cdot \pi / 180 = 0.295$ rad .

A. Design Assumptions

- Paraxial approximation later one we should calculate its produced error.
- Starting with a simple thin lens
- The RX and the TX will have the same lens specs.
- The profile of the field at the feed aperture is:

$$E_{ap} = J_0(2.405 r/a) \exp(-j \pi r^2 / (\lambda R_h)) \quad (1)$$

Which is approximated using a the fundamental Gaussian beam mode [80 Ch 5]

Where $a = 2.55$ cm of the current feed $R_h = 12.42$ cm slant length of the feed

- All the power coupling calculations were based on a linear polarized field [80 ch 7] and a for more accurate design, a more accurate formalism to describe the exact conditions that will allow us to determine maximum field coupling for the multimode Gaussian beam structure that is circularly polarized since we are using a circular polarizer at the input of the feedhorn.

B. Design Philosophy

In the older design “MARK I” we used the illumination of the TX lens as our basis for finding the rest of the design variables, and the RX lens was chosen to be similar to the TX lens. In this design we will design each lens independently based on their perspective system requirements such that

lens is optimized for each side independently. Therefore we have to parts to this section the TX lens and the RX lens:

V.6.1 22 GHZ TX

The goal is to find some of the X Gaussian parameters, and approximate focal length value, such that the output beam is collimated with maximum power coupling from the already designed 22 GHz feed horn. The radius of curvature and thickness will be obtained using the zemax design software.

V.6.1.1 Design Criteria TX

- Maximum power coupling from the FH (minimum spillover)
- Smallest change in OPL versus dX and dY.
- Semi radius of 100 mm
- Smallest thickness possible (to reduced dielectric losses)
- Two curved surfaces to minimize reflections back to the Feed and to reduce possible standing waves between the TX and RX
- A suitable beam coupling from the TX feed horn to the lens antenna to give a gain of > 32 dB
- Minimize losses due to diffraction at the aperture and defocus
- Keep the output beam from growing to an excessive dimension which puts some restriction on the focal length
- Optimum output beam waist $w_{O_{out}}$ size such that its location is not sensitive to the input beam waist.
- Minimize the losses due to defocus due to the frequencies that are in edge of the 22 GHz band.

- High Aperture efficiency (high T_e and low Spill over) such that the resulting gain is still $> =30$ dB, and the same time keeping the output divergence high enough such that resulting system pointing error is minimized and yet small enough to minimize multipath interference.

STEP I: Optimum beam antenna illumination

First we would like to list some of the already know Gaussian beam parameters and the important mechanical specifications of the already selected feedhorn, those are listed in Table V. 3: the bolded quantities are the calculated values from the measured or give values.

Parameter		[units]	
F_c	22.6	GHz	
λ	13.27	mm	
ϕ_{div}	0.1745	rad	
a	25.5	mm	Radius of the 22GHz feed
R_h	124.2	mm	Slant length
H	121.5	mm	Horn Length
w_0	14.3	mm	$w_0 = \lambda / (\pi * \phi_{div})$
Z_c	48.25	mm	$Z_r = \pi w_0^2 / \lambda$

Table V.6.1: Gaussian beam parameters and feedhorn mechanical quantities

The aperture illumination produced by a Gaussian feed distribution is described by the edge taper (As discussed in Chapter IV) and rewritten below

$$T_e \text{ (dB)} = [\phi_{div} \text{ (in rad)} / (\lambda/D) - 1.02] / 0.0135 \quad (10)$$

Which describes the truncation of the Gaussian beam that has a divergence angle at the aperture that has a diameter D and radius of $a = D/2$ and the quantity α represents the ratio of the radius of the aperture to the beam radius at the aperture.

$$\alpha = 0.115 T_e \text{ (dB)} = (r_a/w_a)^2 \quad (33)$$

The above formulas are useful for determining the power coupling efficiency $|co|^2$ for the aperture illumination which is also the antenna efficiency ϵ_a [80 pp. 130].

$$\epsilon_a = |co|^2 \quad (34)$$

ϵ_a is important in defining the Gain of the antenna as shown below:

$$G_{ant}[\text{dB}] = 20 \log(\epsilon_a (\pi D_{lens} / \lambda)) \quad (35)$$

Where D_{lens} is the diameter of the lens antenna

Since we are interested in maximum Gain, the only variable we can control is antenna efficiency

ϵ_a . ϵ_a is related to the α for non-blocked beam propagation as below [GOLDSMITH pp. 130]

which is plotted in Figure V.6.1

$$\epsilon_a = 2 \alpha^{-1} [1 - \exp(-\alpha)]^2$$

(36)

We can see that maximum ϵ_a is achieved if $\alpha = 1.27$ which give us another Gaussian beam

parameter $w_a(z)$ the radius at the aperture of 7.87 cm for $a = 10$ cm.

The calculated G_{ant} is 32.6 dB.

We choose the illumination that is characterized by $\alpha = (r_a/w_a)^2$ & T_e such that:

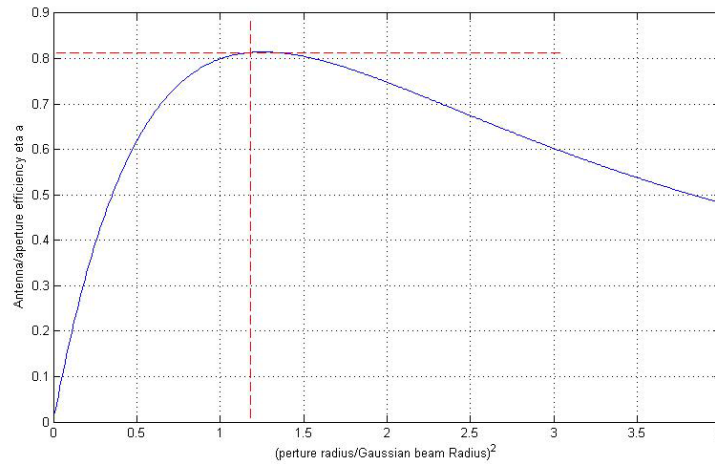


Figure V.6.1 The relationship between the antenna efficiency η_a and the quantity $\alpha (ra/wa)^2$

As we have stated earlier that the field radiating from a corrugated feedhorn is represented as a Bessel function of the first kind with a spherical wavefront as shown in eq (1), where the center the center of the radius of curvature of these spherical wavefront is located inside the feedhorn. This is due to the fact that the feedhorn walls are made from highly conductive material where the E-field lines are perpendicular to the feedhorn boundaries. Figure V.6.2 shows the geometry of the Feedhorn and the equiphase surfaces at the aperture

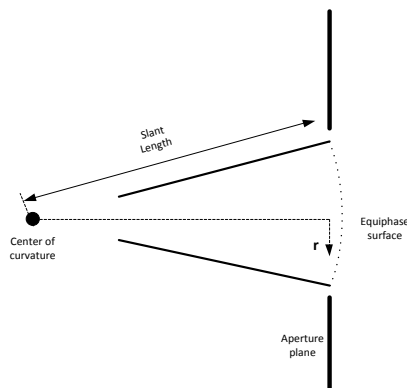


Figure V.6.2 Schematic of the feedhorn illustrating the spherical equiphase surfaces at the aperture

At $R(z) = R_h$ the phase distribution at the aperture of the feedhorn is

$$\Phi_{ap} = -\pi r^2 / \lambda R_h \quad (37)$$

The analysis of the aperture field is most reasonably carried out in terms of the axisymmetric Gauss-Laguerre beam modes. Since each mode will have the same spherical wave of radius of curvature of R , and since the expansion involves modes that all have the same beam radius, it is reasonable to adapt the strategy to choose the radius of curvature of each Gaussian beam mode to match that of the feedhorn at the aperture plane.

That means At the Aperture of the feedhorn we have:

$$R_h = R(z)_{\text{feedhorn}} = R_{22} = z \left(1 + \left[\pi w_o^2 / (\lambda z) \right]^2 \right) \quad (38)$$

Since $R(z)$ for the Gaussian beam is defined from the beam waist w_o , then z here represent the distance from the beam waist plane to the feedhorn aperture plane. We can solve for z from the above equation

$$z = R(z) / 2 \left[1 \pm \left[1 - (2\pi w_o^2 / (\lambda z))^2 \right]^{0.5} \right] \quad (39)$$

$z = 2.3$ cm. This is what is called the phase center Δ_{pc} described earlier in Chapter IV.

Now we would like to find the distance z_l from the back surface of the lens to the plane of the beam waist w_o , we can achieve that by solving for z from the below Gaussian equations

$$w(z)^2 = w_o^2 \left[1 + (z_l / z_c)^2 \right] \quad (40)$$

$$z_c = \pi w_o^2 / \lambda \quad (41)$$

Therefore:

$$z_L = \pi w_o / \lambda [w^2(z) - w_o^2]^{0.5} \quad (42)$$

having $w(z) = 7.87 \text{ cm}$, z_L become = 26.155 cm

Therefore the optimum distance from the back surface of the lens to the Feedhorn aperture is 26.155-2.3 cm= 23.85 cm. That will give us the highest antenna efficiency of 0.812 and a maximum gain of 32.6 dB. However, since the designed lens will have some nominal thickness (unknown at this point) especially that both surfaces would be curved surfaces we anticipate that the actual distance from back surface of the lens to the feedhorn aperture will be few cm less ~ 3 cm. We will choose $f=21$ cm for the TX side. In the new instrument design the mechanical design will allow adjustment in Z and in tilt and tip in order to maximize the performance of the antenna gain and the alignment.

STEP II. Calculating the output beam parameters

As we have mentioned before in the design criteria, the beam needs to expand slowly and at the same time the location of the output beam waist $w_{o_{out}}$ is not sensitive to the input beam waist. Since the feedhorn will emit frequencies from 18.5 GHz to 25.5 GHz, the input beam waist size to the antenna will vary accordingly. The relationship between input and output beam parameters of the Gaussian beam propagating through a lens with the ABCD matrix representation (we are considering the thin lens) have been well derived in the literature [80 Ch 3]. Here we will list few of those equations to help us optimize the design. Referring to Figure V.6.3 The input and output beam parameters can be described in the below:

$$d_{out}/f = 1 + (d_{in}/f - 1) / [(d_{in}/f - 1)^2 + z_c^2/f^2] \quad (43)$$

Figure V.6.3: Gaussian beam, transformation by a quasioptical system characterized by its ABCD matrix.

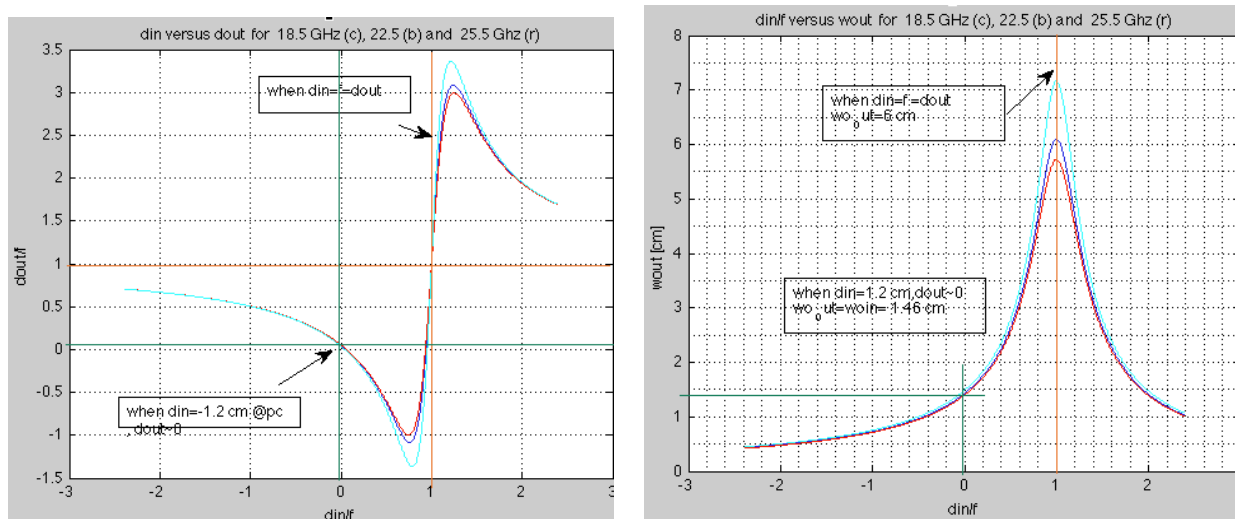


Figure V.6.4 (a) shows the d_{out}/f versus d_{in}/f (b) shows w_{out} versus d_{in}/f for 18.5, 22.6 and 25.5 GHz

Examining the above equations we can obtain the following useful observations:

1. Since we would like to have the out beam diverge slowly, that indicates $z_{c out}$ should be selected to be maximum, which leads to select w_{out} to be maximized, for a fixed w_{in} the System magnification η should be at maximum. The above condition can be achieved if we choose $d_{in} = f$ which leads to have $d_{out} = f$ and $\eta_{max} = f / z_{cin}$
2. With the same condition above, we can achieve another advantages: Since the feedhorn will produce different w_{in} for different λ , the relative position of those w_{in} will vary slightly which leads to change in d_{in} as a function of λ , setting $d_{in} = f$ will force the condition for which the output distance d_{out} is independent of w_{in} which makes not dependent on λ as also shown in Figure V.6.4 (a) where and in (b) where $\eta = \eta_{max}$.

$$W_{out}(f= d_{out})= \lambda f/(\pi w_{in}) \quad (45)$$

With the above condition the final design results for the TX antenna

f	2.26E+10	1.85E+10	2.55E+10	[unit]
λ	1.3	1.6	1.2	[cm]
f	21.0	21.0	21.0	[cm]
d_{in}	21.0	21.0	21.0	[cm]
d_{out}	21.0	21.0	21.0	[cm]
η	4.4	5.2	5.2	
w_{in}	1.428	1.4	1.2	[cm]
$W_{out}(f= d_{out})$	6.2	7.5	6.4	[cm]
$z_{c in}$	4.8	4.8	4.8	[cm]
$z_{c out}$	91.4	4.0	4.0	[cm]
G_{ant}	31.3	29.7	31.4	[dB]
$w(z)=wa$	7.5	7.7	6.5	[cm]
α	1.8	1.7	2.3	
ϵa	0.8	0.8	0.7	
$R(z)\sim f$	22.1	21.7	22.1	[cm]

Table V.6.2 22 Ghz Gaussian Beam parameters

V.6.2 22 GHz RX

V.6.2.1 Design Criteria for the 22 GHz RX

- Semi radius of 100 mm
- Smallest thickness possible (to reduced dielectric losses)

- Two curved surfaces to minimize reflections back to the Feed and to reduce possible standing waves between the TX and RX
- minimum enlargement or smearing of the image spot due to off axis beams (reduced pointing error)
- Minimum dependency on wavelength, so the do and OPL is minimized for 18.5 GHz and 25.5 GHz. [minimize aberration]

At the receiver, after propagating for distance of 5.4 km for the ground experiment, the wavefront and amplitude distribution of the beam is plane with respect to the aperture of the RX system.

$1/R=1/R'-1/f$ Where R is the radius of curvature of the incoming beam and is infinite; therefore $f=R'$.

Therefore the expected amplitude beam profile at the RX Feed would be an Airy disk shape. The resulting spherical wavefronts converge to a spot in the RX feedhorn. However, since the receiver Feedhorn is characterized by a Gaussian beam parameters with w_0 as the beam waist located 2.3 cm behind the feedhorn aperture as shown in the previous section. Therefore in order to couple the expected Airy disk response to the Gaussian beam profile of the feedhorn as much as possible it will ensure the maximum power coupling to the Feedhorn.

If we define a circle which contains ~ 86% of the energy with diameter $d_0 = 2w_0$, since the input beam completely fills the lens of diameter $D=20$ cm.

$$d_0 = 2w_0 \sim 2f\lambda/D \tag{46}$$

since we want to fit to the w_0 of the feedhorn, then f can be estimated: $f \sim w_0 D/\lambda = 21.5$ cm very close to the value chosen in the TX case.

In regards to the choice of curved surfaces the following argument can be made: The advantages are two folds:

If the flat surface is oriented toward the horn, it creates a resonant cavity with the flat mounting plate on which the horn is mounted which will create unwanted standing waves and interferences due to multipath. If the flat lens surface is oriented toward the other ATOMMS instrument, there will be multipath between the two ATOMMS instruments as well. The amplitude of the electric field the of the first multipath mode is estimated to be a factor of $R^2/3$ lower than the direct signal where R is the Fresnel reflection coefficient which is ~ 0.2 for HDPE, therefore the first multipath signal would be lower than the direct signal by $0.04/3 = 1.3\%$, which is too large with respect to the tight specification of the maximum amplitude variations of $\sim 0.1\%$. Therefore a curved surface dramatically reduces this effect.

V.6.3 Lens design

In the previous sections we laid out some of the design criteria needed to design and construct the lens which was mainly focused on achieving best power coupling and mode matching between the quaioptics elements. In this section we report the some of the results of the lens design. The criteria for optimizing the surfaces were (minimize spot size, minimize chromatic aberration, and thickness). The resulting surfaces were both aspheric in order to minimize spherical aberration. The radii and conic factors are listed in Table V.4. Figures V.23,through V.26 show the lens shape, the Airy disk spot size for different wavelengths, the spot size with respect to the field change and the maximum OPD respectively. The rest of the data are shown in APPENIX C.

Parameters		units	Description
f	21	cm	Focal length
R1	49.246	cm	R of curv surface 1
R2	-14.714	cm	R of curv surface 2
k1	-13.58		Conic factor surf1
k2	-2.31		Conic factor surf2
do[zemax]	0.16	cm	Spot radius
tc	51.75	cm	thickness

Table V.4. 22 GHz HDPE zemax lens surfaces parameters

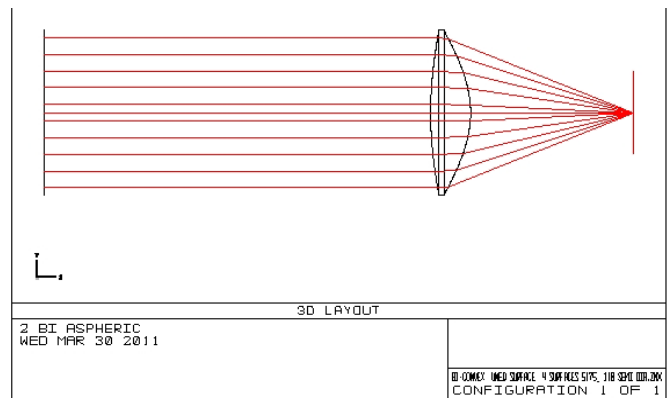


Figure V.23 Zemax Lens configuration

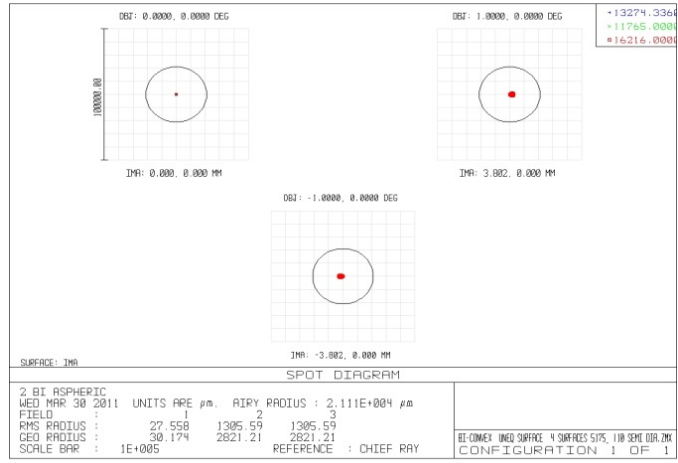


Figure V.24 Airy disk spot size

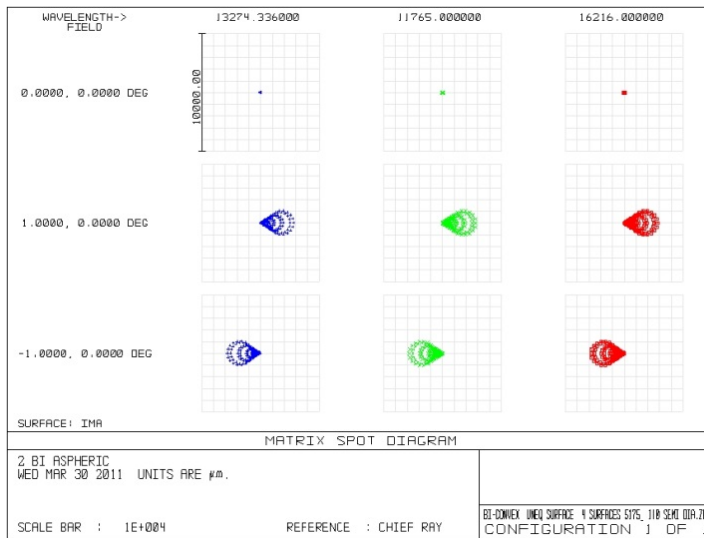


Figure V.25 Spot diagram for 0, +1,-1 deg fields

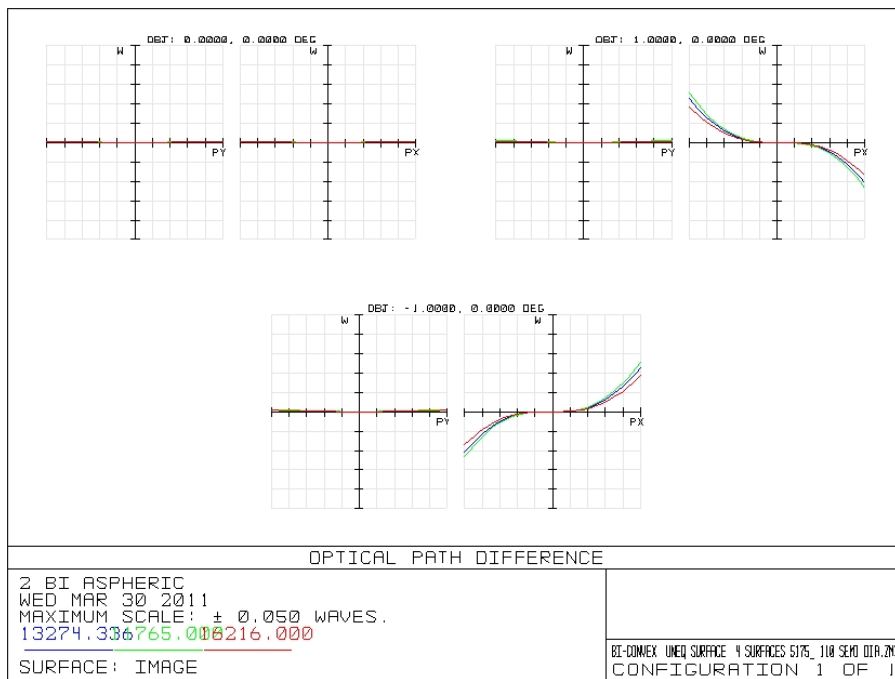


Figure V.26 OPD for 0, +1 deg and -1 deg fields

Zemax results are very satisfactory; spot size for the highest, lowest and center wavelength in the band 1.62, 1.327 and 1.137 cm. The maximum OPD measured at angles of +/-1 deg $0.05\lambda \sim 0.66$

mm. The Gaussian beam spot diagram is shown in Figure V.27 showing Gaussian waist of 1.64 cm, it might seem higher than what we have started the design with on the transmitter side, however this value doesn't take into account the Feed horn phase center which is not modeled in Zemax. If we propagate the Gaussian beam further beyond the geometric focal point defined by Zemax a distance equal to the Δpc predicted in section I of the design by a distance of 2.3 cm we get to $w(z=0) = w_0 = 1.43$ cm for $f = 22.6$ GHz.

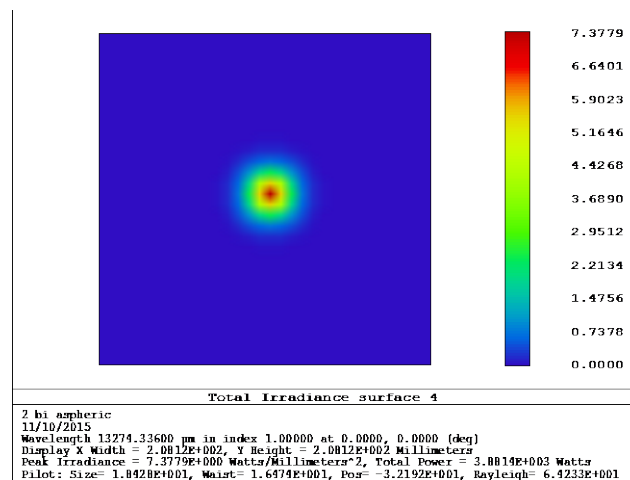


Figure V.25 The Gaussian beam spot produced by Zemax with $w_0 = 1.64$ cm

As mentioned earlier a similar procedure is recommended to be carried out when designing the 200GHz lens.

Up to this point we have successfully investigated and analyzed the diffraction problem caused by the 200GHz feedhorn to the 22 GHz beam. The simulation carried out both with FRED and with the Matlab both compare closely to the measurement made between the two instruments. After that we presented few design solutions with criteria derived from the ATOMMS performance requirements. The two lens design approach seemed to provide the lowest risk and less complicated to implement compared to the other concepts. A more recommended developmental

work which was not possible to fit it in the scope of this work is to test the design lens and verified all the predicted Gaussian beam parameters in this chapter to make a new assessment for performance of the ATOMMS instrument.

CHAPTER VI: CONCLUSION

In this work the design and characterization of two optical systems for remote sensing were investigated. The first was the optical fiber phase stabilization system used as part of the photonicallly generated microwave local oscillator (LO) signal for the ALMA interferometer. As part of this effort, the inherited design was characterized and its major short falls identified and mitigated by using an alternative novel approach. In Chapter I the scientific motivation behind the ALMA instrument was presented. This powerful instrument will observe emission from atoms and molecules, almost to the beginning of time itself. With this amazing remote sensing capability, it can help improve our understanding of things like how stars are formed, the nature of distant solar systems, and, perhaps, the likelihood of finding life elsewhere. Such capability requires a spectral band range from 30 GHz to >1 THz. The ALMA array is reconfigurable, with baseline lengths from a 50m to 20 km, providing an angular resolution of better than 1 arc second. To achieve the very high coherence requirement across the array, each ALMA antenna (64 in all) must have an ultra-stable local oscillator in its receiver. This requirement is met by using a photonicallly produced local oscillator reference generated by beating very narrow linewidth fiber lasers phase locked to a Rubidium gas cell (master laser) with a slave laser phase locked to the master with a frequency difference equal to the LO frequency. A detailed description of this process is provided in Chapter I.

Chapter II covered the existing (at the time) proof-of-concept design that we used an Optical Phase Stabilization in Fiber (OPCiF) approach. It started with the concept of using a Michaelson interferometer, where the very narrow laser signal (Master laser) is generated in the Near_End of the array and transmitted in the forward direction towards the Far_End of the array. A

portion of it is routed back using an optical circulator to the Near_End and mixed with a copy of the Master laser. The resulting signal carries the accumulated residual phase shift in the fiber length which is then conditioned and used to drive a fiber stretcher. The stretcher actively nulls the phase in the Far_End. The test results obtained for this system (see Section II.3.4) were far from what is needed to meet the ALMA phase stability specs. For 180 meters of fiber at an LO frequency of 26 GHz, it was only possible to achieve a phase drift of ~ 70 fs. Aside from the progress made to improve the phase stabilization of the fixed fiber, it was necessary to extend the performance of the OPCiF system for use with a moving fiber. Those measurements were made and results addressed in detail in the remaining part of Chapter II. The SOPD was measured for a moving fiber structure, both in the lab and at one of the prototype antennas site. Measurements of the SOPD for the buried fiber were also performed. The conclusion of those tests showed that the optical isolator exhibited a larger SOPD than anticipated. At a wavelength difference 0.7 nm, the total calculated optical length change is $\sim \Delta L = 1.7\text{mm}$, or about 5.6ps which is too large for ALMA's LO's.

To mitigate the limitation set by the optical isolator, a new novel technique is introduced and developed. Chapter III details the new approach, which replaces the optical circulators with beam splitters, an AOM cell, and a Faraday mirror. The outgoing and returning light are now diplexed by using the polarization beam splitter at the near end of the fiber. This results in a system that has less SOPD and thus less possibility of phase change due to fiber motion, while being less sensitive to polarization misalignment. Within this scheme the polarization was still free to vary along the fiber, but the reflected light is orthogonal to the transmitted light at every point in the fiber. The results were highly noticeable, yet still not enough to achieve the phase drift requirement.

The new limiting factor was found to be phase drifts resulting from larger SOPC and SOPD which were dependent on the type of fiber motion. It was found that bending at a constant radius produced the least SOPC and SOPD, in comparison to twisting or bending with a variable radius. The remainder of Chapter III covered the full implementation of using two newly designed fiber wraps that bend the fiber at a constant radius with a fiber length of 14 km. The OPSiF system was able to zero out most of the accumulated phase drift (~ 950 deg over 1.1 hr was reduced to ~ 2 deg over the same period) induced in the 81 GHz photonic LO signal due to the temperature and low frequency acoustical and vibrational noise from the surrounding environment. With the simulated antenna motion added to the setup, the calculated ASD was ~ 1.7 deg, yet it was still not fully immune to the sudden jumps in the phase induced due to the mechanical motion of the fiber wrap. The setup has a precision of ~ 0.4 deg over the 300 sec time period. This part of the work concluded that using this configuration of optical fiber based Michaelson optical interferometer can compensate for the temperature and ambient acoustic-related phase variations down to the femtosecond level. The limiting factors due to noise induced in the SOPC and/or SOPD long fiber, in the fiber wrap under motion, and in the fiber stretchers, needed to be characterized further.

The application of OPSiF in transferring accurate timing is not limited to the high coherence requirement of the ALMA instrument, this work can be expanded to use in many applications. For example, to precisely synchronize frequency and time between the ground and orbiting satellites, or compare remotely located atomic clocks, or to distribute highly coherent stable signals for different scientific applications, or to probe chemical dynamics using an X-ray pump, and many others.

The second part of the dissertation is an optics design and implementation for Earth and Space Atmosphere Remote Sensing using ATOMMS (Active Temperature, Ozone and Moisture

Microwave Spectrometer). ATOMMS uses a complimentary set of microwave transmitters and receivers in the ~22 GHz and ~183 GHz atmospheric water bands installed on converging aircraft to measure the absorption of water and ozone as a function of altitude. The system requires a front-end optics design to direct the transmitted beams from the nose cone of one aircraft to another. Chapter IV covers the detail design of the lens system, including the selection of the material used for the lenses and the testing and analysis of the index of refraction. Later in Chapter V the initial design using coaxial lenses was reevaluated using Matlab and FRED simulation software. The modeling of the diffraction was limited, since we simplified the 3 D diffraction problem to 1 and 2 D. Different design concepts were presented and evaluated against the performance of the ATOMMS instrument and an optimum design selected. The modeling of the lens produced excellent results, yet considerable work is still needed to verify the performance of the lens in the real system, which should be carried out as part of the future instrument development. As a future work, it would be very useful to measure the phase center of the two beams, so that final optimization of the beam coupling is achieved. Once fully built and tested, the ATOMMS instrument promises to revolutionize the way atmospheric limb sounding is conducted, providing increased accuracy, resolution, and coverage of planetary atmospheres.

- **B. Design Constraints**

- 1. Minimize Dichroic size=> closest possible to the 200 FH
- Assume a 1st minimum dimension of Lmesh=sqrt(3^2+3^2)=4.24 cm
- 2.minimize beam distortion (NOT MET)
- 3. 22 GHz system in focus

- **C. Variable Parameters with their constraints:**

- 1. dmesh= distance from the center of the mesh to the 200FH aperture= 1cm
- 2. from 1 the 22 GHz beam waist is at x= 1.0 cm from the point c.
- 3. 22 GHz feedhorn location [distance from center line of the 22 GH FH aperture to 200 GHz FH center of aperture: d_200_22 FHs
- * d_200_22 FHs_min=4.5 cm.

- d_200_22 FHs need to me at minimum so that as the 22 Ghz beam gets reflected doesn't grow after focus large, which will make the dichroic mirror small enough, for now we choose 4.5 cm. But with x22=4.5 cm we need to move z22 to z22= - 3.5 cm.

- **D. From the above we can estimate both the beam distortion U, the focal length of the surface fe, and the Diameter of the ellipsoid D.**

- * here we made R1=R2=R but R is NOT = to the radius of curvature Rz at the surface of the reflecting mirror.
- Fe= R/2=2.25
- Theta_p= PI-acos(R1^2-R2^2+Ao^2/2R1Ao) ; Ao=sqrt(R1^2+R2^2))
- Thetap= PI-Pi/4= 3PI/4
- With Thetai = PI/4
- PSI= 3PI/4-Pi/4= PI/2
- wm=1.9575,
- U=wmtan(thetai)/2sqrt(2)fe
- Theta i= 45 deg U = 0.1532.
- Kf= 1-U^2= 0.9765
- D should be > 4 wm= ~ 4 * wm= 9cm which is very large.

- **E. NOTES:**

- 1. To minimized D we have to have a smaller wm which means either get even closer to the Fh22 or redesign the FH such that to get a starting wo to be less than 1.44 cm.
- 2. The further the curved lens is away from the 22 GH FH, the larger wm becomes at the surface of the mirror, which means the larger the Diameter of the mirror would have to be.
- 3. still Need to calculate the cross polarization the effect of surface accuracy Metal reflection
- 4 the orange dontted line shows how large the D of the curved mirror needs to be _ 8- 9 cm

REFERENCES

- [1] Wootten & Gallimore (2000, ASP Conf. Ser. Vol. 240, pg. 54). Bottom images from K. Lanzetta, K. Moore, A. Fernandez-Soto, and A. Yahil (SUNY). © 1997 Kenneth M. Lanzetta
- [2] A. Dutrey¹ - S. Guilloteau¹ - V. Piétu² - E. Chapillon^{1,2} - F. Gueth² - T. Henning³ - R. Launhardt³ - Y. Pavlyuchenkov³ - K. Schreyer⁴ - D. Semenov³ “Cavities in inner disks: the GM Aurigae case” A&A 490, L15-L18 (2008)
- [3] Empirical Constraints on Turbulence in Protoplanetary Accretion Disks A. Meredith Hughes¹, David J. Wilner¹, Sean M. Andrews¹, Chunhua Qi¹, Michiel R. Hogerheijde²
- [4] ALMA observations of α Centauri - First detection of main-sequence stars at 3 mm wavelength L4 R. Liseau, W. Vlemmings, A. Bayo, E. Bertone, J. H. Black, C. del Burgo, M. Chavez, W. Danchi, V. De la Luz, C. Eiroa [et al. \(12 more\)](#) Published online: 19 December 2014.
- [5] “Site Test Interferometer,” Radford, S. J. E., Reiland, G., Shillue, B., 1996, PASP 108,441
- [6] “Interferometry and Synthesis in Radio Astronomy”, A.R. Thompson, I. M. Moran, and G. W. Swenson, Jr., 2nd Ed, Wiley, - New York, 2001, p. 233
- [7] H. Ito, T. Ito, Y. Muramoto, T. Furuta, T. Ishibashi “Rectangular waveguide output unitraveling-carrier photodiode module for high-power photonic millimeter-wave generation in the F-band,” IEEE JLT Vol. 21, Dec 12 2003, pp. 3456-3462
- [8] P. Huggard, B.N. Ellison, P. Shen, N. Gomes, P.A. Davies, “Efficient generation of guided millimeterwave power by photomixing,” IEEE Photonics.

[9] P. Shen, P.A. Davies, W.P. Shillue, L.R D'Addario, J.M. Payne, "Millimetre-wave generation using an optical comb generator with optical phase-locked loops, Proc MWP 2002, pp. 101-104

[10] S. Fukushima, C.F.C. Silva, Y. Muramoto, and A. J. Seeds, "Optoelectronic Millimeter-Wave Synthesis Using an Optical Frequency Comb Generator, Optically Injection-Locked Lasers, and a Uni- Traveling-Carrier Photodiode," IEEE J Lightwave Tech., Vol. 21, No. 12, Dec. 2003, pp. 3043-3051

[11] J. Ye, J. L. Hall, "Optical Phase Locking in the Microradian Domain: Potential Application to NASA Spaceborne Optical Measurements," Optics Letters, Vol. 24, No. 24, Dec 15, 1999, pp. 1838- 1840

[12] Cicerone, Ralph J., et al., Climate Change Science: An Analysis of Some Key Questions National Research Council, 2001, National Academy vPress, pp 23-24

[13]http://www.atmo.arizona.edu/personalpages/kursinsk/papers/ATOMMSv_051605_corrected.pdf.

[14] E. R. Kursinski, E. R., et al., "The Active temperature, ozone and moisture microwave spectrometer (ATOMMS)", in vECMWF/EUMETSAT GRAS SAF Workshop Proceedings, The applications of GPS Radio Occultation Measurements. S. Healy Ed. V 2008

[15] John D. Anderson Jr " Ludwig Prandtl's Boundry layer"prandtl_vol58no12p42_48.pdf APS journal http://www.aps.org/units/dfd/resources/upload/prandtl_vol58no12p42_48.pdf

[16] Ware, R., and Coauthors, 1996: GPS sounding of the atmosphere from low Earth orbit: Preliminary results. Bull. Amer. Meteor. Soc, 77, 19-40.

[17] Wickert, Jet al. (2001), Atmosphere sounding by GPS radio occultation: First results from CHAMP, *Geophysical Research Letters*, 28(17), 3263-3266.

[18] Hajj, and Coauthors, 2004: CHAMP and SAC-C atmospheric occultation results and intercomparisuns. *J. Geophys. Res.*, 109, D06109, doi:10.1029/2003JD003909.

[19] Anthes, R. A., et al. (2008), The COSMIC/FORMOSAT-3 mission: Early results, *Bulleting of the American Meteorological Society*, 89(3), 313-333

[20] Schneider, T., O’Gorman, P. A., and Levine, X. J.: Water vapor and the dynamics of climate changes, *Rev. Geophys.*, 48, RG3001, doi:10.1029/2009RG000302, 2010

[21] Sherwood, S. C., Roca, R., Weckwerth, T. M., and Andronova, N. G.: Tropospheric water vapor, convection, and climate, *Rev. Geophys.*, 48, RG2001, doi:10.1029/2009RG000301, 2010.

[22] Westwater, E. R.: Atmospheric Remote Sensing by Microwave Radiometry, Chap. 4. Ground-based microwave remote sensing of meteorological variables, John Wiley & Sons, edited by :Janssen, M. A., 1993.

[23] Oikonomou, E. K., and a. O’Neill (2006), Evaluation of ozone and water vapor fields from the ECMWF reanalysis ERA-40 during 1991-1999 in comparison with UARS satellite and MOZAIC aircraft observations, *J. Geophys. Res.*, 111, D14109

[24] Kursinski, E. R., D. Ward, A. Otarola, R. Frehlich, C. Groppi, S. Albanna, M. Schein, W. Bertiger and M.Ross (2009), The Active Temperature Ozone andMoisture Microwave Spectrometer (ATOMMS), Bookon Proceedings of 3rd International Workshop on Occultations for Probing Atmosphere and Climate(OPAC-3), Sept 17–21, 2007, Graz, Austria,Available: December 4, 2009.]

- [25] Kursinski, E. R., S. B. Healy and L. J. Romans, 2000b, Initial Results of Combining GPS Occultations with ECMWF Global Analyses within a 1Dvar Framework, *Earth, Planets and Space*, **52**, 885-892.
- [26] Fjeldbo, G., A. J. Kliore, and V. R. Eshleman, 1971: The neutral atmosphere of Venus as studied with the *Mariner V* radio occultation experiments. *Astron. J.*, **76**, 123–140. Gorbunov, M. E., 2001: Radio holographic methods for processing radio occultations data in multipath regions. Danish Meteorological Institute Scientific Rep. 01-01, Copenhagen, Denmark,
- [27] Tricomi, F. G., 1985: Integral Equations. Dover, 233 pp.
- [28] Kursinski, E. R., 1997: The GPS radio occultation concept: Theoretical performance and initial results. Ph.D. thesis, California Institute of Technology, Pasadena, CA, 374 pp.
- [29] J. Moran, “The Submillimeter Array,” Proc SPIE Vol 3357, Symposium on Advanced Technology MMW, Radio, and Terahertz Telescopes, March, 1998, pp. 208-219
- [30] T. Kakuta, S. Yanaka, “LCP Coated Optical Fiber with Zero Thermal Coefficient of Transmission of Delay Time,” Proc. 36 The Int. Wire and Cable Symp., 1987, pp. 234-240
- [31] L. D’Addario, M. Stennes, “Transmission of Timing References to Sub-Picosecond Precision over Optical Fiber,” Proc. SPIE Vol. 3357, Symposium on Advanced Technology MMW, Radio, and Terahertz Telescopes, March, 1998, pp. 691-701
- [32] M. Calhoun, R. Sydnor, W. Diener, “A Stabilized 100- Megahertz and 1-Gigahertz Reference Frequency Distribution for Cassini Radio Science,” the Interplanetary Network Progress Report 42-148, Feb 15, 2002, http://ipnpr.jpl.nasa.gov/tmo/progress_report/42-148/148L.pdf

- [33] K. Sato et al, "Development of an Ultra-Stable fiber Optic Frequency Distribution System Using an Optical Delay Control Module," IEEE Transactions on Instrumentation and Measurement, Vol. 49, No. 1, Feb. 2000, pp. 19-24
- [34] T.P. Celano et al, "Sub-Picosecond Active Timing Control Over Fiber Optic Cable," http://www.timing.com/docs/2002_paper_final4.pdf, (as of 2002-11-14)
- [35] S. Durand, T. Cotter, "Operational Performance of the EVLA LO Round-Trip Phase Systems, EVLA memo#144 July 2002,
- [36] S. Durand, T. Cotter, "Operational Performance of the EVLA LO Round-Trip Phase System, EVLA Memo #144 July2002
<http://www.aoc.nrao.edu/evlainternal/geninfo/memoseries/evlamemo44.pdf>
- [37] W.S. Jia et al, "Thermal Characteristics of the Propagation Delay for Bare and Cabled Single-Mode OVD Fibers,"
- [38] A.H. Hartog et al, "Variation of Pulse Delay with Stress and Temperature in Jacketed and Unjacketed Optical Fibres," Optical and Quantum II, Chapman and Hall Ltd,1979, pp. 265-273
- [39] L.G. Cohen, J.W. Fleming, "Effect of Temperature on Transmission in Lightguides," Bell Sys Tech Journal, Vo. 58, No. 4, April, 1979, pp. 945-951
- [40] Roger Norrod, "Measurement of Optical Fiber Temperature Coefficient of Delay," National Radio Astronomy Observatory, Electronics Division Technical Note #168, 1993
- [41] L. Snyder, S. Radford, M. Holdaway, ALMA memo #314, "Underground Temperature Fluctuations and Water Drainage at Chajnantor," 2000 June 30

- [42] Larry D'Addario, "Fiber Dispersion Calculations and Their Implications for Length Correction," internal report dated April 2002, available via ALMA EDM
- [43] M. Holdaway, private communication, 2002 -10-11
- [44] E. Silverberg, SMA Technical Memo #122, "Temperature Measurements in the Mauna Kea fiber Optic Conduits," 1998 May.
- [45] K. Nakagawa and A. Onae, "Development of an acetylene optical frequency standard at 1.5 μm and its application." *Proc. SPIE*, vol 4269 p 41 (2001).
- [46] M. Brooks, "ALMA monitor and control bus AMBSI-1 standard interface design description." ALMA Computing Memo #13, 2002-Mar-05.
- [47] ALMA doc# BEND-56.03.00.00-001-A-TDR "ALMA Photonic LO Reference: Buried Fiber Polarization Measurements at the VLA" Sarmad Albanna, Bill Shillue
- [48] ALMA doc# BEND-56.03.00.00-001-A-TDR "ALMA Photonic LO Reference: Buried Fiber Polarization Measurements at the VLA" Sarmad Albanna, Bill Shillue
- [49] L. Ma, P. Jungner, J. Ye, J.L. Hall, , "Delivering the same Optical Frequency at two places: accurate cancellation of phase noise introduced by an optical fiber or other time- varying path," *Optics Letters*, Vol. 19, No. 21, Nov. 1, 1994, pp. 1777-1779
- [50] Wootten, A., "Atacama Large Millimeter Array" *Proc SPIE* vol4837, 110-1 18 (2003).
- [51] www.eso.org/projects/alma
- [52] Payne, J., Shillue, B., Vaccari, A., "Photonic Techniques for Use on the Atacama Large Millimeter Array," *Proc. MWP*, 105-108 (1999).
- [53] Payme, J., Shillue, B. "Photonic techniques for local oscillator generation and distribution in millimeter wave radio astronomy," *Proc. MWP*, 9-12 (2002).

[54] Ito, H., Ito, T., Muramoto, Y., Furuta, T., Ishibashi, T., “Rectangular waveguide output untraveling-camer Photodiode module for high-power photonic millimeter-wave generation in the F-band,” IEEE JLT Vol. 21, 3456-3462 (2003).

[55] Cliche, J.-F., Shillue, B., Latrasse, C., Têtu, M., and D’Addario, L. R., “A high coherence, high stability laser for the photonic local oscillator distribution of the atacama large millimeter array,” in Proc. SPIE—Ground-Based Telescopes, vol. 5489, 1115–26 (2004).

[56] Shen, P., Gomes, N. J., Davies, P. A., and Shillue, W. P., “Polarization Mode Noise in Ultra-low Drift Phase Reference Distribution System over a Fiber Network. Microwave Photonics, 2005. MWP 2005, International Topical Meeting, 12-14,297-300, (2005).

[57] Huggard, P., Ellison, B.N., Shen, P., Gomes, N., Davies, P. A., “Efficient generation of guided millimeter wave power by photomixing,” IEEE Photonics Tech Letters, Vol. 14, 197 -199 (2002).

[58] Martinelli, M., “A Universal Compensator for Polarization Changes Induced By Birefringence on a Retracing Beam,” Optics Communication, Vol. 72, No. 6, **15**,341-344 (1989).

[59]. Dangui V., Kyun Kim, H., Digonnet, M. J. F., and Kino, G. S., “Phase sensitivity to temperature of the fundamental mode in air-guiding photonic bandgap fibers” OPTICS EXPRESS 667, / Vol. 13, No. 18, 6669-6684 (2005).

[60] P. F. Goldsmith, QuasiOptics Systems, NewYork, IEEE Press, John Wiley & Sons, 1998 pp157-176.

[61] Constantine A. Balanis, Antenna Theory: Analysis and Design, New York, NY, John Wiley & Sons,1997, 2nd Edition, p60.

[62] P. F. Goldsmith, QuasiOptics Systems, New York, NY, IEEE Press, John Wiley & Sons, 1998 pp129-139.

[63] A. Sengupta, A. Bandyopadhyay, B.F. Bowden, J.A. Harrington and J.F. Federici, "Characterization of Olefin copolymers using terahertz spectroscopy" The Institution of Engineering and Technology 2006, 13October2006. Electronics Letters online no: 20063148 1

[64] G. A. Ediss & T. Globus, "60 to 450 GHz Transmission and Reflection Measurements of Grooved and Un-grooved HDPE Plates", ALMA Memo No. 347, National Radio Astronomy Observatory Charlottesville, VA 22903, Dept of EE, University of Virginia.

[65] D. Raguin, G. Morris, "Analysis of anti-reflection-structured surfaces with continuous one-dimensional surface profiles", Applied Optics 32 (14) (1993) 2581–2598.

[66] D. Raguin, G. Morris, Anti-reflection structured surfaces for the infrared spectral region, Applied Optics 32 (7) (1993)

[67] Nancy Jane Bailey and A. R. Kerr, Electronics Division Technical Note No. 155 PROGRAM "SCATTER" FOR THE ANALYSIS OF DIELECTRIC MATCHING LAYERS, 12 September 1989. <http://www.gb.nrao.edu/electronics/edtn/edtn155.pdf>

[68] Born and Wolf, Principles of Optics, London, UK, 4th edition 1970, PERGAMON PRESS S.A.R.L, P61

[69] J. Lamb, "Cross-Polarization and Astigmatism in Matching grooves." International Journal of Infrared and Millimeter Waves Vol.17, No. 12, 1996. Otarola, A.C., The effects of turbulence in an absorbing atmosphere on the propagation of microwave signals used in an active sounding system. Ph.D. dissertation, The University of Arizona, United States -- Arizona. ProQuest Digital Dissertations @ University of Arizona database. (Publication No. AAT 3336701) 2008.

[70] A. Sengupta, A. Bandyopadhyay, B.F. Bowden, J.A. Harrington and J.F. Federici, "Characterization of Olefin copolymers using terahertz spectroscopy" *The Institution of Engineering and Technology* 2006, 13October2006. Electronics Letters online no: 20063148 1

[71] Herloski, Robert et al "Gaussian Beam Ray-Equivalent Modeling and Optical Design", *Applied Optics*, Vol. 22, No. 8, p. 1168-1174, April 1983 (Erratum, *Applied Optics*, Vol 22, No. 20, p 3151)

[72] Arnaud, Jacques, "Representation of Gaussian Beams by Complex Rays", *Applied Optics*, Vol. 24, No. 4, p. 538-543, Feb 1985

[73] Arnaud, Jacques and Kogelnik, H., "Gaussian Light Beams with General Astigmatism", *Applied Optics*, Vol. 8, No. 8, p. 1687-1693, Aug 1969

[74] Arnaud, Jacques, "Nonorthogonal optical Waveguides and Resonators," *Bell System Technical Journal*, November 1970, p 2311-2348

[75] Bastiaans, M.J., "The Expansion of an Optical Signal into a Discrete Set of Gaussian Beams", *Optik*, Vol. 57, p 95-101, 1980

[76] Bastiaans, M.J., "Gabor's Expansion of a Signal into Gaussian Elemental Signals" *Proc. IEEE*, Vol. 68, p 538-539

[77] Greynolds, Alan W, "Propagation of Generally Astigmatic Gaussian Beams Along Skew Ray Paths", *Proceedings of SPIE, Current Developments in Optical Engineering and Diffractive Phenomena* 560 (1985), p 33-50

[78] Greynolds, Alan W., “ Vector Formulation of the Ray-Equivalent Method for General Gaussian Beam Propagation”, Proceedings of SPIE, Current Developments in Optical Engineering and Diffractive Phenomena 679 (1986), p 129-133

[79] Ru-Shan Wu and Ling Chen “Wave Propagation and Imaging Using Gabor-Daubechies Beamlets”, the Proceedings of the 5th International Conference on Theoretical and Computational Acoustics (May 21-25, 2001, Beijing, China)

[80] P. F. Goldsmith, *QuasiOptics Systems*, NewYork, IEEE Press, John Wiley & Sons, 1998 pp [168-172].